Current Reports on Science and Technology

(A Peer Reviewed Research Journal)

Faculty of Sciences
Khalsa College Amritsar

Current Reports on Science and Technology

(A Peer Reviewed Research Journal)
Bi –Annual
(July-December 2015)

ISSN : 2455-023X

Subscription
Life Member : Rs. 1500/-
Five Years : Rs. 750/-
Per Copy : Rs. 125/-

For Subscription write to :
Librarian, Khalsa College Amritsar
Email : chiefeditorjpas@gmail.com, Ph: +91 183 2258097, Fax : +91 183 2255619

Current Reports on Science and Technology Published by Faculty of Sciences, Khalsa College Amritsar and printed at Printwell 146, Focal Point, Amritsar

Current Reports on Science and Technology

(A Peer Reviewed Research Journal)

Bi –Annual

Volume – 01 Issue – 02 July-December 2015

Contents

Editorial v

1. International Year of Light *Kulwant Singh Thind* 1-11

2. Effect of Replacing Oxide with Fluoride Anion on the Physical and Spectroscopic Properties of Nd^{3+} Doped Borate Glasses
Shaweta Mohan 12-20

3. Germination And Early Biochemical Responses In Brassica campestris L. To Pre-Soaking Chilling Treatment
Kirandeep Kaur Hundal and Navkiran Randhawa 21-28

4. Photon Interaction Parameters for $ZnO-Al_2O_3-Fe_2O_3-P_2O_5$ Glass Systems
Preet Kaur, Tejbir Singh and Devinder Singh 29-37

5. Correlation Among The Structural, Morphological And Gas Sensing Parameters Of USP Deposited Al-CuO Films
Iqbal Singh, Taminder Singh and Gursharan Kaur 38-45

6. Structural, Magnetic and Optical Properties of Cobalt Doped Zinc Oxide
Anumeet Kaur, Veerpal Kaur, Vandana, Anupinder Singh, Mandeep Singh and Lakhwant Singh 46-51

7. A study of indoor radon, thoron and their progeny concentration in Rohtak district of Southeast Haryana, India
Joga Singh, Amanjeet, Ajay Kumar, Jaspal Singh and Gurinderpal Singh 52-61

8. Cytotoxicity of Graphene
Zorawar Singh and Balinder Singh 62-69

9. Indoor Radon and Thoron Estimates in District Hamirpur, Himachal Pradesh, India
Parminder Singh and B.S. Bajwa 70-77

10. Dynamics of Odd Mass Lighter Compound System at Different Excitation Energies
BirBikram Singh and Manpreet Kaur 78-84

11. Effect of orientations in the decay ofvery light mass compound nucleus ^{28}Al* formed in ^{18}O+^{10}B and ^{19}F+^{9}Be reactions
BirBikram Singh, Mandeep Kaur, and Manoj K. Sharma 85-92

12. Synthesis and Biological Activities of 1,3,5-Trisubstituted Pyrazolines
M. S. Batra, Amandeep Singh, Sujita Thakur and Hardeep Kaur 93-111

13. Nonlinear Electron Acoustic Waves in Multispecies Plasma With Non-Maxwellian Electrons
Harvinder Kaur and Tarsem Singh 112-118

14. Effect of Heavy Ion Irradiation on Conductivity of Polyethylene Naphthalate (PEN)
Kusum Devgan and Navjeet Kaur 119-123

15. Ion Track Membrane As Template For Copper Nanowires
S. Amrita Kaur and G.S. Randhawa 124-130

Editorial

This issue of Current Reports on Science and Technology, a peer reviewed research journal, has been dedicated to the international Year of Light. The 68th session of the United Nations General assembly on 20 December 2013 adopted the resolution A/RES/68/221 proclaiming the 2015 as the International Year of Light. The key theme of the year aims to raise awareness of the importance of light-based technologies in providing solutions to worldwide challenges in areas such as energy, education, communications and health. The light-based technologies can provide solutions to challenges in the developing world in the form of ending light poverty. This issue of the Journal is also a tribute to Dr. N.s. Kapani famously known as *"The Sardar who bent the light"*. The discovery of optical fibre paved the way for communication revolution.

A lot of efforts have been put in the careful presentation of this issue of Journal of Pure and Applied Sciences. It will be the endeavour of the publishers to maintain the international standards of peer review process in publishing the research articles. The views of the referees will have the last word in selecting the research papers.

This issue is open to the constructive criticism and the suggestions for improvements in next issues will always be welcome.

Dr. Taminder Singh
Chief Editor

ਸੋ ਪੜਿਆ ਸੋ ਪੰਡਿਤੁ ਬੀਨਾ ਗੁਰ ਸਬਦਿ ਕਰੇ ਵੀਚਾਰੁ ॥
ਅੰਦਰੁ ਖੋਜੈ ਤਤੁ ਲਹੈ ਪਾਏ ਮੋਖ ਦੁਆਰੁ ॥

(ਅੰਗ ੬੫੦)

He alone is educated, and he alone is a wise Pandit,
who contemplates the Word of the Guru's Shabad.
He searches within himself, and finds the true essence; he finds the Door of Salvation.

(SGGS Ang. 650)

Curr. Rep. Sci. & Tech. 1 (2) (2015) 1-11

International Year of Light

Kulwant Singh Thind
Former Head, Department of Physics
Guru Nanak Dev University, Amritsar (India)
kulwantsthind@yahoo.com

The year 2015 is a wonderful choice for celebrating the International Year of Light because it marks a number of anniversaries; 1000 years since the Islamic Golden Age dedicated to Ibn al-Haytham (1015), father of scientific methods; 400 years since the French engineer and garden architect Salomon de Caux devised a solar powered mechanism; 200 years since the French physicist Augustin Jean Fresnel (1815) established and developed the wavetheory of light (Fresnel's theory of diffraction); 150 years since the British physicist James Clerk Maxwell (1865) produced the unified theory of electromagnetism, including light,that paved the way for technologies from lasers to mobile phones; 100 years since the German-Swiss theoretical physicist Albert Einstein (1915) conceived the theory of General Relativity, stressing the central importance of light in both space and time; 80 years since the Russian physicist Pavel Cherenkov (1934) discovered the Cherenkov light caused by a charged particle moving faster than the speed of light in a medium; 50 years since the US astrophysicists Arno Penzias and Robert Wilson (1965) discovered the Cosmic Microwave Background Radiation, providing some of the strongest evidence for the "Big Bang" theory for the origin of the universe; and 50 years since the Chinese-born Hong Kong, British and US electrical

engineer and physicist Charles Kao (1965) pioneered the development of low-loss fibres for optical communication, thus enabling fast and massive internet transmissions.

Light is very important in all aspects of our lives. Through photosynthesis, light is arguably the basis of life. Illumination is the energy that let us develop visual tasks like reading, identifying colors, perceiving volumes, measuring physical dimensions. Sunlight can be converted into electricity to heat our homes and power our industries. We can add value to our homes, institutions, public spaces, commercial areas, cultural facilities, working spaces and practically all spaces by the use of light. Light is the means by which humanity sees itself. All people see the same sun rise and fall on horizon and all cultures throughout history express the same wonder at the natural beauty of light seen in effects such as the rainbow.

Through studies in fundamental science ranging from particle physics to cosmology, light provides a window on the universe. Light played an important role in electromagnetic research by the Dutch theoretical physicist Hendrik Anton Lorentz, who studied the propagation of light, and the Lorentz transformation. The latter was shown later by Einstein to emerge naturally from his special theory of relativity. Using telescopes for light in its many forms, from radio waves to gamma rays, scientists are getting a better understanding of processes at work in Universe.

Science and technology of light are essential for the future development of humankind and in search of solutions to solve global problems in sustainability and healthcare through international cooperation. Optics and photonics have completely transformed the way we live today, and light transmits signals across the globe at the fastest possible speeds, and new technology developments have revolutionised the way we display and receive information and communicate.

Light has been the use of poets and painters for centuries. Less known to the public is the fact that light is also an inspiration for countless scientists and physicists that include names such as Newton, Einstein, Huygens, Planck, Hertz, Maxwell and Townes.

Finally, light as a form of energy used in architecture requires electricity. Light defines the architectural space; it contributes to its perception and understanding while adding value to its function and

bringing an emotional component for its users. One of the pioneers of the use of light as part of the architectural concept was Richard Kelly. He established three basic visual effects in order to design the lighting of any space. This means that the use of light has an impact on environment and therefore it is also essential to plan and design lighting in the most energy efficient way in order to preserve our planet. The International Year of Light will bring together a wide range of different communities, from astronomy to medicine and photonics to arts and culture.

The Resolution:

The UNESCO (United Nations Educational, Scientific and Cultural Organization) Executive Board adopted a resolution welcoming and endorsing an International Year of Light in 2015 at its 190th session in Paris 318 October 2012. The resolution was placed before the Executive Board by Ghana, Mexico and the Russian Federation (Board Members) and New Zealand (UNESCO Member State). UNESCO delegates from Ghana and Mexico introduced the proposal to the Executive Board. The resolution was adopted by the Executive Board joined by co-signatories from a further Board Members: Angola, Bangladesh, Brazil, Burkina Faso, China, Congo, Cuba, Djibouti, Ecuador, Ethiopia, Gabon, Gambia, Kenya, Indonesia, Italy, Malawi, Nigeria, Peru, the Republic of Korea, Saudi Arabia, Spain, Thailand, Tunisia, the United Arab Emirates, the united States of America, Venezuela and Zimbabwe. Other Member States of UNESCO who declared support for the initiative were Hungary, Serbia and South Africa.

The UNESCO General Conference endorsed the UNESCO Executive Board resolution at its 37th session on November 19, 2013. In parallel, a resolution was submitted to the United Nations Second Committee on 6th November 2013 by the nation of Mexico with delegates from both Mexico and New Zealand speaking in support. The resolution was adopted with co-sponsorship from 35 counties: Argentina, Australia, Azerbaijan, Bosnia and Herzegovina, Chile, China, Colombia, Cuba, Dominican Republic, Ecuador, Franc, Ghana, Guinea, Haiti, Honduras, Israel, Italy, Japan, Mauritius, Mexico, Montenegro, Morocco, Nepal, New Zealand, Nicaragua, Palau, Republic of Korea, Russian Federation,

Somalia, Spain, Sri Lanka, Tunisia, Turkey, Ukraine and United States of America.

The 68th session of the United Nations General assembly on 20 December 2013 adopted the resolution A/RES/68/221 proclaiming the 2015 as the International Year of Light.

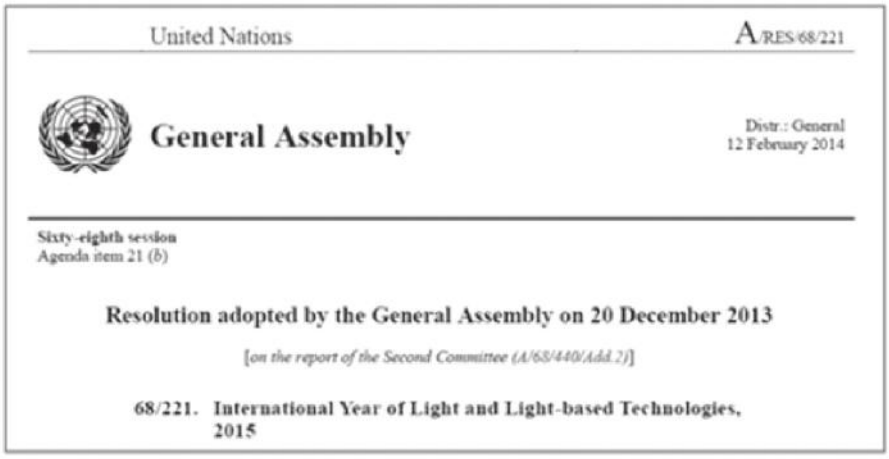

United Nations A/RES/68/221

General Assembly

Distr.: General
12 February 2014

Sixty-eighth session
Agenda item 21 (b)

Resolution adopted by the General Assembly on 20 December 2013

[*on the report of the Second Committee (A/68/440/Add.2)*]

68/221. International Year of Light and Light-based Technologies, 2015

The official Opening Ceremony took place on 19-20 January 2015 at the UNESCO Headquarters in the iconic "Fontenoy Building" near the Eiffel Tower Paris, France. This was the beginning of a yearlong series of activities all over the world. The two-day event gathered over 1,000 participants comprising together Nobel laureates, international dignitaries, leading scientists and representatives from governments, industry and academia. It introduced all key themes of the year, acting as inspiration for events worldwide during 2015 to raise awareness of the importance of light-based technologies in providing solutions to worldwide challenges in areas such as energy, education, communications and health.

One of the key themes on the second day of the event was the notion that light-based technologies can provide solutions to challenges in the developing world in the form of ending light poverty. The year will bring together many different stakeholders including scientific societies and unions, educational institutions, technology platforms, non-profit organizations and private sector partners, focusing specifically on how the science of light can improve the quality of life in the developing world and in emerging economies. An outcome of this realisation was a pledge to end

light poverty by the year 2030 by providing off the grid electricity by the means of utilising solar energy. An equivalent topic of importance was the realisation and mitigation of the imminent threat of climate. The opening ceremony was brought to an end by a discussion of global science policies with the emphasis of international collaborations.

Major Scientific Anniversaries:

The year 2015 will mark the following major scientific anniversaries, from the early works on optics by Ibn Al-Haytham in 1015 to Kao's achievements on the transmission of light in fibres for optical communications in 1965.

1000 Years of Arabic Optics:

It is 1000th anniversary of the Book of Optics written by Ibn al-Haytham in 1015. Ibn al-Haytham was born around 965 in Basra and died around 1039 in Cairo. He contributed greatly to the understanding of vision, optics and light. His work helped change science around the world and is known today as the 'Book of Optics'.

Ibn al-Haytham is known for being the first person to test hypotheses through experiments that could be repeated, as much as two centuries before scholars in the west began to do so. His scientific and mathematical reputation earned him the nickname 'Ptolemy the Second' and he often is regarded as the "father of modern optics".

400 Years of Solar Powered Mechanism:

It is 400 years since the French engineer and garden architect Salomon de Caux devised an optical-mechanical apparatus driven by solar energy. His device consisted of glass lenses and an airtight metal vessel containing water and air. When the air was heated by focusing the sunlight, a small water fountain was produced.

200 Years of Fresnel's Theory of Diffraction:

It is 200 years since Fresnel's transformational paper on the wave nature of light. During the late 17^{th} century, scientists were embroiled in a debate about the fundamental nature of lightwhether it was a particle or wave. Sir Isaac Newton was a strong advocate of the theory that light was

made of particles known as “corpuscles”. Newton attempted to disprove the theory that light was composed of waves, a concept which was first proposed by the French philosopher René Descartes in 1637. However, some important work carried out by Fresnel changed the way in which the scientific community thought about the nature of light.

150 Years of Maxwell's Electrodynamics:

It is 150 years since James Clerk Maxwell published his work on the unification of electricity and magnetism in Philosophical Transactions of the Royal Society. Maxwell's most significant scientific achievement was his electromagnetic theory of light propagation, which he first presented in 1864 with the publication of 'A Dynamical Theory of the Electromagnetic Field'. This paper hypothesised that an electric field, a magnetic field and light could all be explained by using a single theory.

An early inspiration for Maxwell's work took place in Copenhagen in 1820, when H. C. Oersted embarked on a series of experiments to illustrate the connection between magnetism and electricity. A decade later, Michael Faraday converted electric energy into magnetic energy using an insulated wire and a galvanometer. Maxwell understood the significance of Faraday's work and realised that the speed of an electromagnetic waves travelled at the speed of light. As a result, he was able to incorporate light, magnetism and electricity into a single theory. Maxwell further concluded that light propagated in electric and magnetic waves, which he believed would vibrate perpendicular to one another.

This theory of light propagation paved the way for a number of major technological innovations. The first and possibly most significant of these occurred in 1888, when Heinrich Hertz used Maxwell's theory to create instruments capable of sending and receiving radio pulses. This discovery, contributed to the creation of the television and the microwave. James Clerk Maxwell truly is the champion of modern day science.

100 years of Einstein's General Relativity General Relativity:

It is 100 years since Einstein's general theory of relativity emerged,

supporting standard cosmological models quite successfully. Before publishing his general relativity theory in 1916, Einstein decided to include an additional constant term to his field equations. One year later, in his 1917 paper Cosmological Considerations in the General Theory of Relativity, Einstein announced that his favoured cosmological model was one, which differed from his previous model. In this paper, Einstein's universe was mathematically described as spatially finite but temporally infinite.

Einstein's theory helped to speed up the discovery of black holes and the detection of intense radiation emitted from massive, dead stars in active galactic nuclei. General relativity also accurately predicts and explains gravitational bending, i.e. the ability of the path of light to be bent by a gravitational field. Experiments performed during solar eclipses have confirmed that light rays passing close to the sun are bent by the gravitational field of the sun. Currently astrophysicists are interested in formulating a theory of quantum cosmology, which attempts to reconcile post-Big Bang quantum conditions with Einstein's general relativistic principles

80 Years of Cherenkov light:

It is 80 years since the Russian physicist Pavel Cherenkov (1934) discovered the Cherenkov light emitted by a beam of high-energy charged particles moving through a transparent medium at a speed greater than the speed of light in that medium. For example, light is moving in water at a speed that is only 75% of its speed in vacuum. Thus, it is throughout possible for high-energy particles (e.g. beta particles) to move faster than light in water. The effect is similar to a sonic boom, when an object moves faster than the speed of sound. Cherenkov light often appears bluish, since the Cherenkov effect is strongest for light with short wavelengths.

The idea of a material particle moving faster than the speed of light was difficult to grasp in those days, even for scientists. In fact, Cherenkov's English-language manuscript “Visible Radiation Produced by Electrons in a Medium with Velocities Exceeding that of Light” was rejected by Nature, whose editors did not take the work seriously. Fortunately, the Physical Review was more open-minded and accepted the paper.

Today, the Cherenkov effect is used in nuclear physics in the so-called Cherenkov detector for detecting and counting high-energy charged

particles. The particles pass through a liquid, and a photomultiplier tube registers the Cherenkov light.

50 Years of Penzias & Wilson's Cosmic Microwave Background: It is 50 years since Penzias and Wilson discovered the cosmic microwave background, evidence for the birth of the universe. In 1964 two American radio astronomers, Arno Penzias and Robert Wilson, were working at the Bell Labs in Holmdel, using the Horn Antenna to map signals across the Milky Way. The Holmdel Horn Antenna was a highly sensitive instrument originally built to detect faint radio waves, which had been deflected off satellites. In order for the antenna to work properly, all sources of interferences such as radio waves, radar and heat were removed. They still noticed a faint, persistent and ever-present noise emanating from every direction. It was not coming from a planet, the sun, or anywhere else in the Milky Way. As a result, the Wilson and Penzias logically conclude that the noise was originating from outside our galaxy.

50 Years of Charles Kao's Optical Fibre Technology:

It is 50 years since the development of fibre optic technology driven by the dramatic progression of telecommunications. Charles Kao is commonly referred to as the “Father of Fibre Optical Communications” due to his contribution to the field. As a result of his work, many high-quality commercial and industrial communication products have arisen which many now take for granted.

When light travelling through a medium hits the boundary of a new medium of different refractive index at an angle less than the critical angle, part of the light is refracted and part is reflected rather than being transmitted.

Kao found that an optical fibre is able to retain light propagating due to total internal reflection, whereby light is entirely reflected rather than being partly refracted. An optical fibre comprises of a transparent inner core made from silica or plastic, surrounded by cladding made from a material which has a low enough refractive index in order to ensure light waves are totally internally reflected in the fibre.

In 1966, Kao developed a fibre optic wire, which enabled signals to be transmitted over kilometre distances rather than just a few meters, as had

previously been the case. This wire was able to carry as much information as is contained in 200,000 phone calls or 200 television channels.

Themes:

An International year of Light allows the universality of light and the variety of its applications to be appreciated via many and varied themes covering broad areas of interest on national, regional and international levels. The official stated themes of the International Year of Light are:

Science of Light:

This theme highlights the fundamental scientific properties of light. Light science is one of the most accessible themes to promote cross-disciplinary education. Study of the fundamental scientific properties of light has impacted widely on all fields of science, technology and engineering. From early attempts to understanding the motion of stars and planets to the appreciation of the importance of light in photosynthesis, efforts to understand the nature and the characteristics of light have revolutionized nearly every field of science. Light from the Big Bang provides us with a vision of the origin of the universe. The spectrum of light from X-rays to infrared lasers provides technologies that underpin our lives, and the interaction of light with the human body provides valuable techniques for diagnostics, imaging and medical treatment.

Light Technology:

Light based technology, often referred to as photonics describes a range of applications aimed at directly raising the quality of life worldwide by reducing child mortality, improving maternal health and combating disease. Advanced research in areas such as nano-photonics, quantum optics and ultrafast science are inspiring new fundamental discoveries and opening new scientific frontiers.

Light itself underpins the existence of life, and light-based technologies directly respond to the needs of humankind by improving access to information, promoting sustainable development, increasing societal health and well being, and furthering environmental goals by saving energy and reducing global warming.

Light pulses and advanced optical fibre cables form the backbone of the global internet and satellite telephones and wireless technologies allow even the most remote areas of the world to have access to communications, information and even advanced medical care. Light technology is essential to improve society's energy independence through devices that efficiently convert sunlight to other energy forms and new forms of low cost green lighting.

Optical technologies are tremendously important for our daily lives. Corrective eyeglasses for improved vision are familiar to us all, and simple optical instruments such as microscopes form a cornerstone of modern medical diagnostics. The field of Green Photonics studies ways to apply light technology to generate energy and yield environmentally sustainable outputs. Light-based technology is a major economic driver with potential to revolutionize the 21st century as electronics did in the 20th century.

Light in Nature:

This theme focuses attention on the beauty and accessibility of science. The wonder of light and colour is revealed spectacularly in effects such as sunset, rainbows, halos and shadows to cite just a few examples of rich variety of optical phenomena, which can be found in nature. This theme will raise awareness of the beauty and accessibility of science through activities that will encourage and support observation of light and colour in Nature. It is easy and delightful to understand Nature through light: from ice crystals near the arctic to mirages in the desert, and from shadows in the forest to shifting images on water, the wonder and beauty of natural optics is everywhere.

Light and Culture:

This theme highlights the myriad ways in which light has influences and continues to influence human culture. From the early artists and scientists of Antiquity to the development of perspective and understanding of light and shadow during the Renaissance to impressionism and modern artistic techniques, this theme will describe how the study of light and art is central to understanding and appreciating our cultural heritage. Describing the continuous links between light and

culture throughout history will provide valuable insights into the interactions between science and art and the humanities in general.

This theme will also describe ways in which light can be used to improve our appreciation of cultural heritage in ways such as applying optical techniques to image paintings, the use of modern technology in museums to experience culture in an interactive environment and the use of natural light and low-pollution lighting to illuminate architecture, monuments and public spaces.

This theme will provide an important bridge between science and culture and will aid in breaking down the boundaries between the fields that are becoming increasingly separated in the modern world.

Mission:

The International year of light, a global initiative will highlight to the citizens of the world the importance of light and optical technology in their lives, for their future and for the development of society.

Activities will be planed so that people of all ages and with all backgrounds from all countries enjoy and appreciate the central role of light in science and culture, and as a cross-cutting scientific discipline that can advance sustainable development

Motivation:

Light is one of the main messengers in our understanding of the universe and the subatomic world. An International Year of Light is the ideal instrument to ensure the necessary increased worldwide awarenesss of the central role of light in the present and in the future. An International Year of Light will contribute significantly to fulfilling the missions of UNESCO to the building of peace, the alleviation of poverty, to sustainable development and intercultural dialogue through education, science, culture and communication.

Curr. Rep. Sci. & Tech. 1 (2) (2015) 12-20

Effect of Replacing Oxide with Fluoride Anion on the Physical and Spectroscopic Properties of Nd^{3+} Doped Borate Glasses

Shaweta Mohan
Department of Physics, BBK DAV College for Women, Amritsar (India)
shwetamohan_82@yahoo.co.in

Abstract

Physical and spectroscopic properties of Nd^{3+} doped oxide and fluoride glasses of the type 20 Na_2O30 PbO49.5 $B_2O_3$0.5 Nd_2O_3 and 20 NaF30 PbO49.5 $B_2O_3$0.5 Nd_2O_3 have been investigated. Optical absorption spectra and Judd-Ofelt theory has been used to determine the oscillator strengths and the intensity parameters Ω_2, Ω_4 and Ω_6. The radiative transition probability (A), radiative lifetime (τ_R) and branching ratio (β_R) for the fluorescent levels have been determined. The lasing efficiency of the prepared glasses has been characterized by the spectroscopic quality factor (Ω_4/Ω_6), the value of which is in the range 0.2-1.5, typical for Nd^{3+} in different laser hosts. The radiative transition probability of the potential lasing transition $^4F_{3/2} \rightarrow {}^4I_{11/2}$ of Nd^{3+} ions is found to be higher for oxide based glass as compared to the glass with fluoride ion.

Keywords

Glasses, Judd-Ofelt Analysis, Laser materials, Optical properties

I. Introduction

Borate glass is a suitable optical material with high transparency, low melting point, high thermal stability and good rare-earth ions solubility [1, 2]. It can produce glasses both for scientific and technological applications. The addition of alkali oxides to borate glass can improve its physical properties as well as modify their preparation conditions. RE-doped binary alkali borate glasses are not only important for optical applications, but also form an interesting class of glasses to study the effect of the alkali ion on the

glass forming network, particularly around the rare-earth ions. Optical properties of rare earth ion doped alkali and mixed alkali borate glasses have been studied in the recent years [3-7]. Ratnakaram et al. have reported the spectroscopic properties of Nd^{3+} ions in fluoroborate and chloroborate glasses [8]. Patek [9] has explained the operating characteristics of lasing ions and how their spectroscopic and lasing properties can be varied by changing the host glass composition. The spectroscopic properties and optical properties of rare earth ions depend on the chemical composition of the glass which determine the local structure at the rare earth sites and the distribution of the doped ions in the glass matrix.

The aim of the present work is to study how the replacement of oxide ion with fluoride ion modifies the spectroscopic properties of the neodymium doped borate glass. Studies on Nd^{3+} ion has been undertaken, since it is a potential laser ion and also neodymium lasers can operate with high efficiency, even at room temperature.This work is an effort to possibly compare an oxide and fluoride ion to meet the needs of laser designer.

II. Experimental

This The following two glasses of the composition

BO 20 NaX-30 PbO-49.5 $B_2O_3$0.5 Nd_2O_3

And

BF 20 NaF-30 PbO-49.5 B_2O_3-0.5 Nd_2O_3

were prepared by the melt quenching technique. All the chemical raw materials used in preparing above mentioned glass series Na_2CO_3, PbO, B_2O_3, NaF and Nd_2O_3 were of high purity (99.9%).

The densities of the prepared samples were determined by using Archimedes' principle with benzene as the immersion liquid (buoyant). It was calculated using the following formula

$$\frac{W_a}{W_a \quad W_b} \qquad {}_b \tag{1}$$

where W_a is the weight in air, W_b is the weight in buoyant and ρ_b the density of buoyant. The refractive indices of the prepared glasses were measured ~ at 30°C using an Abbe refractometer with mono-bromonaphthalene as an

adhesive coating. The estimated error is ±0.001. Optical measurements were performed using a UV-VIS double-beam spectrophotometer (Shimadzu 160-A, Japan) in the range 200-1100 nm.

III. Theory

A. Physical properties

Physical properties such as molar volume, ion concentration N, polaron radius r_p (Å), field Strength F, inter nuclear distance r_i (Å) were determined using standard formulae [10].

B. Oscillator Strength and Judd-Ofelt parameters

This Judd-Ofelt formalism [11, 12] is a semi-empirical method that analyzes the absorption spectra of trivalent rare earth ions in crystals and glasses and has proved to be a powerful tool for the systematic investigation and selection of these materials for specific purposes.

The oscillator strength (f) is a dimensionless quantity which is related to the quantum probability of a transition and hence gives the intensity of absorption band corresponding to that particular transition.

From the absorption spectra, the oscillator strength of each absorption band can be determined experimentally from the area under the absorption band and can be expressed in terms of absorption coefficient α at a particular wavelength λ by [13]:

$$f_{meas} = 4.32 \times 10^{-9} \int_{\nu_1}^{\nu_2} \varepsilon(\nu)\, d\nu \qquad (2)$$

where is the molar extinction coefficient at mean energy ν (cm^{-1}) and it represents the area under an absorption peak, OD being the optical density, c is the concentration of rare earth ions in moles/lt. and d is the optical length of the glass in cm.

As given by Judd-Ofelt theory, the theoretical oscillator strengths, f_{cal} of a transition between an initial J manifold $|(S, L)J\rangle$ and a final J′ manifold $|(S'; L')J\rangle$ can be given by :

$$f_{cal}(aJ, bJ') = \frac{8\pi^2 mc\nu}{3h(2J+1)}\left[\frac{(n^2+2)^2}{9n} S_{ed} + nS_{md}\right], \qquad (3)$$

where :

$$S_{ed}[(S,L)J : (S',L')J'] = \sum_{\lambda=2,4,6} \Omega_\lambda \left|\left\langle (S,L)J \left\| U^{(\lambda)} \right\| (S',L')J' \right\rangle\right|^2 \qquad (4)$$

is the line strengths for electric dipole transitions, respectively. Since the bands that are produced by magnetic dipole mechanism have very low spectral intensity compared to that of the electric dipole bands, S_{md} is not considered. $\left|\left\langle (S,L)J\left\|U^{(\lambda)}\right\|(S',L')J'\right\rangle\right|^2$ are the doubly reduced matrix elements of the unit tensor operator of rank λ=2, 4 and 6 connected the initial and final states. The matrix elements computed for free hosts, as reported by Carnall et al. [14] have been used for the calculations. The best set of values of Ω_2, Ω_4 and Ω_6 parameters are determined by a standard least square fitting between the theoretical oscillator strength fcal and the experimental oscillator strength f_{exp} values.

The rms deviation between the experimental and calculated oscillator strengths is defined as:

$$rms\,\Delta f = \sqrt{\frac{\sum_{i=1}^{L}(f_{\exp} - f_{cal})^2}{L-3}} \tag{5}$$

where L is the number of absorption bands taken into account for the above calculations.

C. Radiative properties

The radiative transition probability also known as spontaneous emission rate for the emission from initial state to a final state is given by [15]

$$A(aJ,bJ') = \frac{64\pi^4 e^2}{3h\lambda_o^3(2J+1)}\frac{n(n^2+2)^2}{9}\sum_{\lambda=2,4,6}\Omega_\lambda\left|\left\langle (S,L)J\left\|U^{(\lambda)}\right\|(S',L')J'\right\rangle\right|^2 \tag{6}$$

The total radiative emission probability of an excited state is given by the sum of the terms calculated over all the terminal states.

$$A_T(aJ) = \sum_{bJ'} A(aJ,bJ') \tag{7}$$

The fluorescence branching raito β_R is given as

$$\beta_R = \frac{A(aJ,bJ')}{A_T(aJ)} \tag{8}$$

The radiative lifetime τ_R of the emission state is given as

$$\tau_R = \frac{1}{A_T(aJ)} \tag{9}$$

IV. Results And Discussion

A. Physical properties

The physical properties of the prepared glasses are listed in Table 1. Density of glass BO is found to be less than BF glass. This is because the replacement of smaller fluorine ions by larger oxide ions results in an increase in molar volume which offsets the increase in atomic weight and causes a decrease in density of the glass [16]. The higher density of BF glass attributes to it an increased number of Nd^{3+} ions per unit volume as compared to oxide glass. Due to larger number of rare earth ions, the inter-nuclear distance of Nd^{3+} ions in BF is less than oxide glass.

The field strength of Nd^{3+} ions is greater in flouroborate glass because of its greater density in comparison to oxide glass. Replacement of fluoride ions by more polarizable oxide ions results in an increase in refractive index [16]. Thus, the refractive index of BO is more than BF glass.

Table 1. Physical properties of prepared glasses

Physical property	BO	BF
Density (ρ) (g/cm^3)	4.18	4.59
Average molecular weight ($\overline{M}$) (g)	115.49	111.50
Molar Volume (V_M) (cm^3)	27.58	24.24
Ion concentration N ($\times 10^{20}$ ions/cm^3)	2.18	2.48
Ion concentration c (moles/liter)	0.36	0.41
Polaron radius r_p (Å)	6.69	6.41
Field Strength F ($\times 10^{14}$cm^2)	6.70	7.30
Inter nuclear distance r_i (Å)	16.60	15.90
Refractive index (n)	1.652	1.650
Dielectric constant (ε)	2.73	2.72
Molar refraction (R_M)	10.08	8.84
Reflection losses (R %)	6.04	6.01

B. Spectral intensities and Judd-Ofelt parameters

The optical absorption spectrum of the BO glass is shown in Fig. 1. The absorption bands of Nd^{3+} correspond to transitions from $^4I_{9/2}$ ground state to various excited states. These transitions were assigned by comparing the spectra with the standard wavelength chart of Nd^{3+} [17]. Experimental (f_{exp}) and calculated (f_{cal}) values of oscillator strengths, which give the intensity of absorption bands are presented in Table 2. The rms deviations between experimental and calculated values are within the experimental limit, thus confirming the validity of the Judd-Ofelt theory. It

is observed that the spectral intensity of the hypersensitive transition $^4I_{9/2} \rightarrow {}^4G_{5/2} + {}^2G_{7/2}$ is more for BO as compared to BF glass.

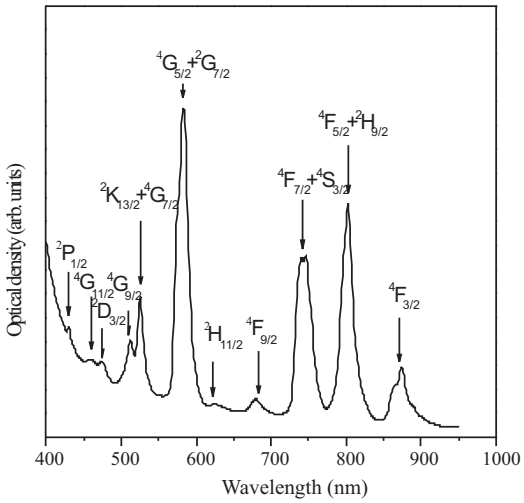

Fig1.Optical absorption spectra of BO glass.

The JuddOfelt parameters Ω_2, Ω_4 and Ω_6 calculated using the oscillator strengths and reduced matrix elements are also presented in Table 2. The table also includes the spectroscopic quality factor (Ω_4/Ω_6), which determines the lasing efficiency of the host. The intensity parameter Ω_2, which is generally related with the covalency of the metal-ligand bond, is greater for oxide glass (BO) as compared to fluoride (BF) glass. This result agrees with the higher intensity of hypersensitive transition. The Stark splitting of the hypersensitive transition $^4I_{9/2} \rightarrow {}^4G_{5/2} + {}^2G_{7/2}$ is poorly resolved as observed in previous studies. Hence a variation of the spectral profile of the transition $^4I_{9/2} \rightarrow {}^4F_{7/2}$, $^4S_{3/2}$ is investigated. The peak intensity ratio of the longer (IL) and shorter (IS) wavelength components designated as IL/ISis higher for BF as compared to BO glass. A higher value of Ω_6 parameter for BO confirms this result.

C. Radiative properties

Radiative properties such as radiative transition probability (A), total transition probability (A_T), radiative lifetime (τ_R) and branching ratio (β_R) for the excited $^4F_{3/2}$ of fluorescence levels of Nd^{3+} ion in the prepared glasses are summarized in Table 3. It is observed that the radiative transition

probability of the potential lasing transition $^4F_{3/2} \rightarrow {}^4I_{11/2}$ of Nd^{3+} ions is higher for BO glass as compared to BF. The total radiative probability is also higher for the oxide glass as compared to the fluoride glass (BF). This imparts a lower radiative lifetime to BO glass. A higher radiative transition probability and low radiative lifetime are required for high radiative quantum efficiency of a laser material.

Table 2.*Oscillator strengths and Judd-Ofelt parameters*

Transitions from ground state $^4I_{9/2}\rightarrow$	**BO**		**BF**	
	f_{exp}	f_{cal}	f_{exp}	f_{cal}
$^4F_{3/2}$	2.99	3.08	3.37	2.85
$^4F_{5/2}+{}^2H_{9/2}$	9.54	9.60	8.24	9.43
$^4S_{3/2}+{}^4F_{7/2}$	9.78	9.77	10.30	9.87
$^4F_{9/2}$	1.17	0.73	1.49	0.71
$^2H_{11/2}$	0.92	0.22	1.05	0.21
$^4G_{5/2}+{}^2G_{7/2}$	25.03	25.02	22.41	22.42
$^2K_{13/2}+{}^4G_{7/2}$	4.66	4.76	4.51	4.40
$^4G_{9/2}$	2.29	2.00	2.89	1.90
$^2D_{3/2}+{}^2G_{9/2}$	1.74	0.99	1.78	1.25
$^4G_{11/2}$	1.38	0.29	1.34	0.26
$^2P_{1/2}$	1.31	0.79	1.46	0.71
rms deviation	±0.59		±0.68	
$\Omega_2(\times10^{-20}\ cm^2)$	5.31		4.84	
$\Omega_4(\times10^{-20}\ cm^2)$	5.67		5.31	
$\Omega_6(\times10^{-20}\ cm^2)$	6.40		6.32	
Ω_4/Ω_6	0.88		0.78	
I_L/I_S	1.032		1.052	

Table 3.*Radiative properties of prepared glasses*

Transitions from $^4F_{3/2}\rightarrow$	**BO**		**BF**	
	$A(s^{-1})$	β_R	$A(s^{-1})$	β_R
$^4I_{15/2}$	22	0.005	22	0.005
$^4I_{13/2}$	422	0.096	427	0.102
$^4I_{11/2}$	2101	0.481	2077	0.494
$^4I_{9/2}$	1820	0.417	1673	0.398
$A_T(s^{-1})$	4366		4199	
$\tau_R(\mu s)$	229		238	

V. Conclusions

The physical and spectroscopic studies on Nd^{3+} doped sodium lead oxide and fluoride borate glasses were conducted. Smaller size of fluoride ion imparts a higher density and increased number of Nd^{3+} ions to the

respective glass. Because of the higher value of Ω_2 parameter, the covalency of the metal-ligand bond is more oxide glass as compared to BF glass. The radiative transition probability of the potential lasing transition $^4F_{3/2} \rightarrow {}^4I_{11/2}$ of Nd^{3+} ions is higher for BO glass as compared to BF. Thus, BO is more suitable for lasing transition as compared to BF glass.

VI. References

[1] N. Soga, K. Hirao, M. Yoshimoto and H. Yamamoto, Effects of Densification on Fluorescence Spectra and Glass Structure of Eu3+ Doped Borate Glasses, J. Appl. Phys. 63 (1988) 4451-4454.

[2] S. M. Kaczmarek,$Li_2B_4O_7$ Glasses doped with Cr, Co, Eu and Dy, Opt. Mat., 19 (2002) 189-194.

[3] R. Balda, J. Fernandez, M. Sanz, A. de Pablos, J. M. Fdez-Navarro and J-Mugnier, Laser Spectroscopy of Nd^{3+} ions in GeO_2-PbO-Bi_2O_3 Glasses, Phys. Rev.B, 61 (2000) 3384-3390.

[4] A. Speghini, M. Peruffo, M. Casarim, D. Ajo and M. Bettinelli, Electronic Spectroscopy of Trivalent Lanthanide Ions in Lead Zinc Borate Glasses, J. Alloys Compd., 300 (2000) 174-179.

[5] M. B. Saisudha, J. Ramakrishna, Phys. Effect of Host glass on the Optical Absorption Properties of Nd^{3+}, Sm^{3+} and Dy^{3+} in Lead Borate Glasses Rev. B, 53 (1996) 6186-6196.

[6] W. Soppe, J. Kleerebezem and H.W. den Hartog, "Raman Spectroscopy Study of $(B_2O_3)_{1-x-y}(Li_2O)_x(Li_2Cl_2)_y$ and $(B_2O_3)_{1-x-y}(Li_2O)_x(Cs_2O)_y$, J. Non-Cryst. Solids, 93 (1987) 142-154.

[7] N. A. Sharaf, A. A. Ahmed, A. F. Abbas, Mixed Alkali Effect on Density, Refractive index and Related Properties of Alkali Borate Glasses, Phys. Chem. Glasses, 39 (1998) 76-82.

[8] Y.C. Ratnakaram and A. Viswanadha Reddy, "Electronic Spectra and Optical Band gap Studies in Neodymium Chlorophosphate Glasses, J. Non Crys. Solids, 277 (2000) 142-154.

[9] K. Patek, Glass Lasers, Butter Worth, London, (1970).

[10] A.S. Rao, Y. N. Ahammed, R. R. Reddy, and T. V. R. Rao, Spectroscopic Studies of Nd^{3+}-doped Alkali Fluoroborophosphate Glasses, Opt. Mater.10 (1998) 245-252.

[11] B. R. Judd, Optical Absorption Intensities of Rare-Earth Ions, Phys. Rev., 127 (1962) 750-761.

[12] G. S. Ofelt, Intensities of Crystal Spectra of Rare-Earth Ions, J. Chem. Phys., 37 (1962) 511-520.

[13] W.T.Carnall, P.R. Fields and K. Rajnak, Electron Energy Levels in the Trivalent Lanthanide Aquo Ions. I. Pr^{3+}, Nd^{3}+Sm^{3+}, Dy^{3+}, Ho^{3+}, Er^{3+}, and Tm^{3+}, J. Chem. Phys., 49 (1968) 4424-4442.

[14] W.T. Carnall, J.P. Hessler and F. Wagner, Transition Probabilities in the Absorption and Fluorescence Spectra of Lanthanides in Molten Lithium Nitrate -Potassium Nitrate Eutectic, J. Phys. Chem., 82 (1978) 2152-2158.

[15] D. C. Brown, High Peak Power Nd: Glass Laser Systems, Springer, Berlin, (1981).

[16] J. E. Shelby, Introduction to Glass Science and Technology, The Royal Society of Chemistry, Cambridge (1997).

[17] G. H. Dieke, Spectra and Energy Levels of Rare Earth Ions in Crystals, Interscience, New York (1968) 56.

Curr. Rep. Sci. & Tech. 1 (2) (2015) 21-28

Germination and Early Biochemical Responses In *Brassica campestris* L. To Pre-Soaking Chilling Treatment

Kirandeep Kaur Hundal and Navkiran Randhawa
P.G. Department of Botany, Khalsa College, Amritsar (India)
hundal_kiran@ymail.com

Abstract

Seed germination occupies a unique position in plant life. Low temperature has a strong impact on survival, growth and development of seedlings. The present investigation was carried out to study the influence of cold treatment of 0ºC and 4ºC for 24hrs and 48 hrs on various characteristics of seeds of Brassica campestris L. The percent germination of seeds, radicle and plumule length, fresh weight and dry weight of seedlings were significantly influenced by various chilling treatments as compared to control. There was significant increase in the level of biochemical reserves due to cellular and metabolic changes that occurred during cold acclimatization.

Key words

Abiotic stress, chilling injury, Germination potential, chilling treatment

I. Introduction

Brassica campestris is a cold seasoned crop which frequently faces cold temperature [1]. The plants of oleiferous Brassica seeds produce heteromorphic seeds, varying in size and germination potential. Many factors affect the growth and development of plant. Seeds are the primary and essential starting point for agronomic important plants [2]. Germination test is the most widely used test for seed viability. Seed germination is an essential process in plant development to obtain optimal seedling number that result in high seed. Seed vigour is the end result of

various properties that determine potential for rapid,uniform emergence and development of healthy seedlings. Various external and internal factors affect the morphological, physiological, biochemical and anatomical parameters. Among these factors chilling stress has been shown to have profound effect on various morphological and biochemical parameters of seedlings.

II. Material And Methods

The seeds of *Brassica campestris* L. were procured from the Department of Plant Breeding and Genetics, Punjab Agricultural University, Ludhiana, Punjab. The experiment was conducted in P.G. Department of Botany, Khalsa College, Amritsar. Seeds were hand separated, graded and uniform seeds were surface sterilized with 0.1% mercuric chloride for one minute, followed by thorough washing with distilled water. The seeds were soaked in distilled water in beakers and kept at 0ºC and 4ºC (in refrigerator) for 24hrs and 48hrs respectively. The seeds were then sown in sterilized petriplates in three replicates. One set of petriplates containing seeds was kept as control (No chilling treatment). The petriplates were kept in seed germinator at 80% relative humidity. Data was recorded on various morphological parameters like germination percentage, radicle length and plumule length of seedlings after different intervals of time i.e. 24hrs to 192hrs. Physiological parameters include fresh weight, dry weight and moisture content of the seedlings. Biochemical reserves viz. total Soluble Sugars, Starch [3] and Total Soluble Proteins [4] were also estimated in seedlings.

A. Morphological Parameters

a. Germination Percent

The number of seeds germinated after different intervals of time were counted in control as well as in chilling stress treated petriplates.

$$\text{Germinatio n Percent} = \frac{\text{No. of seeds germinated}}{\text{Total No. of seeds sown}} \times 100$$

b. Radicle Length And Plumule Length (Cm)

It was determined with the help of scale.

B. Physiological Parameters

a. Fresh Weight, Dry Weight and Moisture Content of Seedlings

Fresh weight of the seedlings was taken after different intervals of time by weighing them on a balance and for dry weight estimation, the same seedlings were kept in oven at 100ºC for 72 hours and weighed.

$$\text{Percent Moisture Content} = \frac{\text{Fresh Weight - Dry Weight}}{\text{Dry Weight}} \times 100$$

b. Total Soluble Sugars (Dubois et al 1956):

Extraction:100 mg of randomly collected seedling tissue was homogenized in 80% ethanol and centrifuged at 3000 rpm for 15 minutes. The extraction procedure was repeated twice. The supernatants were pooled and then ethanol was evaporated. The final volume was adjusted to 50 ml with distilled water. This extract was used for estimation of total soluble sugars and expressed in mg/g fw.

Procedure: To 0.2 ml of extract, 1 ml of 5% phenol was added. The solution was kept for 10 minutes followed by addition of 5 ml of chilled concentrated H_2SO_4 with constant shaking. After 10 minutes, the tubes were cooled to room temperature under running tap water. The absorbance was recorded at 490 nm against 80% ethanol as blank. The concentration of total soluble sugars (as glucose) was calculated from glucose standards run simultaneously and the total soluble sugar content was expressed as mg g -1 fresh weight.

c. Total Soluble Starch:

Starch was estimated by method as given by (Dubois et al 1956) from randomly selected leaves. 100 mg of fresh tissue sample was homogenized with 80% ethyl alcohol. Centrifuged and retained the residue, washed with 80% ethyl alcohol 4-5 times to remove all traces of soluble sugars. 5 ml of distilled water followed 6.5ml of 52% perchloric acid was added. Kept at 0oC for 20 minutes, centrifuged and retained the extract. Repeated same step 3-4 times and diluted to the desired volume. Took 0.1ml of diluted extract in a test tube added 0.9 ml of distilled water and 1ml of phenol. Add 5ml of chilled H_2SO_4. It was cooled at room temperature for 30 minutes. For blank, 1ml phenol, 1ml distilled water and 5 ml of H_2SO_4 is used. Absorbance was recorded at 490 nm.

d. Total Soluble Protein Content:

The protein content was determined by the method of (Lowry et al1951) and values were expressed in mg g-1 fresh weight of plant tissue.

III. Results And Discussion

Fig. 1 shows that the germination potential was significantly affected by various presoaking chilling treatments. All the chilling treatments caused significant increase in the germination of the seeds. Maximum increase was with 4ºC for 48hrs. This data is similar to the findings reported in chickpea [5].

A. Radicle length and Plumule length (cm) of the seedlings

Fig. 2 and Fig. 3 show the effect of chilling treatment on radicle length and plumule length of the seedlings. There was marked enhancement in the radicle length of seedlings given chilling stress treatment at different intervals of time as compared to control. Seedlings which were subjected to stress at 0ºC for 24hrs had significant increase in length of radicle as compared to seedlings subjected to stress at 0ºC for 48hrs, likewise chilling treatment at 4ºC for 24hrs also caused significant enhancement in radicle length of the seedling but % age increase was less than that at 0ºC treatment (Fig. 2). Similar trend was observed in the plumule length of the seedlings. There was marked reduction in radicle length and plumule length of seedlings subjected to chilling stress at 4ºC for 48hrs (Fig. 3).

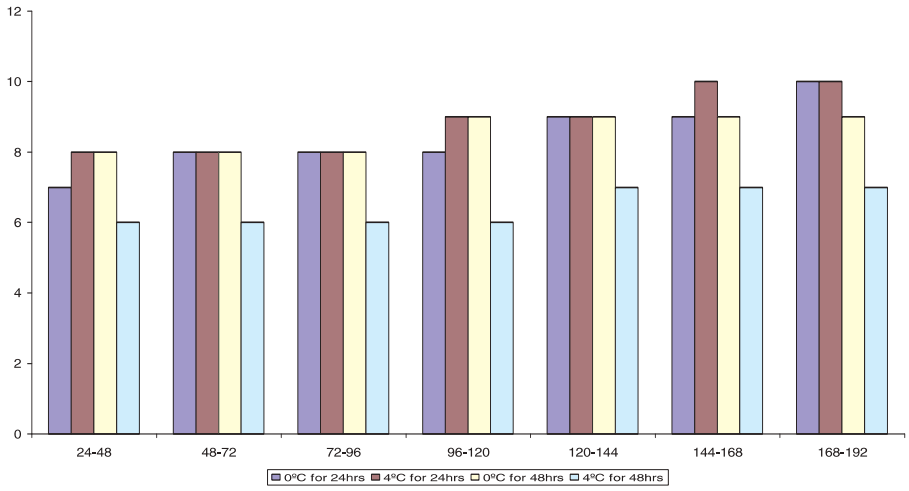

Fig 1. *Effect of presoaking chilling stress of 0° C and 4° C for 24 hrs and 48 hrs on germination potential (%) of seedlings of Brassica campestris L.*

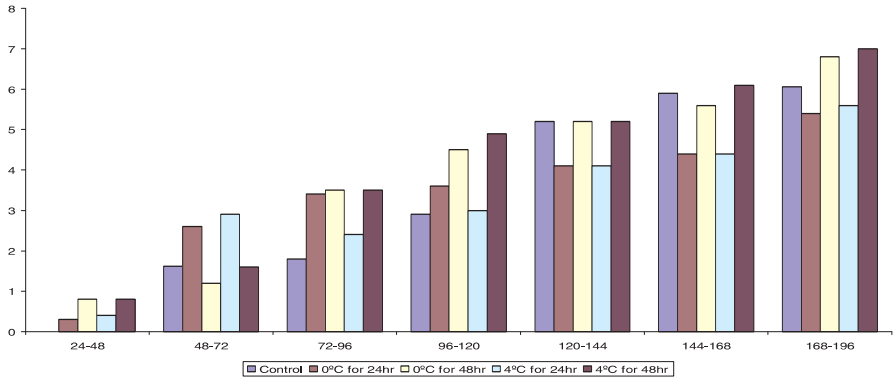

Fig 2. *Effect of presoaking chilling stress of 0° C and 4° C for 24 hrs and 48 hrs on plumule length (cm) of seedlings of Brassica campestris L.*

B. Physiological Parameters

Fresh Weight, Dry Weight and Moisture Content also showed marked variation with various stress treatments. Table 1 shows that there was significant increase in the fresh weight of seedlings at 0ºC for 24, 48hrs and 4ºC for 24hrs, but there was reduction in the fresh weight following stress treatment at 4ºC for 48hrs. The dry weight was also affected in the similar trend. Moisture content was significantly higher in chilling treated seedlings as compared to control. Fresh weight (FW) is related to tissue volume, decrease in fresh weight represents increase in the leaf thickness. Decrease in dry weight indicate transient dry matter accumulation and for increased cell wall thickness [6].

C. Biochemical Reserves

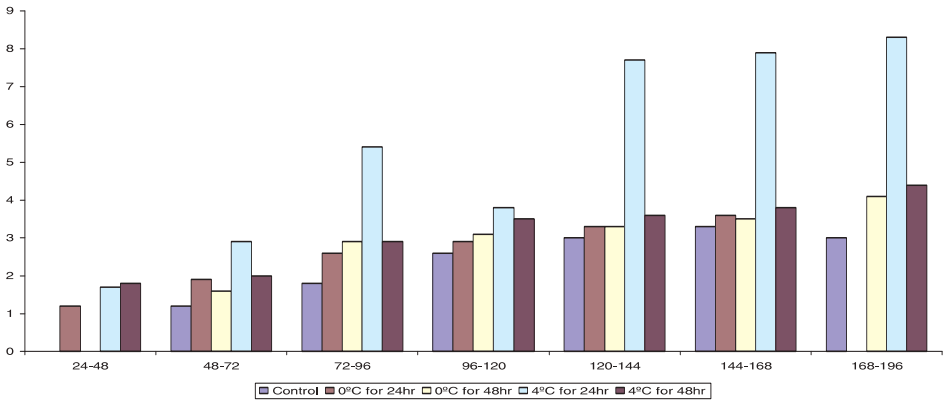

Fig 3. *Effect of presoaking chilling stress of 0° C and 4° C for 24 hrs and 48 hrs on radicle length (cm) of seedlings of Brassica campestris L.*

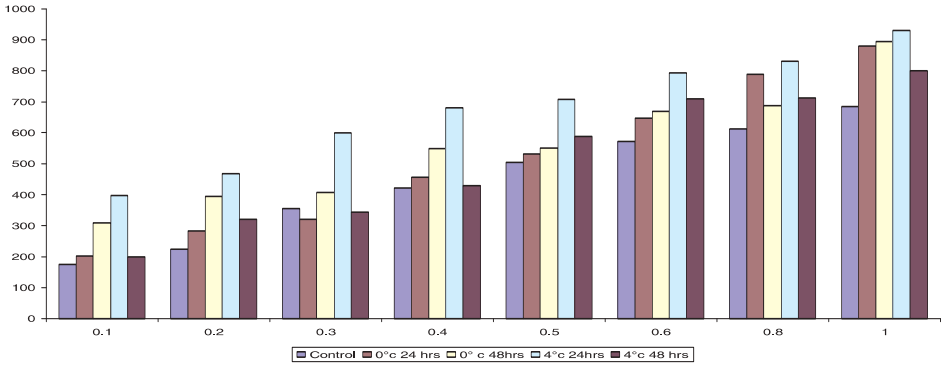

Fig 4. *Effect of presoaking chilling stress of 0° C and 4° C for 24 hrs and 48 hrs on Soluble sugars of seedlings of Brassica campestris L.*

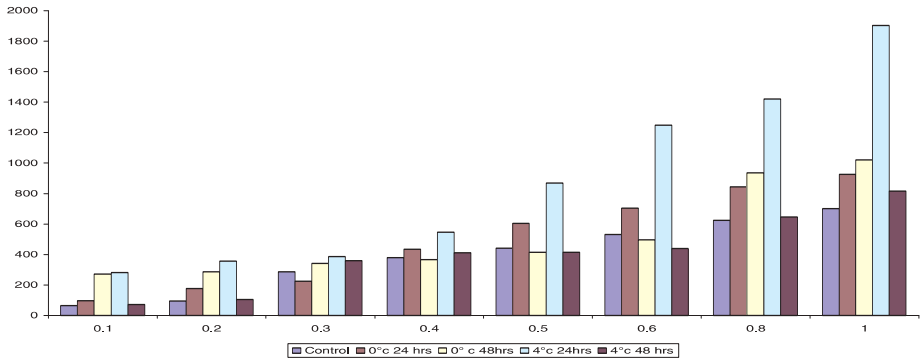

Fig 5. *Effect of presoaking chilling stress of 0° C and 4° C for 24 hrs and 48 hrs on Soluble starch of seedlings of Brassica campestris L.*

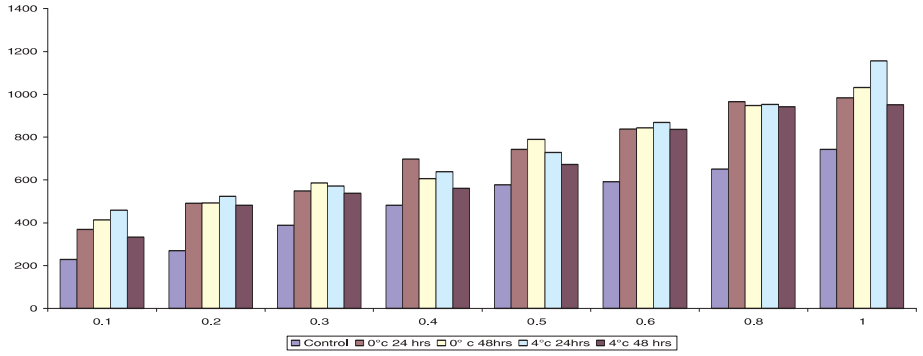

Fig 6. *Effect of presoaking chilling stress of 0° C and 4° C for 24 hrs and 48 hrs on Soluble proteins of seedlings of Brassica campestris L.*

Chilling treatment also resulted in marked variation in levels of various biochemical reserves of seedlings like total soluble sugars, starch and total soluble proteins. Fig. 4, 5, and 6 showed that as compared to

Table 1: Effect of Pre Soaking Chilling Stress of 0°c And 4°c For 24hrs and 48hrs on Fresh Weight (G), Dry Weight (G) And Moisture Content (%) In Seedlings of Brassica campestris L.

Time Internal	0°c for 24hrs			0°c for 28hrs			0°c for 24hrs			0°c for 28hrs		
	Fresh weight	Dry weight	Moisture content	Fresh weight	Dry weight	Moisture content	Fresh weight	Dry weight	Moisture content	Fresh weight	Dry weight	Moisture content
24 - 48	0.379 ±0.01	0.035 ±0.02	982.8	0.29 ±0.04	0.010 ±0.02	2800	0.477 ±0.02	0.053 ±0.03	800	0.46 ±0.01	0.019 ±0.03	2321.1
48 - 72	0.400 ±0.03	0.040 ±0.04	900	0.23 ±0.02	0.012 ±0.01	1816.6	0.281 ±0.04	0.032 ±0.02	778.1	0.38 ±0.04	0.014 ±0.02	2614.3
72 - 96	0.047 ±0.02	0.040 ±0.03	917.5	0.34 ±0.01	0.023 ±0.03	13.8	0.312 ±0.01	0.034 ±0.04	817.6	0.45 ±0.01	0.021 ±0.01	2042.8
96 - 120	0.449 ±0.01	0.036 ±0.01	1147.2	0.21 ±0.03	0.011 ±0.04	1809.0	0.320 ±0.03	0.035 ±0.02	814.3	0.63 ±0.04	0.024 ±0.04	2525
120 - 144	0.423 ±0.03	0.043 ±0.04	883.7	0.20 ±0.02	0.014 ±0.02	1328.5	0.288 ±0.04	0.015 ±0.03	1820	0.41 ±0.03	0.019 ±0.01	2057.9
144 - 168	0.470 ±0.04	0.041 ±0.02	1046.3	0.29 ±0.04	0.020 ±0.04	1350	0.259 ±0.02	0.013 ±0.01	1892.3	0.63 ±0.02	0.023 ±0.03	263.9.1
168 - 192	0.474 ±0.02	0.336 ±0.01	1216.6	0.36 ±0.02	0.017 ±0.03	2017.6	0.394 ±0.03	0.044 ±0.04	795.4	0.54 ±0.01	0.026 ±0.04	1976.9
192 - 216	0.441 ±0.01	0.046 ±0.03	858.7	0.35 ±0.01	0.026 ±0.01	1246.2	0.474 ±0.01	0.048 ±0.03	887.5	0.48 ±0.03	0.021 ±0.02	2185.7
216 - 240	0.451 ±0.01	0.035 ±0.01	1188.6	0.41 ±0.04	0.011 ±0.02	3627.3	0.437 ±0.02	0.032 ±0.01	1265.6	0.44 ±0.04	0.014 ±0.03	3042.8
240 - 264	0.578 ±0.04	0.037 ±0.02	1462.2	0.43 ±0.02	0.031 ±0.04	1287.1	0.569 ±0.04	0.041 ±0.02	1287.8	0.43 ±0.01	0.023 ±0.02	1769.6

Significant at 5% level, values represent mean + S.E.

control, the level of all the reserves were significantly enhanced by chilling treatment at 0ºC for 24hrs, 48hrs and 4ºC for 24hrs. But the stress at 4ºC for 48hrs caused a marked reduction in level of various reserves. The percentage increase in the level of total soluble sugars in case of seedlings given presoaking chilling treatment at 0°C for 24hrs 0°C for 48hrs and 4°C for 24 hrs was 4.51%, 2.78% and 0.95% respectively as compared to the control but the level showed a marked reduction in seedlings given stress treatments at 4°C for 48hrs (Fig. 4).

Similar trend was observed in the level of starch content (Fig. 5). The protein content was significantly enhanced as compared to the level of total soluble sugars and starch. The percentage increase in seedlings subjected to stress of 0°C for 24hrs, 0°C for 48hr and 4°C for 24hrs was 30.5%, 25.41% and 15.77% respectively as compared to control but the seedlings given 4°C for 48 hrs stress treatment showed a significant reduction in level of protein content as compared to control (Fig. 6). Cold stratification break dormancy of viable seeds and enhance germination in many crops [7].

Cellular and metabolic changes that occur during cold acclimatization include increase level of biochemical reserves [8]. Our data corroborated these studies. To conclude, Chilling Treatment led to enhancement in germination indices viz. Germination percent, radical and plumule length,

as well as physiological traits like dry and fresh weights of seedlings, moisture content in *Brassica campestris* L. seeds. Biochemicals like total soluble sugars, starch and protein showed significant alleviation in pre-treated seeds. This is acclimation of seeds by morpho-physiological and biochemical alterations in response to pre-soaking chilling treatment. However, treatment with 0°C for 24 hours proved most appropriate temperature and time period for enhancement in germination and biochemical traits in *Brassica campestris* L.

IV. Acknowledgement

Sincere gratitude to P.G Department Botany, Khalsa College, Amritsar for providing with required facilities to conduct the research

V. References

[1] O.Kurt, "Effects Of Chilling On Germination in Flax (L. usitatissimum L.)"Turk. J. Field Crops2 (2010) 153-169.

[2] M. Kumar, G. Sirhindi, R. Bhardwaj, S. Kumar, and G. Jain, "Effect of exogenous H2O2 on antioxidant enzymes of Brassica campestris L. seedlings in relation to 24-epibrassinolide under chilling stress" Indian J. Biochem. Biophys.47 (2010) 378-382.

[3] M. Dubois, K. A. Gilles, J. K. Hamilton, P. A. Roberts and F. Smith, "Calorimetric methods for the determination of sugars and related substances" Analyt. Chem.28 (1965)350-356.

[4] O. H. Lowry, N. J. Rosenbrough, A. L. Farr and R. J. Randall, "Protein measurement with Folin-Phenol reagent" J. Biol. Chem.193 (1951) 265-275.

[5] A. Chohan, "Comparative studies on morphological and biochemical characteristics of chickpea genotypes under chilling stress" J. Environ. Biol. 38 (2011) 189-194.

[6] Z. Lu and P. M. Neumann, "Low cell wall extensibility can limit maximum leaf growth rates in rice" Crop Sci. 39 (1999) 126-130.

[7] M. A. Hughes and M. A. Dunn,"The molecular biology of plant acclimation to low temperature", J. Exp. Bot.72 (1996) 291-305.

[8] M. Nkomo and L. Kambizi, "Effects of pre-chilling and temperature on seed germination of CorchorusolitoriusL. (Tiliaceae) (Jew's Mallow), a wild leafy vegetable"Afr. J. Biotech. 8 (2009) 1078-1081.

Curr. Rep. Sci. & Tech. 1 (2) (2015) 29-37

Photon Interaction Parameters for ZnO-Al_2O_3-Fe_2O_3-P_2O_5 Glass Systems

Preet Kaur, Tejbir Singh and Devinder Singh
Department of Physics, Sri Guru Granth Sahib World University,
Fatehgarh Sahib (India)
preetkaur_020@yahoo.com

Abstract

Gamma radiations are used in numerous applications such as for sterilizing medical equipments, medical diagnostics and radiation therapy, food processing (irradiation), non-destructive techniques for elemental analysis, for metallic castings or welds in oil pipelines etc. However, the longer exposure to these highly penetrating gamma rays to living tissues can result in mutation, radiation sickness, cancer and even death. In the present study, various photon interaction parameters such as mass attenuation coefficient, effective atomic number, half value layer, mean free path and electron density of $15ZnO$-$(17.5-x)Al_2O_3$- xFe_2O_3-$67.5P_2O_5$ glass systems ($x=0$, 7.5, 12.5, 17.5) and $15ZnO$-$(25-x)Al_2O_3$- xFe_2O_3-$60P_2O_5$glass systems ($x=0$, 25) have been investigated for photon energies of 1KeV to 100GeV. It has been observed that all the photon interaction parametersfor the selected glass systems vary with the photon energy.

Keywords

Glasses, Gamma Rays, Photon Interaction Parameters.

I. Introduction

Phosphate glasses have a wide range of applications owing to its properties such as low melting temperature, low optical dispersion, high thermal expansion coefficient [1-2], high refractive indices and high transparency to UV light as compared to silicate glasses [3]. Phosphate glasses are found to be advantageous over silica glasses for being good host

to high concentration of doping rare earth ions for solid state lasers [4]. Zinc phosphate glasses could potentially be used for the treatment of chronic inflammatory diseases such as rheumatoid arthritis, which is characterised by decreased Zn^{2+} levels in the blood. Alexander et al. [5] first developed phosphate glasses having high capacity for absorption of short electromagnetic waves (X-rays and gamma rays). Hood and MacAvoy [6] developed a transparent high density phosphate glasses particularly suitable for radiation shielding windows. Arbuzov et al. [2] studied optical, spectral and radiation shielding properties of high lead phosphate glasses and reported the glass samples to be resistant to radiation at doses up to 107R. The authors also reported larger coefficient of absorption of gamma radiations for the said glass samples than those of dense silicate flints. Lead-indium and lead-scandium phosphate glass systems are found to have low melt viscosity, better chemical durability, high refractive index (1.75 to 1.83) in visible region, better transparency and moderate dispersion which makes them potentially useful for radiation shielding applications [7].

Materials to be used for radiation shielding should have homogeneity of density and composition, and sufficient thickness to absorb the radiations to a safe level. Mass attenuation coefficient (μ_m), mean free path (mfp), effective atomic number (Z_{eff}), half value layer (HVL) and the electron density (Ne) are the basic quantities which determine the scattering and absorption of X-rays and gamma rays photons in matter.

The mean free path (mfp) measures the average distance travelled by a photon between two consecutive collisions/scatterings in the material. Half value layer (HVL) is the thickness of the interacting material at which the intensity of the photon beam entering it is reduced by one half. The lower are the values of mfp and HVL, the better is the radiation shielding material in terms of thickness requirement. The effective atomic number for a material composed of several elements cannot be expressed by a single number. It has to be weighed differently for each of the different processes by which gamma rays can interact with matter [8]. The effective atomic number is defined as the ratio of total atomic cross-section to the total electronic cross-section.

The main objective of this study is to investigate (a) mass attenuation

coefficient, effective atomic number, half value layer, mean free path and electron density of four samples of 15 ZnO - (17.5 - x) Al_2O_3 - x Fe_2O_3 - 67.5 P_2O_5 glass systems (x = 0, 7.5, 12.5, 17.5) and two samples of 15 ZnO - (25 - x) Al_2O_3 - x Fe_2O_3 - 60 P_2O_5 glass systems (x = 0, 25) for photon energies of 1 keV to 100 GeV and (b) to compare the photon interaction parameters of the selected glass samples.

II. Computational Work

The chemical composition and density of the selected glass samples [1] have been given in Table 1.

Table 1. *Chemical compositions and density of selected glass samples*

Sample	Chemical Composition (mol %)				Glass density (g/cm^3)
	ZnO	Al_2O_3	Fe_2O_3	P_2O_5	
ZAP1	15	17.5	0	67.5	2.68
ZAFP2	15	10	7.5	67.5	2.79
ZAFP1	15	5	12.5	67.5	2.81
ZFP1	15	0	17.5	67.5	3.39
ZFP2	15	0	25	60	3.14
ZAP2	15	25	0	60	2.63

A. Mass attenuation Coefficient:

Mass attenuation coefficients (μ_m) measures the number of photons interacted (may be scattered or absorbed) with the interacting material [9]. values of the selected glass samples were generated in the energy region from 1 keV to 100 GeV using Win X Com energy grid [10] based on the mixture rule (equation 1) [11]. The program provides total cross section and attenuation coefficients as well as partial cross sections for various interaction processes for about 100 elements.

$$\mu_m = \frac{\mu}{\rho} = \sum_i w_i \left(\frac{\mu_i}{\rho_i}\right) \qquad (cm^2/g) \qquad (1)$$

where μ_i, ρ_i and W_i are the attenuation coefficient, density and weight fraction of the i^{th} constituent element respectively.

B. Mean Free Path:

The mean free path has been determined from the attenuation coefficient using the relation

$$mfp = \frac{1}{\mu} \text{ (cm)} \quad \ldots (2)$$

where μ is the linear attenuation coefficient of the selected glass samples which is obtained by multiplying the corresponding values of mass attenuation coefficients with its densities.

C. Half Value Layer:

Half value layer has been computed using the relation

$$HVL = \frac{0.693}{\mu} \quad \text{(cm)} \quad \ldots (3)$$

D. Effective Atomic Number:

The molecular cross-section has been calculated by the relation [12-13]

$$\sigma_m = (\mu_m)_{glass} \frac{M}{N_A} \text{ (barn/molecule)} \quad \ldots (4)$$

where $M = \sum_i n_i A_i$ is the molar mass, N_A is Avogadro number, n_i and A_i are the number of formula units and the atomic weight, respectively, of the i^{th} element in the glass system.

The average atomic cross-section can be obtained by dividing the molecular cross-section by the total number of formula units as follow:

$$\sigma_a = \sigma_m \frac{1}{\sum_i n_i} \text{ (barn/atom)} \quad \ldots (5)$$

The average electronic cross-section would be calculated by the relation [14]

$$\sigma_e = \frac{1}{N_A} \sum_i \frac{f_i A_i}{Z_i} (\mu_m)_{glass} \quad \text{(barn/electron)} \quad \ldots (6)$$

where $f_i = \frac{n_i}{\sum_j n_j}$ is the fractional abundance of element w.r.t. total number of atoms.

The effective atomic number has been calculated by the relation [15]

$$Z_{eff} = \frac{\sigma_a}{\sigma_e} \text{ (unit-less)} \quad \ldots \quad (7)$$

E. Electron Density:

The electron density N_e can be derived from mass attenuation coefficient and electronic cross-section values using the following expression [16]:

$$N_e = \frac{\mu_m}{\sigma_e} \quad \text{(e/g)} \quad \ldots(8)$$

III. Result And Discussion

Mass attenuation coefficients (μ_m) for the selectedZnO-Al_2O_3-Fe_2O_3-P_2O_5 glass systemsso obtained using WinXCom software for photon energies ranging from 1 keV to 100 GeV has been shown in Fig. 1. The mass attenuation coefficient of the selected glasses varies with the photon energy for all the compositionsfor total interaction processes. The variation in μ_m for the selected glass systems with energy can be divided into three parts on the basis of three dominant photon interaction processes in different energy regions (i) photoelectric absorption from 1 to 100 keV, (ii) Compton scattering from 100keV to 11 MeV and (iii) pair production at energy above 11 MeV. Coherent scattering is not playing any significant role here because it occurs mainly at very low energies.

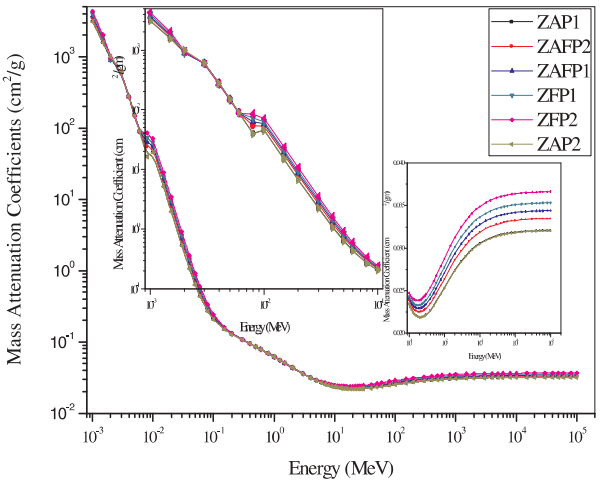

Fig 1: Variation of mass attenuation coefficient with the energy of gamma radiations

Below 10 keV, there has been observed discontinuities in the variation of μ_m which arises from the photoelectric effect around various absorption edges of elements. Aluminium has a K absorption edge at 1.56 X 10^{-3} MeV.

Iron has K- absorption edge at 7.112 X 10^{-3} MeV. K- absorption edge of phosphorous lies at 2.145 X 10-3 MeV. L_1, L_2 and L_3 absorption edged of zinc are at 1.194 X 10^{-3}, 1.043 X 10^{-3} and 1.020 X 10^{-3} MeV respectively. K-absorption edge of zinc lies at 9.659 X 10^{-3} MeV.

Effective atomic number (Z_{eff}) is computed for selected glass samples from the contribution of all partial photon interaction processes in different energy regions. Its variation with energy has been shown in Fig. 2. Below 10 keV, there has been observed a discontinuous decrease in Z_{eff}. This may be due to absorption edges of various constituent elements. From 10 to 200 keV, there has been a sharp decrease in Z_{eff} due to dominance of photoelectric absorption in this region. Z_{eff} becomes constant from 100keV to 2MeV due to Compton scattering. Thereafter, Z_{eff} increases with increase

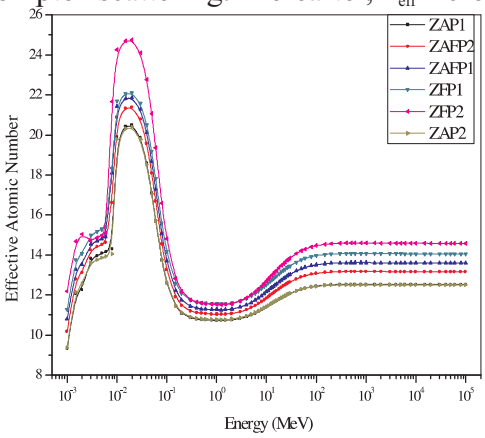

Fig 2: Variation of Effective Atomic Number with the energy of gamma radiations

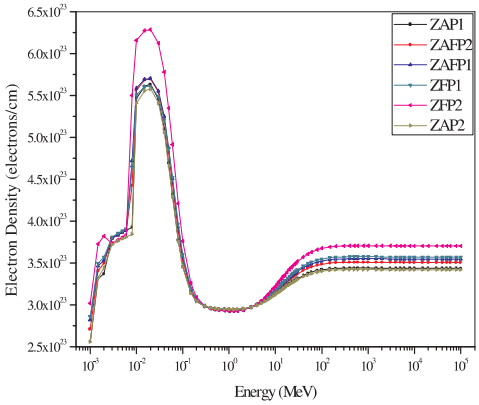

Fig 3: Variation of electron density with the energy of gamma radiations

in photon energy above 5 MeV due to dominance of pair production in the higher energy region. The glass sample ZFP2 is shown to have the maximum value of Z_{eff} at almost all the energies in the given energy range. It is observed that the variation of μm and Z_{eff} is increased with increasing weight fraction of Fe_2O_3. Variation of electron density (N_e) with energy is following the same trend as that by Z_{eff} (Fig.3).

The variation of mean free path and half value layer has been shown in Fig. 4 and 5. The variation of mfp and HVL has higher value around 30 MeV where Compton scattering is predominant.

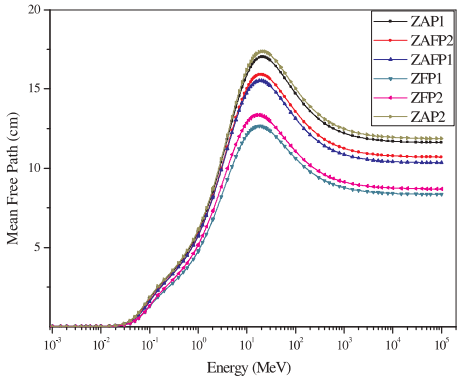

Fig 4: Variation of mean free path with the energy of gamma radiations

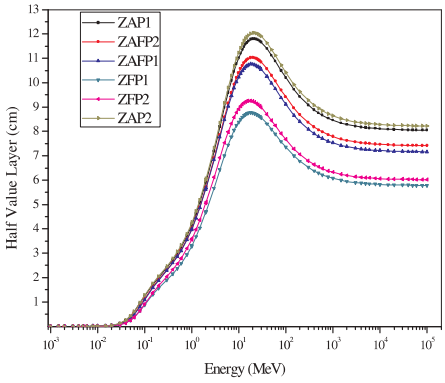

Fig 5: Variation of half value layer with the energy of gamma radiations

Among all the selected samples, ZFP2 shows the lowest values of mfp and HVL for all energy regions in the given energy range. This is due to the higher values of mass attenuation coefficients and densities for selected glass samples.

Among the selected glass samples, ZFP2 sample is shown to have the best radiation shielding parameters in terms of mass attenuation coefficient and effective atomic number. Moreover, ZAP1 and ZAP2 samples are shown to have least value of effective atomic number, maximum value of mean free path and half value layer. It may be due to the presence of Fe_2O_3.

IV. Conclusion

Present investigations among the selected glass samples shows that the sample ZFP2 (with maximum contribution of Fe_2O_3 with ZnO) has maximum value of mass attenuation coefficient and effective atomic number, and minimum values for mean free path and half value layer. Hence, it can be better used for shielding purposes.

Among the selected glass samples, ZAP2 has the least value of mass attenuation coefficient, effective atomic number and electron density, and maximum values for mean free path and half value layer for the selected energy range. Hence, it can be used for making geometries to hold samples.

V. References

[1] M. Karabulut, E.Melnik, R. Stefan, G.K. Marasinghe, C.S. Ray, C.R.Kurkjian, D.E. Day, "Mechanical and structural properties of phosphate glasses" J. Non-Crys. Solids 288(2001) 8-17.

[2] V. I. Arbuzov, N. Z. Andreeva, N. A. Leko, S. I. Nikitina, N. F. Orlov, and Y. K. Fedorov"Optical, spectral, and radiation-shielding properties of high-lead phosphate glasses" Glass Phys. and Chem.31 (2005) 583590.

[3] R. K. Brow, "Review: The structure of Simple Phosphate Glasses" J. Non-Crst. Solids 263 (2000) 1 - 28.

[4] M. Bitar, J.C. Knowles, M.P. Lewis,V.Salih"Soluble phosphate glass fibres for repair of bone-ligament interface" J. Mat. Sci. 16(2005) 1131-1136.

[5] S. Alexander, P. Pittsburgh, J. Joseph Rothermel, N. Y. Corning, and-Kuan-Han Sun, P. Wilkinsburg "Phosphate glass" US Patent 2 518 194, 1950.

[6] H.P. Hood and T.C. MacAvoy"High density, soft phosphate glass, method, and gamma radiation shielding window" US Patent 3 149 234, 1964.

[7] B.C. Sales and L.A. Boatner, "Optical, structural and chemical characteristics of Lead-Indium Phosphate and Lead-Scandium Phosphate glasses"J. American Ceramic Society 70(1987) 615-621.

[8] G.J. Hine "The effective atomic numbers of materials for various gamma interactions" Phys. Rev. 85(1952) 725-737.

[9] T. Singh, P. Kaur, P. S. Singh "Variation of mass attenuation Coefficient, Effective atomic number and electron density with incident photon energy of some organic acids"Nucl. Sci. Engg. 156(2007) 1-15.

[10] L. Gerward, N. Guilbert, K. B. Jensen, H. Levring "X-ray absorption in matter: Reengineering XCOM" Radiat. Phys. Chem. 60(2001) 23-24.

[11] D.F. Jackson, D. J. Hawkes, "X-ray attenuation coefficients of elements and mixtures" Phys. Rep. 70(1981) 169-233.

[12] H. Singh, K. Singh, L. Gerward, K. Singh, H.S. Sahota, R. Nathuram, "ZnO-PbO-B_2O_3 glasses as gamma-ray shielding materials" Nucl. Instrum. Methods B 207(2003) 257-262.

[13] K. Singh, H. Singh, V. Sharma, R. Nathuram, A, Khanna, R. Kumar, S. S. Bhatti, H. S. Sahota, "Gamma ray attenuation coefficients in bismuth borate glasses" Nucl. Instrum. Methods B 194(2002)1-6.

[14] T. Singh, Rajni, U. Kaur, P. S. Singh, "Photon energy absorption parameters for some polymers" Ann. Nucl. Energy 37(2010) 422-427.

[15] K. Singh, H. Singh, G. Sharma, L. Gerward, A. Khanna, R. Kumar, R. Nathuram, H. S. Sahota, "Gamma-ray shielding properties of CaO-SrO-B_2O_3 glasses" Radiat. Phys. Chem. 72(2005)225-228.

[16] S. R. Manohara, S.M. Hanagodimath, L. Gerward, "Photon interaction and energy absorption in glass: a transparent gamma ray shield" J. Nucl. Mater. 393(2009) 465-472.

Curr. Rep. Sci. & Tech. 1 (2) (2015) 38-45

Correlation Among The Structural, Morphological And Gas Sensing Parameters Of USP Deposited Al-CuO Films

Iqbal Singh, Taminder Singh and Gursharan Kaur
Department of Physics, Khalsa College, Amritsar (India)
iqbalsgh@yahoo.com

Abstract

Nanocrystalline Al doped CuO films have been deposited on to the corning glass substrate by ultrasonic spray pyrolysis (USP) technique. The effect of doping concentration 1, 5 and 10 % of Al on the film properties was investigated. The films were deposited at substrate temperature of 300 °C using aqueous a cupric nitrate solution as host and aluminium nitrate solution as dopant in precursor solution. The effect of doping on the structural, morphological, and gas sensing properties of CuO films was studied and correlated. X-ray diffractograms of the films indicate the formation of polycrystalline CuO having monoclinic crystal structure with crystallite size around 18 nm. No phase corresponding to the aluminium or its oxide has been detected on the XRD diffractogram. The scanning electron micrographs indicate the formation of trapezium like facet structures on the film surface.

Keywords

CuO, Spray pyrolysis, Activation energy, Gas sensor

I. Introduction

Doping is a traditional technology used in metal oxide based materials by which material properties can be substantially improved by dispersing a low concentration of additives on surface or in its volume. The doping affects the material properties in different ways such as enhancement in catalytic activity and modifies structural parameters of the intrinsic metal oxide [1-3]. Metal oxide nanostructures have been doped by many physical or chemical methods, such as thermal evaporation [4], wet chemical methods [5], spin coating [6] and sputter deposition [7].

In the proposed work an attempt has been made to dope aluminium (Al) ions in CuO material to check its effect on the material properties. The ultrasonic spray pyrolysis is an excellent technique for preparing uniformly

doped nanostructured CuO. The incorporation of Al^{3+} ions destroys CuO crystallinity by efficiently substituting Cu^{2+} sites in the material since the radius of Al^{3+} ion (0.53 Å) is smaller than that of Cu^{2+} ion (0.73 Å). The defect equation of Al^{3+} substituted Cu^{2+} ions can be represented by an equation 1. The substitution of Al^{3+} ions for Cu^{2+} ions will consume some native holes. Thus for p-type semiconductor, the decreased hole concentration decreases the electrical resistivity.

$$Al_2O_3 + 2h^0 \Rightarrow 2Al^0 \quad + 2O_o^{\ x} + \frac{1}{2}O_2 \tag{1}$$

II. Experimental

A. Film Deposition

The films of CuO were deposited onto glass substrate using 0.2M aqueous solution of trihydrated cupric nitrate ($Cu(NO_3)_2.3H_2O$) with controlled volume of aqueous solution of $Al(NO_3)_3.9H_2O$ to have doping concentration of 1, 5 and 10% . To make 100 mL of the precursor solution the required quantity of salt is dissolved in double distilled water. Before deposition, the substrates were, firstly cleaned and deposition parameters are optimized described in detail [8]. The substrate temperature was selected as 300 ˚C on the basis of reports [9].

a. Structural Analysis

The phase identification of the film was analyzed by X-ray diffraction (XRD) pattern, taken using X'Pert Panlytical diffractometer with Cu K_α radiation (λ = 1.5405 Å , 30mA , 40 KV) in 2θ range from 30-80˚. The crystallite size in CuO samples has been calculated using Scherrer's formula as given below [10].

$$D = \frac{K\lambda}{B\cos\theta_B} \tag{2}$$

b. Lattice constants

Lattice parameters ($a \neq b \neq c$, $\alpha = \gamma = 90^\circ \neq \beta$ for monoclinic structure) and the volume of unit cell for the CuO films were calculated using the formulas given below

$$\frac{1}{d^2} = \frac{1}{\sin^2\beta}\left(\frac{h^2}{a^2} + \frac{k^2\sin^2\beta}{b^2} + \frac{l^2}{c^2} - \frac{2hl\cos\beta}{ac}\right)$$
$$V = abc\sin\beta \tag{3}$$

B. Surface Morphology And Compositional Study

To study the surface topography and compositional analysis of films, field emission scanning electron micrographs (FESEM), energy-dispersive absorption X-ray spectroscopy (EDAX) spectrum respectively were taken on a JEOL JSM-6700F with a beam voltage of 30 KV. The thickness of the film was monitored using depth profiler (Dektek 3030 XT).

C. Electrical Characterization

The electrical characterization of the film was done by using two probe technique by heating the sample with the help of a specially designed heater and the temperature measured using a K-type (chromelalumel) thermocouple placed on the middle of the substrate.

D. Activation energy

The change in conductivity of the films was measured in the temperature range 300 to 473 K, by applying a d.c. 10 V bias across the films with silver contact. The data so obtained has been used to calculate the activation energy using the formula.

$$\sigma = \sigma_0 \exp(-\frac{\Delta E_a}{kT}) \quad (4)$$

where ΔE_a is the activation energy which corresponds to the energy difference between the valance band and the conduction band, σ_o is a temperature independent factor and k is the Boltzman's constant and T is the absolute temperature.

b. Gas response

The films were tested for their room temperature sensitivity to ammonia with the help of gas sensing set up and the data was recorded with Keithley (6517A) electrometer when 50 ppm of ammonia gas was introduced in the measuring cell of volume 500 cm^3. The response (S) of a sensor is defined as the ratio of change in the resistance on exposure to gas to the resistance in air.

$$S = \frac{|R_g - R_a|}{R_a}$$

where R_g and R_a are CuO thick film resistance, measured in ammonia and air atmosphere, respectively.

III. Results and discussion

Fig 1. shows the Al doped CuO films deposited onto the glass substrate kept at temperature of 300˚C with deposition time of 10 minutes. The obtained XRD diffractogram of the film are shows sharp peaks indicating polycrystalline nature of samples and shows the characteristic peaks corresponding to CuO phase. It has been observed in the diffractogram that no peak corresponding to the Al or Al_2O_3 phase appeared on the XRD pattern of all samples with different dopant amount. A matching of the observed and the standard (*hkl*) planes confirms that the deposited films are polycrystalline having monoclinic CuO. The diffractogram show the prominent (002) and (111) monoclinic CuO peaks and the prominent peak positions along with *d* values are tabulated in Table 1. The positions and the *d* values of the diffraction peaks for CuO are in good agreement with those reported earlier for the spray deposited CuO thin films [11, 12]. The change in intensity of prominent peaks or the disappearance of small intensity peaks with doping concentration in the films may be due to the difference in growth behaviour e.g. orientation of crystallites, phase composition etc.

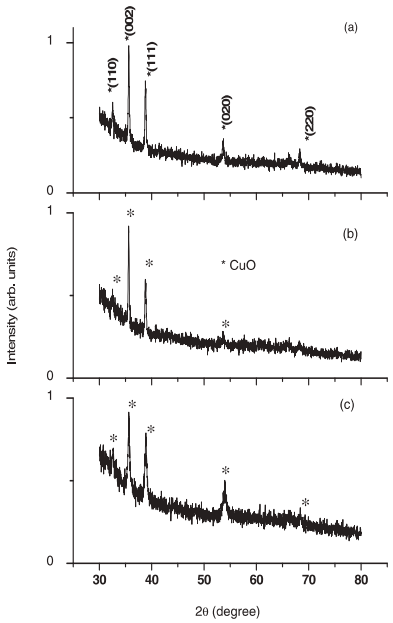

Fig 1. XRD diffractograms of Al doped CuO thin films of (a) AF1, (b) AF2 and (c) AF3 samples

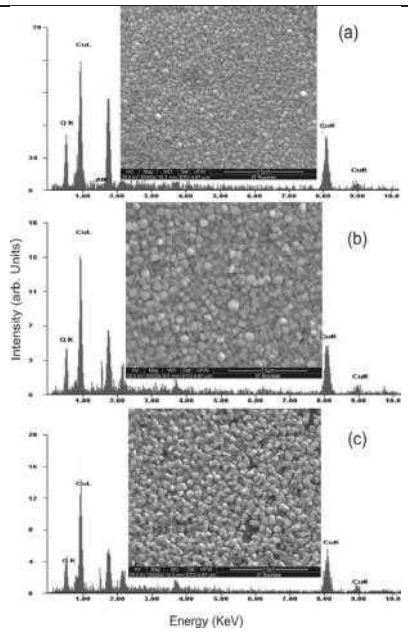

Fig 2. FESEM images and EDAX spectrums of Al doped CuO films of (a) AF1, (b) AF2 and (c) AF3 samples

Table 1 *Sample code, prominent peak positions (2θ), interplannar spacing (d) and relative intensity (I) of diffraction peaks of Al doped CuO thin film samples*

Al doped CuO thin film sample	Sample name	2θ(°)	d(Å)	I
1% doping	AF1	35.633	2.517	100
		38.794	2.319	76.33
5% doping	AF2	35.618	2.518	100
		38.774	2.321	66
10% doping	AF3	35.650	2.516	100
		38.888	2.314	86.73

Table 2 *Lattice parameters, strain, crystallite size, elemental composition, activation energy and optical band gap of Al doped CuO thin film samples*

Property/sample	AF1	AF2	AF3
a (Å)	4.695	4.672	4.724
b (Å)	3.429	3.427	3.411
c (Å)	5.125	5.115	5.129
β (Degree)	99.406	99.152	99.676
cell volume (Å^3)	81.413	80.877	81.503
Average Crystallite size, D (nm) XRD	38	35	36
Cu:O, atomic % age	59.11:40.89	52.54: 47.46	52.43:47.57
Activation energy E_a (eV)	0.22	0.23	0.26

The average crystallite size in Al doped CuO samples has been calculated from the prominent peak position using Scherrer's formula and obtained values (Table 2) have been found to lie in range of 35-38 nm. The observations indicate that addition of higher aluminum ions during the deposition of CuO films show comparatively smaller crystallite size. The lattice parameters of Al-CuO samples have been calculated and obtained values (Table 2) are in good agreement with those contained in ICDD card 41-254.

Fig 2 shows FESEM images and corresponding EDAX spectrum of aluminium doped film samples. The images show uniform distribution of faceted like spherically shaped grains in all samples. It has been observed from the images that the size of grains goes on increasing with the dopant concentration. The EDAX spectrum gives elemental composition of Cu and O atoms and samples are found to be metal deficient. EDAX analysis shows Al content of approximately same to doped value in all samples.

The electrical measurement of Al doped CuO film samples have been investigated as function of temperature (300-473 K). The conductivity of

films is found to increase with increase in temperature due to chemisorptions of large number of oxygen molecules on surface of film. Fig 3. shows the temperature dependence of conductivity of films and slope of lnσ vs. 1000/T plots has been used to calculate activation of the aluminium doped CuO film samples The activation energies (E_a) (Table 2) found to lie in range of 0.22 to 0.26 eV for all doped CuO samples. The value of activation energy is found to increase with dopant concentration. The variation of activation energy with doping can be understood from the change in crystallite size and inclusion of defects which affects the scattering of carriers at grain boundaries and mobility.

The gas response characteristics of USP deposited Al-CuO thin films are shown in Fig 4. Observations show that resistance of films starts decreasing with the introduction of ammonia gas and attains a saturate value after some time. The AF2 and AF3 films exhibits highest response in rage of 95-96 % with shortest response time of 60 seconds. Whereas, AF1 film show comparatively poor response of 72% only. The effect of dopant on gas sensing properties of films can be explained on the basis of modification induced by dopant in terms of increasing catalytic sites for gas adsorption [13]. Aluminium doped USP deposited CuO films show poor recovery of film resistance but AF2 and AF3 films recovers the 90% of the resistance in 500 seconds whereas AF3 films do not recover the resistance in same time.

IV. Conclusions

Nanocrystalline Al doped CuO thin films have been successfully deposited onto the amorphous glass substrates at substrate temperature of 300˚C with required deposition time of 10 minutes by low-cost aerosol spray pyrolysis technique. The structural and surface morphological characterization studies of the films shows that doping in the film induce defects which enhances the catalytic activity of the film surface. The sensitivity of the 10% Al doped sample is found to be highest among the investigated samples for ammonia vapors at room temperature.

V. Acknowledgements

The authors thank Director Indian Institute of Technology Roorkee

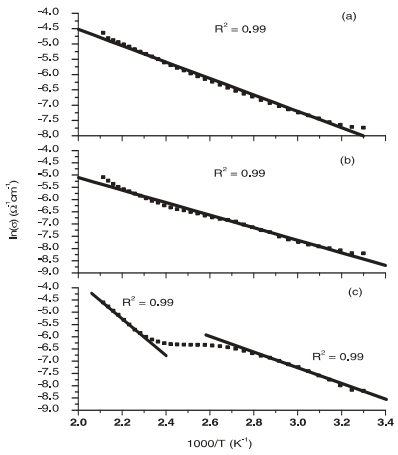

Fig 3. Electrical conductivity as a function of temperature of Al doped CuO films of (a) AF1, (b) AF2 and (c) AF3 samples

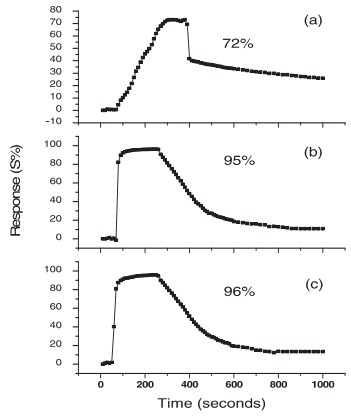

Fig 4. Room temperature ammonia response of Al doped CuO films of (a) AF1, (b) AF2 and (c) AF3 samples

and Central Instrumentation Laboratory, Panjab University, Chandigarh for providing FESEM, EDAX and XRD facilities.

VI. References

[1] K. Jain,, R. P. Pant, and S. T. Lakshmikumar, Effect of Ni doping on thick film SnO_2 gas sensor Sensors and Actuators B 113(2006) 823-829.

[2] G. Korotcenkov. Gas response control through structural and chemical modification of metal oxide films: State of the art and approaches. Sensors and Actuators B 107(2005) 209-232.

[3] I. T. Weber,, A. Valentini, L. F. D. Probst, E. Longo, and E. R. Leite, Influence of noble metals on the structural and catalytic properties of Ce-doped SnO_2 systems. Sensors and Actuators B 97(2004) 31-38.

[4] V. Kumar, S. Sen, K. P. Muthe, N. K. Gaur, S. K. Gupta and J. V. Yakhmi, Copper doped SnO_2 nanowires as highly sensitive H_2S gas sensor. Sensors and Actuators B 138 (2009) 587-590.

[5] L. F. He, Y. Jia, F. L Meng, M. Q. Li and J. H. Liu, Development of sensors based on CuO-doped SnO_2 hollow spheres for ppb level H_2S gas sensing. Journal of Material Science 44 (2009)4326-4333.

[6] J. Kaur, R. Kumar and M. C. Bhatnagar, Effect of indium-doped SnO_2 nanoparticles on NO_2 gas sensing properties. Sensors and Actuators B 126 (2007)478-484.

[7] A. Salehi, Selectivity enhancement of indium-doped SnO_2 gas sensors. Thin Solid Films, 416 (2002) 260-263.

[8] I. Singh and R. K. Bedi, Studies and correlation among the structural, electrical and gas response properties of aerosol spray deposited self assembled nanocrystalline CuO. Applied Surface Science 257(2011)7592-7599.

[9] I. Singh, G. Kaur and R. K. Bedi, CTAB assisted growth and characterization of nanocrystalline CuO films by ultrasonic spray pyrolysis technique. Applied Surface Science 257(2011)9546 9554.

[10] H. P. Klug and L. E. Alexander,. X-ray diffraction procedure for polycrystalline and amorphous materials. 2nd edition Wiley, New York(1974) 687.

[11] S. Kose, F.Atay, V. Bilgin and I. Akyuz, Some physical properties of copper oxide films: the effect of substrate temperature, Mater. Chem. Phys. 111(2009) 351-358.

[12] J. Morales, l. Sanchez, F. Martin, J. R. Ramos-Barrado and M. Sanchez, Nanostructured CuO thin film electrodes prepared by spray pyrolysis: a simple method for enhancing the electrochemical performance of CuO in lithium cells, Electro. Acta 49 (2004) 4589-4597.

[13] I. Singh, T. Singh and G. Kaur, Impact of surfactant and co-surfactant on the structural, morphological and electrical properties of nanocrytalline Copper oxide, Current Reports in Sci. And Technol. 1(1) (2015)18-26

Curr. Rep. Sci. & Tech. 1 (2) (2015) 46-51

Structural, Magnetic and Optical Properties of Cobalt Doped Zinc Oxide

Anumeet Kaur, Veerpal Kaur, Vandana, Anupinder Singh, Mandeep Singh and Lakhwant Singh
Department of Physics, Guru Nanak Dev University, Amritsar (India)
anupinders@gmail.com

Abstract

The proper phase formation of powder samples of pure zinc oxide (ZnO) and cobalt doped ZnO, synthesized by sol- gel method was confirmed X-ray diffraction. To see the proper grain growth SEM micrographs were taken and the presence of all the elements in the samples was confirmed with EDAX. The ferromagnetic behavior, the presence of new vibrational bands with Co doping was confirmed by Magnetic measurements and Raman Spectroscopy respectively.

Keywords

Sol- Gel Method, XRD, SEM, .Magnetic Properties

I. Introduction

Zinc oxide has gained a lot of attention of scientific community in past few decades. Being nontoxic, inexpensive and chemically stable, it has useful optical, chemical and electrical properties. Zinc oxide has wide direct band gap (eg=3.3eV), high excitation binding energy (60MeV) and room temperature thermal energy of 25 MeV. Because of these novel features it is mainly used in the fabrication of optoelectronic devices operating in the blue and ultraviolet (UV) regions and has gas sensing applications also [1-2]. It has a wide range of technological applications such as in transparent conducting electrodes of solar cells, flat panel displays, surface acoustic devices, chemical and biological sensors and UV Lasers.

ZnO is a semiconductor and the combination of magnetic properties in semiconductor is also a promising field having applications in LED, Lasers and spintronics. The optoelectronic properties get enhanced with doping of transition metal and give the room temperature paramagnetism and high temperature ferromagnetism and are known as dilute magnetic

semiconductors [2,3]. In this paper, we have doped cobalt in ZnO by simple and inexpensive sol- gel method, having easier composition control and needs lower processing temperature. The Raman spectroscopy, structural and magnetic properties of cobalt doped ZnO have been reported.

II. Experimental

Cobalt doped zinc oxide powders with composition $Zn_{(1-x)}Co_xO$ with x=0, 0.2 (abbreviated as ZNO and ZNCO) were prepared by sol-gel method[4]. Cobalt nitrate (99.5% purity Loba Chemie) and zinc acetate (99% purity Loba Chemie) were used as precursors for cobalt and zinc respectively. First the molar solution of ZnO was prepared by mixing them together and the desired solution was stirred for 30 minutes. Afterwards 20ml ethanol and 5ml diethnalamine was added drop wise to the solution. With the addition, solution became milky and precipitates were formed. To obtain the Gel, the solution was again stirred for 5 hours at 800°C. After the gel formation sample was heated for 12 hours at 500°C. The sample was then grinded to obtain the fine powder. The pellets of this powder were made by adding 2% polyvinyl alcohol (PVA) by weight. Pressing of PVA mixed powder in the form of pellets was done using 10mm dye by applying pressure 10 MPa. The pellets were then sintered at 800°C for 4 hours for proper grain growth and densification.

The prepared samples were then characterized using various techniques. Structural Characterization was carried out using Room temperature X-Ray Diffraction (CuKα radiation, SHIMADZU MAXimaXRD-7000), Scanning Electron Microscope (FESEM) (Carl ZEISS Supra 55) and Energy dispersive X Ray analysis (EDAX) (OXFORD instruments attached with FESEM). The magnetic properties were studied by using Vibrating Sample Magnetometer (VSM) (MicroSense). Raman Spectroscopy was studied with RENISHAW in Via Raman microscope.

III. Results and Discussions

A. Structural Properties:- The phase formation, microstructure and elemental composition studied for Pure ZnO and cobalt doped ZnO samples is discussed in the following sections.

(1) *Phase Formation:-* X-Ray Diffractogram taken at room temperature showing sharp peaks revealed the polycrystalline phase formation. Fig. 1. shows the XRD pattern taken for ZNO and ZNCO corresponding to composition $Zn_{(1-x)}Co_xO$ with x=0, 0.2. The peaks indexed to (100), (002), (101), (102), (110), (103), (200), (112),(201) (004) and (202) correspond to wurtzite ZnO, matching JCPDS card no-5-0664 [4]. The peak indexed as (*) is the impurity peak. An obvious shift in peaks is also observed with doping of Co in ZnO which can be attributed to change in ionic radius.

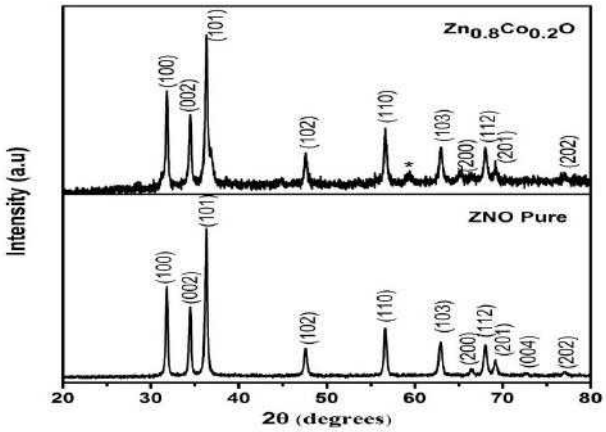

Fig. 1. X-Ray Diffractogram of ZNO and ZNCO.

(2) *Microstructure:* -The SEM micrographs of sintered pellets were taken at same magnification of 15KX to study the surface morphology The SEM images of Sintered samples are shown in Fig. 2

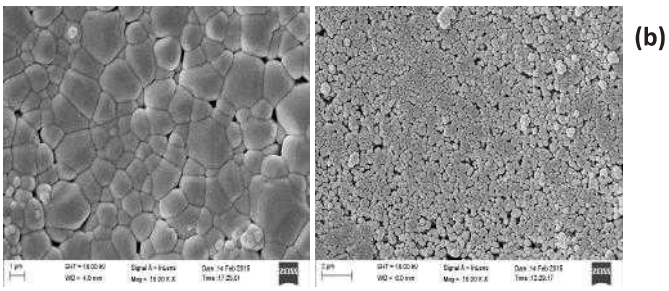

Fig. 2. FESEM images of sintered samples (a) ZNO (b) ZNCO

The images clearly show grain growth in all the samples. With cobalt doping in ZnO the grain size appears to be smaller than pure ZnO.

Table 1. *The weight % of samples (a) ZNO (b) ZNCO*

Sample	%Zn	%O	%Co
ZNO	32.55	5.62	-
ZNCO	40.91	1.95	8.83

(3) ***Composition:*** - The Energy Dispersive X- Ray Spectra confirmed the presence of main elements (Zn, O) and doped element (Co) The EDAX spectra of both the samples is shown in Fig**.** 3 and weight% of all elements is shown in Table1.

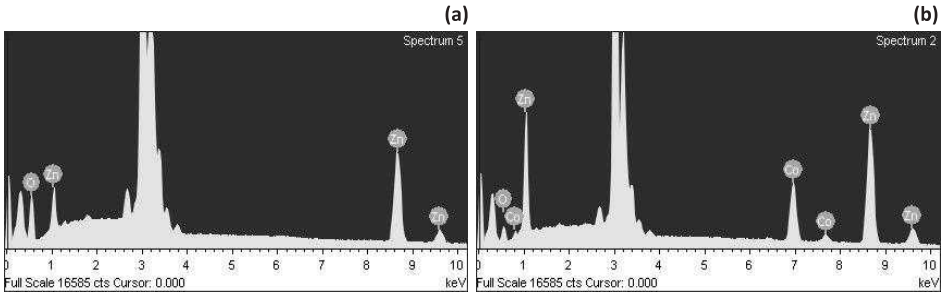

Fig.3. EDAX spectra of (a) ZNO (b) ZNCO

B. Magnetic Properties:- Pure ZnO is diamagnetic in nature but with the doping of magnetic ion (Cobalt) in ZnO, a feeble ferromagnetic nature is observed at room temperature; shown in fig. 4.

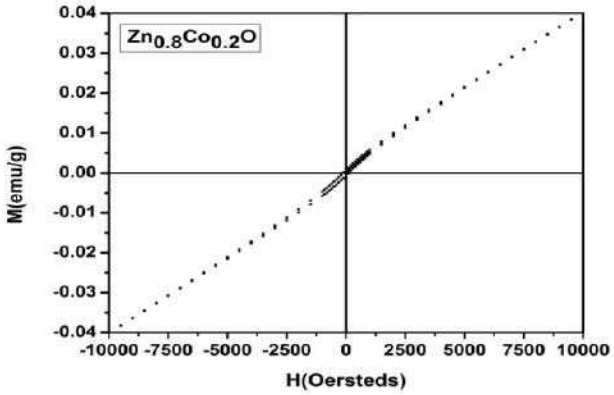

Fig. 4. Magnetization versus magnetic Field for ZNCO at room temperature

The values of coercive field and Remnant magnetization are 115.114 Oe and 72.452E-6 emu/g respectively.

C. Raman Spectroscopy:- The vibrational bands of ZnO and cobalt doped ZnO ($Zn_{(1-x)}$ Co_x O where x=0.2) were investigated by Raman spectroscopy. The argon (Ar^+) laser of wavelength 514.5 nm was used for this analysis. The Raman spectra obtained are shown in Fig. 5. The optical modes predicted by group theory are A1+2B1+E1+2E2 at G point of brillouin zone, where A1, E1 and E2 are first order Raman active modes and B1 is forbidden.

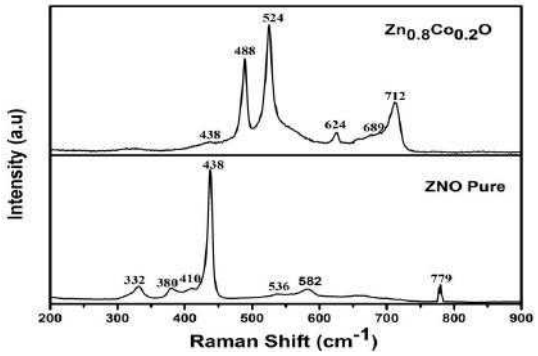

Fig. 5. Raman spectra of (a) ZNO (b) ZNCO

For pure ZnO powder there are two peaks at 332 and 438 cm^{-1} which are ascribed to multiple-phonon scattering process and E2 (HIGH) mode respectively. In addition to this five more normal modes were obtained at 380, 410, 536, 582 and 779^{cm-1} corresponding to A1(TO), E1(TO), E1(LO), E2(HIGH)+E2(LOW), E1(LO) respectively [5].For cobalt doped ZnO ($Zn_{1-x}Co_xO$) there are two strong vibrational bands at 488 and 524^{cm-1}. However the bands at 438 cm-1 appear as less intense as compared to pure ZnO sample which is present at same wavenumber. Including this there are also five more bands similar to pure ZnO sample, these bands are at 488, 524 and 624 cm^{-1} corresponding to A1 (TO)+ E2 (LOW) (surface interface) phonon mode, 2B1(HIGH), TA+B1 (LOW) respectively. The vibrational band at 699 cm-1 may be due to cobalt oxygen vacancy-cobalt complexes and 712 cm^{-1} may be due to local vibration of sub situational Co [6].

IV. Conclusions

The structural analysis using XRD and SEM revealed proper phase

formation and proper grain growth respectively in both $Zn_{(1-x)}CoxO$ with x=0, 0.2 samples prepared by sol-gel method. EDAX confirmed the stoichiometry of all the samples. VSM measurements with cobalt doping confirmed the ferromagnetic behavior while Raman spectra showed the presence of new vibrational bands.

V. Acknowledgement

Authors are very grateful to GNDU (University Potential For Excellence), Amritsar for providing various research facilities to accomplish this research work. One of the authors Anumeet Kaur would like to thank UGC India for providing fellowship.

VI. References

[1] N. H. Nickel and E. Terukov, Zinc oxide-A material for micro- and optoelectronic applications (Springer, Dordrecht, 2005).

[2] J.B.Cui and U.J.Gibson, Electrodeposition and room temperature ferromagnetic anisotropy of Co and Ni-doped ZnO nanowirearrays, Appl.Phys.Lett.87(2005) 133108-1-133108-3

[3] N.F.Djaja, D.A,Montja and R.Saleh,The effect of Co incrporation into ZnO nanoparticles, Adv.Mater. Phys. Chem. .3 (2013)33-41.

[4] Z. N. Kayani, A.A.FSaleemi, S.Riaz and S.Naseem, Structual, optical and magnetic properties of cobalt-doped dip coated ZnO films;IEEE Transactions on magnetics, 50 (2014) No.8,

[5] W. Zhang, J.Zhao, Z. Liu, Z. Liu, Structural, optical and magnetic properties of Zn1-xFexO powders by sol-gel method, Applied Surface Science 284(2013) 49-52

[6] Q.Cao, S. He, Y.Deng, D. Zhu, X. Cui, G.Liu, H. Zhang, S. Yan, Y.Chen, L. Mei, Raman scattreing investigations on Co- doped ZnO epitaxial films: local vibration modes and defrct associated ferromagnetism, Current applied physics 14 (2014) 744-748

Curr. Rep. Sci. & Tech. 1 (2) (2015) 52-61

A study of indoor radon, thoron and their progeny concentration in Rohtak district of Southeast Haryana, India

Joga Singh[a] , Amanjeet[b], Ajay Kumar[c] , Jaspal Singh[b] and Gurinderpal Singh[a]
[a] Post Graduate Department of Physics, Khalsa College Amritsar (India)
[b]Department of Applied Sciences, Chandigarh University, Gharuan (India)
[c] Post Graduate Department of Physics, DAV College, Amritsar (India)
jogasingh81@gmail.com

Abstract

Monitoring of radon (^{222}Rn), thoron (^{220}Rn) and their decay products in residential house has been given considerable attention all over the world. In the present investigation, indoor radon, thoron and their progeny concentration levels are measured by means of single entry pin hole dosimeters with LR-115 detectors installed in randomly selected houses of Rohtak district of southeast Haryana during winter season (November 2014 to February 2015). Indoor radon concentration in Rohtak district varies from 8.63 to 25.18 Bq m^{-3} with lowest and highest radon concentrations reported in dwelling of Saman village and kharkara village respectively. Thoron concentration varies from 19.68 to 77.98 Bq m^{-3} with lowest and highest thoron concentrations reported in dwelling of Rohtak city and Bhaini Maharajpur village respectively. All the dwellings in the region have the radon concentration below the level of concern i.e. 150 Bq/m^3 and lower than the action level 200-600 Bq/m^3 recommended by ICRP. The values of radon and thoron progeny are also found to be below the recommended maximum level. The lifetime fatality risk of the residents of the study area varies from 0.12 $x10^{-4}$ to 0.34 $x10^{-4}$ and effective dose varies from 0.72 mSv y^{-1} to 2.23 mSv y^{-1}.

Keywords

Radon, Thoron, Single entry pin hole dosimeter, LR-115 detectors.

I. Introduction

Radon (^{222}Rn) is a radioactive colourless, odourless and noble gas which is the decay product of ^{226}Ra. Radium is one of the elements of the ^{238}U decay series. Radon and its daughter products are responsible for lungs cancer. The most important progenies of Radon are ^{214}Po and ^{218}Po as they are inhaled into lungs. [1]. It is present everywhere in the environment because of inert gas. Radon enters into the house through cracks, construction joints, gaps in floors, gaps around service pipes and cavities inside walls and building construction materials .As radon progenies like ^{214}Po and ^{218}Po are inhaled, they can mutate the cells in the lungs. These alterations can increase the chances of lungs cancer [2]. Radon, thoron and their progenies present in the environment contribute the maximum of the natural radiation dose to the occupational workers and general public [3]. A measurement of Radon, thoron and their progeny exposure is due to their detrimental effects on the health of the inhabitants because, precisely, out of 98% of average radiation dose received by man is from natural sources [4]. For smokers, there is a strong correlation between the radon concentration at home and lung cancer. The absolute risk to smokers and recent ex-smokers is much greater than lifelong non-smokers. Radon in the home accounts for about 9% of deaths from lung cancer and about 2% of all deaths from cancer in Europe [5].

Generally, the thoron concentration in dwellings is considered negligible because of the short lifetime of the thoron (55.6 sec). The worldwide average estimated by UNSCEAR is 3 Bq m^{-3} [4]. While calculating the risk, the contribution of thoron and its progeny can not be ignored. As such the radon measurements should be accompanied by the thoron measurement for assessment of the correct level of dose due to radionuclide present in the environment [6].

II. Geology of Study Area

Haryana is a landlocked state in northern India. It is located between 27°39' and 30°35' N latitude and between 74°28' and 77°36' E longitude. The altitude of Haryana varies between 700 and 3600 ft. (200 m and 1200 m) above sea level. The State of Haryana is located in the north-western

part of India. The river Yamuna flows on the eastern boundary of the State. The Shivalik mountain range flanks the State on its north; the State of Himachal Pradesh is also on its northern side. On the western side, it is flanked by the State of Punjab. At the southern side, the State is flanked by the Aravalli Hills and the desert of Rajasthan. On the eastern side, Uttar Pradesh is the neighbouring State, which touches it only for a limited length. Haryana has four main geographical features: The Yamuna-Ghaggar plain forming the largest part of the state,the Shivalik Hills to the northeast, semi-desert sandy plain to the southwest, the Aravalli range in the south [7].

Rohtak is located in Haryana state of india between 28° 40' 30" to 29° 05'35" north latitude and 76°13' 22" to 76° 51' 20" east latitude (Figure 1). The altitude of district is about 220 meter from mean sea level. There is a gentle slope from north to south i.e.19 cm per km upto Jhajjar town in the northern part of the rohtak and there is considerable slope west to east. Jawahar Lal Nehru feeder and Bhalaut sub Branch are main canals. The district area is occupied by Indo-Gangetic alluvium. There is no surface features worth to mention. Physiographically the area is flat terrain. The area slopes towards northeast to southwest with an average gradient of 0.19 m/km. The soils of the district are fine to medium textured. It comprises sandy loam in Rohtak, Sampla, and Lakhan Majra blocks whereas it is loamy sand with occasional clay loam in Kalanaur and Meham Blocks. The soils of the district are classified as arid brown (Solemnized) and sierozem.

Fig. 1.Map of the study area.

III. Materials and Methods

The pin hole dosimeters (Fig. 2 (a) & (b)) has been used for measuring radon, thoron and their progeny levels in dwellings of Rohtak district of Haryana which were developed and calibrated at Environmental Assessment Division, BARC, Mumbai.

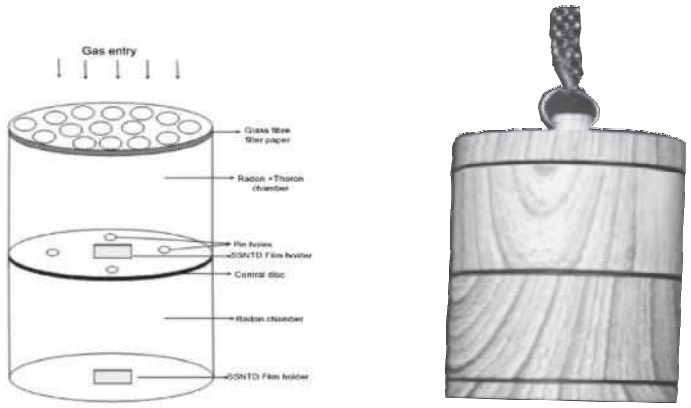

(a) *Fig. 2* (b)

Mostly, for indoor measurement a special detector film, particularly suitable for the spark counter, manufactured by Kodak under the trade name LR-115 is used. This detector consists of thin films of cellulose nitrate colored deep red and coated on 100 mm thick polyester backing. These detectors are kept inside a pin hole dosimeter, a cylindrical plastic chamber divided into two equal compartments, each having an inner volume of 135 cm^3 and height 4.5cm. The two equal compartments on both sides are filter and pinhole compartments. There is one small compartment at the external middle attached to it which is used for bare mode exposure. Films are then inserted at the three compartments by which tracks are recorded. In the filter cup, filter paper is used to cover the entry point of the compartment blocking the entry of the progeny while it allows both radon and thoron gas to pass through. In the pinhole side, we have a pinhole in which only radon gas passes through. One filter paper is used to cover the entry point to block the progenies. In bare mode, as is clear from its name, the film is being exposed barely to the environment and tracks on it are due to radon gas, thoron gas and their progenies. Dosimeters are hanged overhead on the ceiling at the height of minimum 1.5 m from the floor and

at least 10 cm away from any surface. The room size, distance of the dosimeter from roof, wall and floor, and size of the ventilations present at that specific room are measured. The number of windows, ventilations and doors are also counted. This contributes to the ventilation rate of air inside the specific room. The exposed films are then etched in an etching bath using 2.5N NaOH solution at 60ºC for 90 mins during which 4μm thickness is etched away. Etching of the film is necessary because the tracks produced on the films are visible for counting only after etching. The tracks recorded on LR-115 detectors are counted using spark counter. Background track density of an unexposed detector has also been counted. The corrected track density is then obtained by subtracting the number of tracks on an unexposed detector from the exposed detector. The corrected tracks will be converted to radon and thoron gas concentrations using the following equations [8].

$$C_R\ (Bq/m^3) = \frac{(T_1)}{K_R.d} \tag{1}$$

$$C_T(Bq/m^3) = \frac{(T_2 - d.C_R \times K_R^{'})}{K_T.d} \tag{2}$$

Where C_R and C_T are the concentration of radon and thoron (in Bq/m^3) respectively, T_1 is the track density of detector in radon chamber (in tracks/cm^2),K_R is the calibration factor of radon in radon chamber (in tracks.$cm^{-2}d^{-1}$/Bq.m^{-3}),d is the time of exposure (in days), T_2 is the track density of detector in thoron chamber (in tracks/cm^2), $K_R^{'}$ is the calibration factor of radon in radon chamber (in tracks.$cm^{-2}d^{-1}$/Bq.m^{-3}) and K_T is the calibration factor for thoron in thoron chamber (in tracks.$cm^{-2}d^{-1}$/Bq.m^{-3}). The numeric values of these factors are given below:

K_R=0.0170 tracks.$cm^{-2}d^{-1}$/Bq.m^{-3}

K_T=*0.010* tracks.$cm^{-2}d^{-1}$/Bq.m^{-3}

K'_R = 0.0172 tracks.$cm^{-2}d^{-1}$/Bq.m^{-3}

The Annual effective dose (indoor inhalation dose received) due to ^{222}Rn and its progeny and ^{220}Rn and its progeny, has been estimated using the following relation [9].

$$D = \{(0.17+9F_R)C_R + 0.11+32F_T)C_T\} \times 7000 \times 10^{-6} \tag{3}$$

F_R=Equilibrium factor for radon=0.4

F_T= Equilibrium factor for thoron=0.1

Progeny level of radon: PAEC (WL)= C_R (Bq/m^3) × F_R/3700 (4)

Progeny level of thoron: PAEC (WL)= C_T (Bq/m^3) × F_T/3700 (5)

The Conversion of equilibrium equivalent concentration, EEC_{Rn} (**Bq m^{-3}**) into annual exposure to the workers was calculated by using 1 **Bq m^{-3}**=0.00445 WLM. The conversion factor for Life Time Fatality risk is 3×10^{-4} [10].

IV. Results And Discussion

The values of radon, thoron and their progeny concentration, life time fatality risk and annual effective dose in dwellings of Rohtak district of Haryana, Northern India (Figure 1) measured in the winter season (November 2014 to February 2015) are tabulated in Table 1. The indoor radon and thoron levels in this area are found to vary from 8.63 to 25.18 Bq m^{-3} and 19.68 to 77.98 Bq m^{-3} with an average value of 16.52 Bq m^{-3} and 33.38 Bq m^{-3} respectively with standard deviations of 5.38 and 17.79 respectively . The lowest value of radon concentration (8.63 Bq m^{-3}) is found in dwelling of Kharkara village which is well ventilated with two windows and one door while the highest value of radon concentration (25.18 Bq m^{-3}) is found in dwelling of Saman village which is poorly ventilated with only one door and no windows. Radon concentration concentration depends on variation in ventilation conditions, type of construction and other factors such as temperature, humidity etc. A well ventilated house has low radon concentration as compared to poorly ventilated house. This is because in well ventilated dwellings the radon can easily escape out and hence does not accumulate inside so the radon level inside becomes lower in well ventilated houses in comparison to poorly ventilated houses [11]. In the study area, most of the dwellings consist of brick walls, concrete roofs and cemented floors. So contribution to the building material is almost same for all the dwellings. The average value of radon concentration in study area (25.18 Bq m^{-3}) is lower than the average value of 40 Bq m^{-3} reported for the dwellings worldwide [4]. This may be due to low concentration of radioactive elements, viz. uranium and radium

in the soil and building materials of the study area. However, all the dwellings have the radon concentration below the level of concern *i.e.* 150 Bq m^{-3} and lower than the action level 200-600 Bq m^{-3} recommended by ICRP [12]. The variation of radon concentration in dwelling of study area are shown in Figure 3.

The values of thoron concentration were found to vary from 19.68 Bq m^{-3} to 77.94 Bq m^{-3}. The lowest value of thoron concentration (19.68 Bq m^{-3}) is found in dwelling of Rohtak City and highest concentration of thoron (77.94 Bq m^{-3}) is found in dwelling of Bhaini Maharajpur village with an average value of 33.38 Bq m^{-3} as shown in figure 4. The observed values of radon and thoron concentration in the study area are found to be lower than that reported by Deepak Verma et.al. [11] in Bareilly area, M.Shakir Khan et.al.[13] in Kanshiram Nagar (Uttar Pardesh) area, Jyoti Sharma et.al.[14] in Jaipur area and S. Shobha et.al.[15] in Banglore city.

Annual effective dose in the study area varies from 0.72 mSv y^{-1} to 2.23 mSv y^{-1} in Kharkara village and Bhaini Maharajpur village respectively. The values of effective dose in all dwellings of study area are found to be lower than the action level 3-10 mSv y^{-1} recommended by ICRP [12].The lifetime fatality risk of the residents of the study area varies from 0.12 $x10^{-4}$ to 0.34 $x10^{-4}$ with an average of 0.22 $x10^{-4}$ and a standard deviation of 0.07. The values of radon and thoron concentration vary from 0.9 mWL to 2.7mWL and from 0.5mWL to 2.1mWL respectively. The maximum value of radon progeny (2.7mWL) and thoron progeny (2.1 mWL) found in the present study is below the recommended maximum level of 21.5 mWL in India [16] as shown in Table 2. Statistics of different measured parameters for study area are shown in Table 3.

Table 1: Radon, Thoron Concentration and Indoor inhalation rate in Dwellings of study area.

Village Name	No.of Dwellings	Radon Concentration (Bq m^{-3})	Thoron concentration (Bq m^{-3})	Effective Dose (mSv y^{-1})
Bhaini Bharav	10	18.60	40.54	1.43
Bhaini Maharajpur	7	16.25	77.94	2.23
Saman	6	25.18	29.84	1.36
Bhaini Chanderpal	8	16.84	26.52	1.06
Meham	10	18.12	24.60	1.05
Badi Bahu	9	11.81	29.95	1.00
Rohtak City	10	22.35	19.68	1.04
Farmana	6	10.94	30.21	0.99
Kharkara	6	8.63	21.15	0.72
Average Value		16.52	33.38	1.21

Village Name	Progeny Level of Radon (mWL)	Progeny Level of Thoron (mWL)	Annual Exposure(WLM)	Life Time Fatality Risk ($\times 10^{-4}$)
Bhaini Bharav	2.05	1.09	0.08	0.25
Bhaini Maharajpur	1.80	2.10	0.07	0.22
Saman	2.70	0.80	0.11	0.34
Bhaini Chanderpal	1.80	0.70	0.07	0.22
Meham	1.90	0.70	0.08	0.24
Badi Bahu	1.30	0.80	0.05	0.16
Rohtak City	2.40	0.50	0.10	0.30
Farmana	1.20	0.80	0.05	0.15
Kharkara	0.90	0.60	0.04	0.12
Average Value	1.79	0.90	0.07	0.22

Table 3: Statistics of different measured parameters for study area

Different Measured Parameters	MIN	MAX	SD	GM	Median
Radon Concentration (Bq m^{-3})	8.62	25.18	5.38	15.69	16.84
Thoron concentration (Bq m^{-3})	19.67	77.93	17.79	30.54	29.84
Indoor inhalation rate (mSv/y)	0.72	2.23	0.43	1.15	1.04
Progeny Level of Radon (mWL)	0.92	2.7	0.58	1.69	1.8
Progeny Level of Thoron (mWL)	0.53	2.10	0.48	0.82	0.80
Annual Exposure(WLM)	0.04	0.11	0.02	0.07	0.07
Life Time Fatality Risk	0.11	0.33	0.07	0.20	0.22

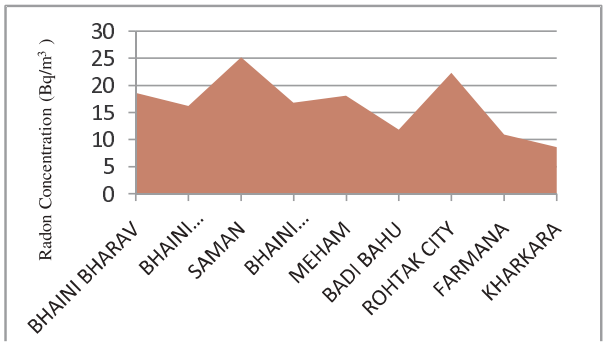

Fig. 3:Radon concentration in dwellings of study area.

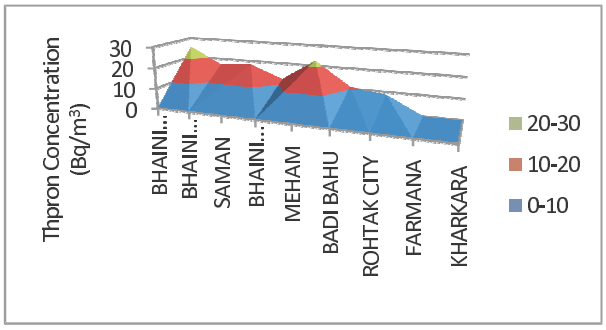

Fig.4:Thoron concentration in dwellings of study area.

V. Conclusion

In this investigation, radon concentration levels in a large number of randomly selected dwellings in Southeast Haryana during winter season are reported. The following conclusions are drawn:

1. The overall average value of radon in the present study (16.52 Bq/m^3) is found to be lower than the world average value of indoor radon level (40 Bq m^{-3}).Overall, the observed values of radon concentration in all the dwellings are lower than the action level (200-600 Bq m^{-3}) recommended by ICRP.
2. The maximum value of radon progeny (2.7 mWL) and thoron progeny (2.1 mWL) have been found to be lower than the action limit of 21.50 mWL for Indian dwellings.
3. The values of effective dose in all dwellings of study area are found to be lower than the action level 3-10 mSv/y recommended by ICRP.
4. The lifetime fatality risk of the residents of the study area varies from 0.12×10^{-4} to 0.34×10^{-4} with an average of 0.22×10^{-4}.

VI. References

[1] Z.A. Hussein, M.S. Jaafa and A.H. Ismail, Measurement of indoor Radon-222 Concentration inside Iraqi Kurdistan:Case Study in the Summer Season J Nucl Med Radiat Ther. Doi:10.4172/2155-9619.1000143 (2013).

[2] O. Abu-Haija, B. Salameh, A. W. Ajlouni, M. Abdelsalam and H. Al-Ebaisat, Measurement of radon concentration inside houses in Tafila Province, Jordan International Journal of the Physical Sciences 5(6)(2010) 696-699.

[3] K. Kant, Rashmi, R.G. Sonkawade, G.S. Sharma and R.P. Chauhan , Seasonal variation of radon, thoron and their progeny levels in dwellings of Haryana and Western Uttar Pradesh, Iran J. Radiat. Res. 7 (2)(2009)79-84.

[4] UNSCEAR, United Nation Scientific Committee on the Effects of Atomic Radiation. Sources and Effects of Ionizing Radiation, United Nations: New York (2000).

[5] S. Darby, D. Hill, A. Auvinen, J. M. Barros-Dios, H. Baysson, F. Bochicchio, H. Deo, R. Falk, F. Forastiere, M. Hakama, I. Heid, L. Kreienbrock, M. Kreuzer, F. Lagarde, I. Mäkeläinen, C. Muirhead,W. Oberaigner, G. Pershagen, A. Ruano-Ravina, E. Ruosteenoja, A. Schaffrath Rosario, M. Tirmarche, L. TomáBek, E. Whitley, H. E. Wichmann, R. Doll, Radon in homes and risk of lung cancer:

collaborative analysis of individual data from 13 European case-control studies BMJ, doi:10.1136/bmj.38308.477650.63, 2004.

[6] R.C. Ramola and T.V. Ramachandran, Variation of Radon and Thoron Levels in Garhwal Homes Japan Health Physics Society, Tokyo, Japan, 32(15)(2000).

[7] M. Shakir Khan and Ameer Azam, Measurements of indoor radon, thoron, and their progeny using twin cup dosimeters in rural areas of Northern India Environ Earth Sci 71(2013) 1319-1325.

[8] B.K.Sahoo Verma, B.K. Sapra, S.D. Kanse, J.J. Gaware and Y.S. Mayya, A New Pin-Hole Discriminated 222Rn/220Rn Passive Measurement Device with Single Entry Face Radiation Measurements 58 (2013) 5260.

[9] V. Mehta, S. P. Singh, R. P. Chauhan and G. S. Mudahar, Measurement Of Indoor Radon, Thoron and their Progeny Levels in Dwellings of Ambala District, Haryana, Northern India Using Solid State Nuclear Track Detectors Rom. Journ. Phys. 59, Nos. 78 (2014) 834845.

[10] K. Kant and S. K. Chakarvarti, Radiological Impact of Airborn Radon and its Progeny in Dwellings, Indian Journal of Pure & Applied Physics 42 (2004) 157-161.

[11] D. Verma and M. Shakir Khan, Assessement of Indoor Radon, Thoron and Their Progeny in Dwellings of Bareilly City of Northern India Using Track Etch Detectors Rom. Journ. Phys. 59, Nos. 12 (2014)172182.

[12] ICRP, International Commission on Radiological Protection, ICRP Publication No. 65 Pergamon Press, Oxford (1993).

[13] M.Shakir Khan and A. Azam, Measurements of indoor radon, thoron, and their progeny using twin cup dosimeters in rural areas of Northern India Environ Earth Sci. 71 (2013) 1319-1325.

[14] Jyoti Sharma, A. K. Mahur, Rupesh Kumar, Rati Varshney, R. G. Sonkawade, R. Swarup ,Hargyan Singh and Rajendra Prasad, Comparative study of indoor radon, thoron with radon exhalation rate in soil samples in some historical places at Jaipur, Rajasthan, India Advances in Applied Science Research,3 (2)(2012)1085-1091.

[15] S. Shobha , L.A. Sathish, S. Sundareshan and T.V. Ramachandran, Inhalation Dose Due to Indoor Radon International Journal of Pure and Applied Physics 6(3)(2010) 257262.

[16] T.V.Ramachandran, K.P. Eappen, R.N. Nair, A.N. Shaikh, Y.S. Mayya and V.D. Puranik, Distribution pattern of radon and thoron levels and inhalation dose rates in Indian dwellings Proc. 12th National Symp. on Environment 192 (2003).

Curr. Rep. Sci. & Tech. 1 (2) (2015) 62-69

Cytotoxicity of Graphene

Zorawar Singh[a] and Balinder Singh[b]
[a]Department of Zoology, Khalsa College Amritsar (India)
[b]Lecturer in Chemistry (Retd.), GSSS, Khanna (India)
zorawarsinghs@rediffmail.com

Abstract

Graphene has emerged as a sensational nanocarbon with unusual properties. Graphene is a thin layer of pure carbon. It is a single, tightly packed layer of carbon atoms that are bonded together in a hexagonal honeycomb lattice. In more complex terms, it is an allotrope of carbon in the structure of a plane of sp2 bonded atoms with a molecule bond length of 0.142 nanometers. It is the thinnest and lightest material known to man at one atom thickness. In this paper an attempt has been made to compile up the studies related to the cytotoxicity of graphene and its derivatives.

Keywords

Graphene, Graphene family nanomaterials, Cytotoxicity

I. Introduction

Graphene is the strongest compound discovered (between 100-300 times stronger than steel and with a tensile stiffness of 150,000,000 psi), the best conductor of heat at room temperature and also the best conductor of electricity known. In initial tests carried out, laser-scribed graphene (LSG) super capacitors (with graphene being the most electronically conductive material known) were shown to offer power density comparable to that of high-power lithium-ion batteries that are in use today. Not only that, but also LSG super-capacitors are highly flexible, light, quick to charge, thin and as previously mentioned, comparably very inexpensive to produce.It is a zero-overlap semimetal (with both holes and electrons as charge carriers) with very high electrical conductivity. Carbon atoms have a total of 6 electrons; 2 in the inner shell and 4 in the outer shell. The 4 outer shell electrons in an individual carbon atom are available for chemical bonding,

but in graphene, each atom is connected to 3 other carbon atoms on the two dimensional plane, leaving 1 electron freely available in the third dimension for electronic conduction. These highly-mobile electrons are called pi (π) electrons and are located above and below the graphene sheet. These pi orbitals overlap and help to enhance the carbon to carbon bonds in graphene. Fundamentally, the electronic properties of graphene are dictated by the bonding and anti-bonding (the valance and conduction bands) of these pi orbitals.

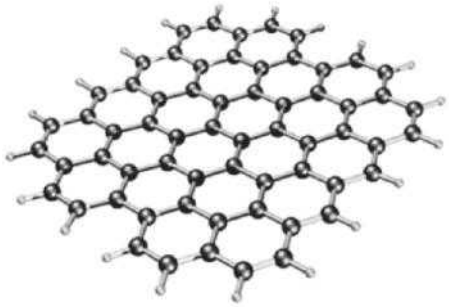

Fig. 1 Structure of graphene [cnx.org]

In recent years, various novel nanomaterials have received much attention due to their great potential for applications in agriculture [1-4]; food safety and food packaging [5-13] and so on. Among them, graphene family nanomaterials (GFNs) are emerging as promising compounds that may have a profound impact on different application fields.

II. Cytotoxicity Studies

Many recent studies were conducted for the assessment of cytotoxic nature of graphene and its derivatives [14-19]. The fabrication of highly pure, colloidally stable, and evenly dispersed Graphene Oxide (GO) in physiologically-relevant aqueous buffers in comparison to conventional GO is investigated. The purified GO material is thoroughly characterized by a battery of techniques, and is shown to consist of single layer GO sheets of lateral dimensions below 500 nm. The cytotoxic impact of the GO in vitro and its inflammation profile in vivo was investigated. The purified GO prepared and characterized here does not induced significant cytotoxic responses in vitro, or inflammation and granuloma formation in vivo following intraperitoneal injection. This is one of the initial steps towards

determination of the safety risks associated with GO material that may be interacting with living tissue [20]. Silver nanoparticles (AgNPs) are increasingly used in daily life for their antibacterial properties, but their low stability and high cytotoxicity hamper practical applications. Sodium 1-naphthalenesulfonate-functionalized reduced graphene oxide (NA-rGO) was used as a substrate for AgNPs to produce AgNP-NA-rGO hybrid. This hybrid showed substantially higher antibacterial activity than polyvinyl pyrrolidone (PVP)-stabilized AgNPs, and the AgNPs on NA-rGO were more stable than the AgNPs on PVP, resulting in long-term antibacterial effects. More importantly, this hybrid showed excellent water solubility and low cytotoxicity, suggesting the great potential application as sprayable reduced graphene oxide based antibacterial solutions [21].

To understand the toxicity profile for a particular type of graphene utilized in a given application, it is important to recognize the differences between the graphene-related components and correlate their cellular toxicity effects to the attributed physiochemical properties. The cytotoxic effects of highly hydrogenated graphene (HHG) and its graphene oxide (GO) counterpart on the basis of in vitro toxicological assessments were reported and the effects were correlated with the physiochemical properties of the tested nanomaterials. Upon 24 h exposure to the nanomaterials, a dose-dependent cellular cytotoxic effect was exhibited and the HHG was observed to be more cytotoxic than its GO control. Detailed characterization revealed an extensive C-H sp3 network on the carbon backbone of HHG with few oxygen-containing groups, as opposed to the presence of large amounts of oxygen-containing groups on the GO. It is therefore hypothesized that the preferential adsorption of micronutrients on the surface of the HHG nanomaterial by means of hydrophobic interactions resulted in a reduction in the bioavailability of nutrients required for cellular viability [18]. PEGylated graphene oxide (PEG-GO) was characterized using Fourier transform infrared spectroscopy (FTIR) and the stability of PEG-GO was detected in different solutions. RAJI cell was selected as a lymphoma cell model to study the cytotoxicity of PEG-GO. Cell viability was detected using the Cell Counting Kit-8 assay. Cells were treated with different concentrations (10-100 mμg/mL) of PEG-GO at different time points (6, 12, and 24 h). The FTIR spectrum of PEG-GO

indicated that polyethylene glycol was successfully grafted onto GO. PEG-GO had excellent stability in all solutions. Cells treated with PEG-GO (10-100 mμg/mL) for 24 hours had survival rates were over 80%. These results demonstrated that PEG-GO had an excellent dispersion in biological solutions and the toxicity of PEG-GO to lymphoma cells was low. This study provided cytological evidence for the application of PEG-GO in medicine [19]. Many recent studies have shown the way nanoparticles interact with cells and biological molecules can vary greatly in the serum-containing or serum-free culture medium. However, the underlying molecular mechanisms of how the so-called "protein corona" formed in serum medium affects nanoparticles' biological responses. Thus, it is critical to understand how absorbed proteins on the surfaces of nanoparticles alter their biological effects. Duan et al.[15] demonstrated with both experimental and theoretical approaches that protein BSA coating can mitigate the cytotoxicity of graphene oxide (GO) by reducing its cell membrane penetration. Cell viability and cellular uptake experiments showed that protein corona decreased cellular uptake of GO, thus significantly mitigating the potential cytotoxicity of GO.

GO nanoplatelets caused dose- and time-dependent cytotoxicity in HepG2 cells with plasma membrane damage and induction of oxidative stress being important modes of toxicity. Both graphene derivatives were internalized by HepG2, a non-phagocytotic cell line. Moreover, they exerted no toxicity when applied at very low concentrations (< 4 mμg/ml). GO nanoplatelets may therefore represent an attractive material for biomedical applications [22]. Graphene and single-walled carbon nanotubes were used to deliver the natural low-toxicity drug gambogic acid (GA) to breast and pancreatic cancer cells in vitro, and the effectiveness of this complex in suppressing cellular integrity was assessed. Cytotoxicity was assessed by measuring lactate dehydrogenase release, mitochondria dehydrogenase activity, mitochondrial membrane depolarization, DNA fragmentation, intracellular lipid content, and membrane permeability/caspase activity. The nanomaterials showed no toxicity at the concentrations used, and the antiproliferative effects of GA were significantly enhanced by nanodelivery. The results suggested that these complexes inhibit human

breast and pancreatic cancer cells grown in vitro. This analysis represented a first step toward assessing their effectiveness in more complex, targeted, nanodelivery systems [23]. Cytoxicities of MDA-MB-231 breast cancer cells (MDA cells) on carbon paste (CP) and graphene-carbon paste (GCP) substrates were also assessed. GCP was prepared by mixing graphene powder into carbon paste with different graphene contents. Cytotoxic effect was evaluated from cell viability, cell adhesion, ROS production and fluorescence staining studies. Cell viability on GCP substrate was found to initially increase as graphene content increases from 0 to 2.5 wt% but then decrease as the content increases further. In addition, the viability decreased with time for all substrates. Similarly, graphene concentration affected the number of adherent cells in the same manner as the cell viability. Likewise, reactive oxygen species (ROS) induced by carbon substrate increased with time and decreased with small graphene inclusion, confirming that low graphene content led to lower cytotoxicity. Moreover, confluence of MDA cells on substrate evaluated using Hoechst 33342 fluorescence staining was also found to be enhanced at low graphene concentration. Therefore, low-content graphene incorporation can effectively improve biocompatibility of carbon-based materials with MDA-MB-231 breast cancer cells, enabling potential applications such as electrochemical electrode for cell study [24]. Cytotoxicity and genotoxicity of GO to HLF cells were concentration dependent, and the genotoxicity induced by GO was more severe than the cytotoxicity to HLF cells. Oxidative stress mediated by GO might explain the reason of its toxic effect. Furthermore, the electronic charge on the surface of GO is thought to play an important role in the toxicity of GO to HLF cells [25].

III. Conclusion

After going through the papers related to the cytotoxicity of graphene and its derivatives, it is clear that graphene has many possible uses in different fields of medical and agricultural sciences, but also comes with the factor of toxicity. Before using graphene in any medical field, it is recommended that the nanocomposite being used on biological system should be checked for its toxicity.

IV. References

[1] M. R. Hill, E. J. MacKrell, C. P. Forsthoefel, S. P. Jensen, M. Chen, G. A. Moore, Z. L. He, and B. S. Sumerlin, "Biodegradable and pH-responsive nanoparticles designed for site-specific delivery in agriculture," Biomacromolecules16 (2015)1276-1282.

[2] S. Mishra and H. B. Singh, "Biosynthesized silver nanoparticles as a nanoweapon against phytopathogens: exploring their scope and potential in agriculture," Appl. Microbiol. Biotechnol.99 (2015) 1097-1107.

[3] S. Sabir, M. Arshad, and S. K. Chaudhari, "Zinc oxide nanoparticles for revolutionizing agriculture: synthesis and applications," ScientificWorldJournal.2014 (2014) 925494.

[4] O. Cota-Arriola, M. O. Cortez-Rocha, A. Burgos-Hernandez, J. M. Ezquerra-Brauer, and M. Plascencia-Jatomea, "Controlled release matrices and micro/nanoparticles of chitosan with antimicrobial potential: development of new strategies for microbial control in agriculture," J. Sci. Food Agric.93 (2013) 1525-1536.

[5] A. A. Becaro, F. C. Puti, D. S. Correa, E. C. Paris, J. M. Marconcini, and M. D. Ferreira, "Polyethylene Films Containing Silver Nanoparticles for Applications in Food Packaging: Characterization of Physico-Chemical and Anti-Microbial Properties," J. Nanosci. Nanotechnol.15 (2015) 2148-2156.

[6] L. Pathak, A. Kanwal, and Y. Agrawal, "Curcumin loaded self assembled lipid-biopolymer nanoparticles for functional food applications," J. Food Sci. Technol.52 (2015) 6143-6156.

[7] M. Roushani, S. Abbasi, and H. Khani, "Synthesis and application of ion-imprinted polymer nanoparticles for the extraction and preconcentration of mercury in water and food samples employing cold vapor atomic absorption spectrometry," Environ. Monit. Assess.187 (2015) 4820.

[8] C. Krishnaraj, S. L. Harper, H. S. Choe, K. P. Kim, and S. I. Yun, "Mechanistic aspects of biologically synthesized silver nanoparticles against food- and water-borne microbes," Bioprocess. Biosyst. Eng. 38 (2015) 1943-1958.

[9] C. Ruiz-Palomero, M. L. Soriano, and M. Valcarcel, "Sulfonated

nanocellulose for the efficient dispersive micro solid-phase extraction and determination of silver nanoparticles in food products," *J. Chromatogr. A*, (2015)doi: 10.1016/j.chroma.2015.06.023.

[10] Z. M. Song, N. Chen, J. H. Liu, H. Tang, X. Deng, W. S. Xi, K. Han, A. Cao, Y. Liu, and H. Wang, "Biological effect of food additive titanium dioxide nanoparticles on intestine: an in vitro study," J. Appl. Toxicol.35 (2015)1169-1178.

[11] R. Jacobs, d. van, V, and C. J. Ter Braak, "Integrated probabilistic risk assessment for nanoparticles: the case of nanosilica in food," J. Nanopart. Res.17 (2015)251.

[12] H. Wang, X. Guo, S. Fu, T. Yang, Y. Wen, and H. Yang, "Optimized core-shell Au@Ag nanoparticles for label-free Raman determination of trace Rhodamine B with cancer risk in food product," Food Chem.188 (2015) 137-142.

[13] D. Lichtenstein, J. Ebmeyer, P. Knappe, S. Juling, L. Bohmert, S. Selve, B. Niemann, A. Braeuning, A. F. Thunemann, and A. Lampen, "Impact of food components during in vitro digestion of silver nanoparticles on cellular uptake and cytotoxicity in intestinal cells," Biol. Chem.(2015)doi: 10.1515/hsz-2015-0145.

[14] Y. Chong, C. Ge, Z. Yang, J. A. Garate, Z. Gu, J. K. Weber, J. Liu, and R. Zhou, "Reduced Cytotoxicity of Graphene Nanosheets Mediated by Blood-Protein Coating," ACS Nano.9 (2015) 5713-5724.

[15] G. Duan, S. G. Kang, X. Tian, J. A. Garate, L. Zhao, C. Ge, and R. Zhou, "Protein corona mitigates the cytotoxicity of graphene oxide by reducing its physical interaction with cell membrane," Nanoscale.7 (2015) 15214-15224.

[16] J. Wu, R. Yang, L. Zhang, Z. Fan, and S. Liu, "Cytotoxicity effect of graphene oxide on human MDA-MB-231 cells," Toxicol. Mech. Methods25 (2015)312-319.

[17] W. Zhang, L. Yan, M. Li, R. Zhao, X. Yang, T. Ji, Z. Gu, J. J. Yin, X. Gao, and G. Nie, "Deciphering the underlying mechanisms of oxidation-state dependent cytotoxicity of graphene oxide on mammalian cells," Toxicol. Lett.237 (2015) 61-71.

[18] E. L. Chng, Z. Sofer, and M. Pumera, "Cytotoxicity profile of highly hydrogenated graphene," *Chemistry.*20 (2014) 6366-6373.

[19] L. Du, S. Wu, Y. Li, X. Zhao, X. Ju, and Y. Wang, "Cytotoxicity of PEGylated graphene oxide on lymphoma cells," Biomed. Mater. Eng. 24 (2014) 2135-2141.

[20] H. Ali-Boucetta, D. Bitounis, R. Raveendran-Nair, A. Servant, J. Van den Bossche, and K. Kostarelos, "Purified graphene oxide dispersions lack in vitro cytotoxicity and in vivo pathogenicity," Adv. Healthc. Mater.2 (2013)433-441.

[21] X. Cai, S. Tan, A. Yu, J. Zhang, J. Liu, W. Mai, and Z. Jiang, "Sodium 1-naphthalenesulfonate-functionalized reduced graphene oxide stabilizes silver nanoparticles with lower cytotoxicity and long-term antibacterial activity," Chem. Asian J. 7 (2012) 1664-1670.

[22] T. Lammel, P. Boisseaux, M. L. Fernandez-Cruz, and J. M. Navas, "Internalization and cytotoxicity of graphene oxide and carboxyl graphene nanoplatelets in the human hepatocellular carcinoma cell line Hep G2," Part Fibre. Toxicol.10 (2013) 27.

[23] L. M. Saeed, M. Mahmood, S. J. Pyrek, T. Fahmi, Y. Xu, T. Mustafa, Z. A. Nima, S. M. Bratton, D. Casciano, E. Dervishi, A. Radominska-Pandya, and A. S. Biris, "Single-walled carbon nanotube and graphene nanodelivery of gambogic acid increases its cytotoxicity in breast and pancreatic cancer cells," J Appl. Toxicol.34 (2014) 1188-1199.

[24] U. Waiwijit, W. Kandhavivorn, B. Oonkhanond, T. Lomas, D. Phokaratkul, A. Wisitsoraat, and A. Tuantranont, "Cytotoxicity assessment of MDA-MB-231 breast cancer cells on screen-printed graphene-carbon paste substrate," Colloids Surf. B Biointerfaces.113 (2014) 190-197.

[25] A. Wang, K. Pu, B. Dong, Y. Liu, L. Zhang, Z. Zhang, W. Duan, and Y. Zhu, "Role of surface charge and oxidative stress in cytotoxicity and genotoxicity of graphene oxide towards human lung fibroblast cells," J Appl. Toxicol.33 (2013) 1156-1164.

Curr. Rep. Sci. & Tech. 1 (2) (2015) 70-77

Indoor Radon and Thoron Estimates in District Hamirpur, Himachal Pradesh, India

Parminder Singh and B.S. Bajwa
Department of Physics, Guru Nanak Dev University, Amritsar (India)
parminderphy@gmail.com

Abstract

In the present investigation indoor radon (^{222}Rn), thoron (^{220}Rn) and their progeny concentrations have been measured in the wide range of dwellings from 12 different villages of Hamirpur district, Himachal Pradesh, India by using LR-115 type-II based Pin-hole Radon-Thoron discriminating twin cup dosimeters, direct radon and thoron progeny sensors (DRPS/DTPS). As inhalation doses are predominantly due to daughter products of radon and thoron and not due to gases, it is important to measure the decay products directly for health risk assessments. In the study region different types of houses were selected randomly according to methodologies described by Radiological Physics and Advisory Division (RPAD), Bhaba Atomic Research Centre (BARC), Mumbai. The indoor radon concentrations in these dwellings have been found vary from 22 to 573 Bq/m^3, with average value of 113.4 Bq/m^3 and for thoron vary from 10 to 739 Bq/m^3, with average value of 116.1 Bq/m^3. The progeny concentrations of radon and thoron are found within the limits of 8 to 141 Bq/m^3 and 0.5 to 15.2 Bq/m^3 respectively, with average values 36.9 Bq/m^3 and 3.2 Bq/m^3 respectively. The average concentration values observed in these dwellings have been found within the safe limits as recommended by International Commission on Radiological Protection (ICRP) and United Nation Scientific Committee on the Effect of Atomic Radiation (UNSCEAR).

Keywords

Radon, Thoron, Progeny concentration, Dosimeter

I. Introduction

Measurement of indoor radon, thoron and their daughter products is

an important aspect as they contribute more than the 50% of total radiation dose inhaled by human beings from natural radioactive sources [1]. After smoking radon is the second main cause of lung cancer in human population [2]. Radon (^{222}Rn) and thoron (^{220}Rn) with half life 3.82 days and 55.2 seconds are decay products of naturally occurring radioactive elements ^{238}U and ^{235}Th respectively. The contribution of radiation dose by thoron is negligible as compared to radon because of short half life but decay products of radon and thoron are more harmful and then they cannot be neglected [3,4]. The alpha emitting, short lived daughter products of radon (^{218}Po, ^{214}Pb and ^{214}Bi) and thoron (^{212}Pb and ^{212}Bi) are present everywhere in environment in attached or unattached fractions of air particles. During inhalation main fraction of these daughter products stay in lungs and irradiate the bronchial target cells by emission of alpha particles, which results in bronchial carcinomas [2-6] and sometimes causes lung cancer [7,8].

The main sources of indoor radon, thoron and their decay products are the soil-gas, minerals and rocks in earth's crust, building material and ground water [9]. The construction type of houses, type of soil, ventilation rate, atmospheric pressure and temperature also have a significant role in indoor gas measurements [10,11]. In the present study latest passive techniques have been used in the dwellings of Hamirpur district Himachal Pradesh for indoor radon, thoron and their progeny concentration measurements, using LR-115 (type II) plastic track detectors and Direct Progeny Sensors (DRPS/DTPS) as developed and recommended by Radiation Protection Advisory Division (RPAD) [12-14], BARC, Mumbai.

II. Geology of The Area

The area of study region is Hamirpur district in Himachal Pradesh (HP) extends from 31.27˚ to 32.10˚ North latitudes and from 75.80˚ to 76.52˚ East longitudes. HP is bounded from west and north by Jammu and Kashmir, east by Uttrakhand and in the south by Punjab. It is highly hilly area and population is very low. Soil contains large number of minerals and rocks, which contribute to radon, thoron and other radioactive gases.

III. Experimental Techniques

The measurement of radon, thoron and their progeny concentrations

have been carried out by latest passive techniques developed by RPAD, BARC, Mumbai, using LR-115 type II plastic track detectors. Indoor radon and thoron concentrations are calculated using pin hole based twin cup dosimeters suspended inside the dwellings such that they are 30 cm away from any surface. Progeny concentrations are also calculated by suspending DRPS/DTPS in the indoor environment away from any door and window. The Pelliculable LR-115 of size 3 cm x 3 cm have been fixed on holders provided in dosimeters. After exposure for three months, the detectors were retrieved from dosimeters and etched in 2.5 N NaOH solution for 90 minutes at 60˚C in a water bath without stirring. After etching and drying, the detector should be peeled off from its cellulose acetate base and the track counting can be done under spark counter Model PSI-SC 1. The operating as well as the pre-sparking voltage of the spark counter has been established prior to these measurements.

A. Pin-hole Based Twin Cup Dosimeters

The newly designed this dosimeter has two compartments separated by a central pin-holesdisc, acting as thoron discriminator. Four pin holes each with dimension of 2 mm length and 1 mm diameter are made in this circular disc. The schematic diagram of the dosimeter is shown in Fig. 1. The dosimeter has a single entry through which gas enters the first chamber namely "radon+thoron" chamber through a glass fiber filter paper (thickness 0.56 μm) and subsequently diffuses to second chamber namely "radon" chamber through pin-holes cutting off the entry of thoron into this chamber due to its short half life. Each chamber is cylindrical having a length of 4.1 cm and radius 3.1cm. Chambers are internally coated with metallic powders to have zero electric field inside the chamber volume, so that the deposition of progenies formed from gases will be uniform throughout the volume. The radon (C_R) and thoron (C_T) concentrations are calculated by following relations [12]:

$$C_R\,(Bq/m^3) = T_1/(d.k_r) \quad (1)$$

$$C_T\,(Bq/m^3) = (T_2 - d.C_r k_r)/(d.k_t) \quad (2)$$

where, d is the number of days of exposure, T_1 and T_2 are the track densities (in tracks/cm^2) observed in 'radon' and 'radon+thoron'

compartment respectively, k_r and k_t are the calibration factors for radon in 'radon' compartment and thoron in 'radon+thoron' compartment respectively. The values of these factors are as follows:

$k_r = 0.019 \pm 0.003$ tracks. $Cm^{-2}/Bq.d.m^{-3}$

$k_t = 0.016 \pm 0.005$ tracks. $Cm^{-2}/Bq.d.m^{-3}$

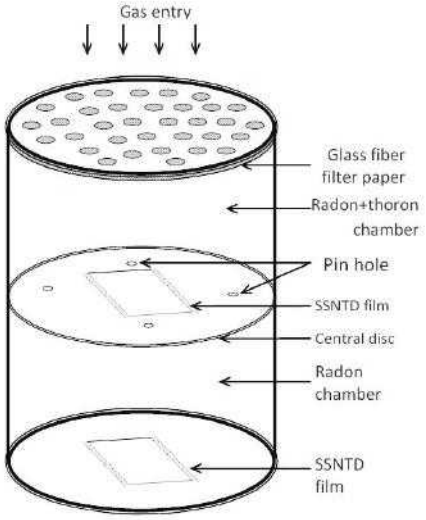

Fig. 1 *Pin hole based twin cup radon/thoron discriminating dosimeter*

Table 1. *Average Indoor radon, thoron and their progeny concentrations at different locations in Hamirpur district of Himachal Pradesh.*

Sr. No.	Location	Radon Conc. (Bq/m^3)	Thoron Conc. (Bq/m^3)	Radon Progeny Conc. (Bq/m^3)	Thoron Progeny Conc. (Bq/m^3)
1.	Chakrauli	176.1	316.1	72.8	4.4
2.	Romera	272.0	201.1	51.6	3.7
3.	Khaya	99.8	119.4	39.3	2.5
4.	Loharian	147.1	67.9	62.8	4.4
5.	Hamirpur	51.7	38.5	10.5	0.9
6.	Tikker	103.1	97.9	39.4	5.2
7.	Galore Khas	36.1	53.3	10.8	1.0
8.	Badsar	40.3	54.5	13.7	1.2
9.	Galote	214.8	331.1	106.9	6.0
10.	Chakmoh	71.3	117.3	27.9	3.0
11.	Baroha	116.0	78.8	26.1	3.7
12.	Asthota	133.4	144.9	39.4	4.0
	Average	113.4	116.1	36.9	3.2

B. Direct Radon/Thoron Progeny Sensors

Deposition based Direct Radon and Thoron progeny sensors (DRPS and DTPS) have been developed for measurement of radon and thoron progeny concentration in the environment. These are made of passive nuclear track detectors (LR-115) mounted with absorbers of appropriate thickness. For thoron progeny, the absorber is 50 μm aluminized mylar which selectively detects only 8.78 MeV α- particles emitted from ^{212}Po; while for radon progeny, the absorber is a combination of aluminized mylar and cellulose nitrate of effective thickness 37 μm to detect mainly 7.69 MeV α-particles emitted from ^{214}Po. The tracks recorded in the exposed LR-115 film are related to Equilibrium Equivalent Progeny Concentration (EEC) using the sensitivity factor. The number of tracks per unit area per unit time (T) can be correlated to the Equilibrium Equivalent Progeny Concentration (EEC) [14] in air using the Sensitivity factor (S) as:

$$EEC\,(Bq.m^{-3}) = T\,(Tracks.cm^{-2}.d^{-1}) / S\,(Tracks.cm^{-2}.d^{-1})/EEC\,(Bq.m^{3}) \quad (3)$$

Where sensitivity factor (S) for DTPS is 0.94 (Tracks.cm^{-2}.d^{-1})/EEC (Bq.m^{-3}) to measure thoron progeny and to find radon progeny concentration the sensitivity factor for DRPS is 0.09 (Tracks.cm^{-2}.d^{-1})/EEC (Bq.m^{-3}).

IV. Results and Discussion

The indoor concentration of radon, thoron and their daughter products in the winter season at different locations of Hamirpur district Himachal Pradesh are calculated by using latest developed pin hole based twin cup

Table 2. *Concentration of radon, thoron and their progenies in A type and B type houses*

S. No.	Types of Dwellings	No. of Dwellings	Avg. Radon Conc. (Bq/m^3)	Avg. Thoron Conc. (Bq/m^3)	Avg. Radon Progeny Conc. (Bq/m^3)	Avg. Thoron Progeny Conc. (Bq/m^3)
1.	(A) Mud houses/ poor ventilation	25	136. 5	145.7	53.6	6.2
2.	(B) Concrete houses/ good ventilation	32	83.2	103.1	31.2	3.2

dosimeters and Direct radon/thoron progeny sensors (DRPS/DTPS). In every village 5-6 different types of houses were selected according to their construction material and ventilation conditions. The observed

concentration values of each village of Hamirpur district are represented in Table 1. The indoor radon concentrations in these dwellings have been found vary from 22 to 573 Bq/m^3, with average value of 113.4 Bq/m^3 and thoron concentration vary from 10 to 739 Bq/m^3, with average value of 116.1 Bq/m^3.

At few dwellings in villages Chakrauli, Romera and Galote show slightly high values of radon and thoron concentration, this may be due to the difference in construction material of houses and ventilation conditions. The progeny concentrations of radon and thoron are found within the limits of 8 to 141 Bq/m^3 and 0.5 to 15.2 Bq/m^3 respectively, with average values 36.9 Bq/m^3 and 3.2 Bq/m^3 respectively. It can be observed from Table 1, that the average values of indoor radon, thoron and their progeny concentrations are lies within the safe limits as recommended by UNSCEAR and ICRP i.e. 200-600 Bq/m^3 [15,16]. The Variation in concentration values at different locations may be due to uranium concentrations in the soil of the area [17], building materials used during construction of houses, ventilation condition of the dwellings, temperature and pressure.

According to the type of construction material and ventilation rate, we have divided the houses in two categories. The mud houses, earthen flooring and poor ventilation conditions considered in type A while concrete/brick houses, concrete floor and roof and good ventilated dwellings consider in type B. The average concentrations of radon, thoron and daughter products in both types of dwellings are represented in Table 2. The average concentration values in A type houses are higher as compared to B type. The higher values in A type dwellings is due to ground floor directly constructed on top soil allows more radon/thoron to diffuse inside the house because of higher porosity of mud floor and walls. Also poor ventilation condition accumulate higher levels of radon/thoron inside the dwellings, results in high values of radon, thoron and their progeny concentrations as compared to B type dwellings.

V. Conclusion

The indoor radon, thoron and their progeny concentrations have been determined from selected locations in Hamirpur district Himachal Pradesh and found that average values of radon and thoron are 113.48 and 116.17

(Bq/m^3) respectively and radon and thoron progeny levels are 36.97 and 3.19 (Bq/m^3) respectively, which lies within the safe limits as recommended by International Commission on Radiological Protection (ICRP) and UNSCEAR. Also found that concentration levels in mud houses or in poor ventilation conditions is higher as compared to concrete houses or well ventilated.

VI. Acknowledgement

We are thankful to the Board of Research in Nuclear Sciences (BRNS), Department of Atomic Energy (DAE), Government of India, for providing financial assistance and also grateful to the residents of Himachal Pradesh for their cooperation and help for placing dosimeters in respective dwellings.

VII. References

[1] UNSCEAR, United Nation Scientific Committee on the Effect of Atomic Radiation (UNSCEAR) "Sources, effects and risks of ionizing radiation" Report to the General Assembly, United Nations, New York, 1988.

[2] BEIR, Committee on the Biological Effect of Ionizing Radiations (BEIR-V) "National Research Council" National Academy Press, Washington DC, 1990.

[3] Ramola, R.C., Prasad, G., Gusain, G.S., Rautela, B.S., Choubey, V.M., Sagar, D.V., Tokonami, S., Sorimachi, A., Sahoo, S.K., Janik, M. and Ishikawa, T. "Preliminary indoor thoron measurements in high radiation background area of southeastern coastal Orissa, India". Radiat. Prot. Dosim. 141(4) (2010) 379-382.

[4] BEIR, Committee on the Biological Effect of Ionizing Radiations (BEIR-VI) "National Research Council" National Academy Press, Washington DC, 1999.

[5] ICRP, International Commission on Radiological Protection, ICRP Publication-32, Pergamon Press, Oxford, 1981.

[6] UNSCEAR, United Nation Scientific Committee on the Effect of Atomic Radiation (UNSCEAR), United Nations, New York, 2000.

[7] Ramachandran, T.V. and Sahoo, B.K. "Thoron in the indoor environment and work places". Indian J. Phys. 83(8), (2009) 1079-1098.

[8] Ramola, R.C., Choubey, V.M., Negi, M.S., Prasad, Y. and Prasad, G. "Radon occurrence in soil-gas and ground water around an active landslide". Radiat. Meas. 43(1), (2008) 98-101.

[9] Bajwa, B.S., Virk, H.S. and Singh, S. "A comparative study of indoor radon level measurements in the dwellings of Punjab and Himachal Pradesh, India". Radiat. Meas. 36, (2003) 457-460.

[10] Singh, S., Kumar, A. and Singh, B. "Radon level in dwellings and its correlation with uranium and radium content in some areas of Himachal Pradesh, India". Environ. Int. 28, (2002) 97-101.

[11] Abu-Jarad, F. and Fremlin, J. H. "Effect of internal wall covers on radon emanation inside houses". Health Phys. 44(3) (1983) 243-248.

[12] Sahoo, B.K., Sapra, B.K., Kanse, S.D., Gaware, J.J. and Mayya, Y.S. "A new pin hole discriminated 222Rn/220Rn passive measurement device with single entry face". Radiat. Meas. 58 (2013) 52-60.

[13] Mishra, R., Prajith, R., Sapra, B.K. and Mayya, Y.S. "Response of direct thoron progeny sensors (DTPS) to various aerosol concentrations and ventilation rates". Nucl. Instrum. Meth. B 268 (2010) 671-675.

[14] Mishra, R. and Mayya, Y.S. "Study of a deposition-based direct thoron progeny sensor (DTPS) technique for estimating equilibrium equivalent thoron concentration (EETC) in indoor environment". Radiat. Meas. 43 (2008) 1408-1416.

[15] United Nation Scientific Committee on the Effect of Atomic Radiation (UNSCEAR). "Sources and effects of ionizing radiation". United Nations (2008).

[16] International Commission on Radiological Protection. "Lung cancer risk from radon and progeny". ICRP Publication-115 Pergamon Press Oxford (2011).

[17] Virk, H.S., Sharma, N. and Bajwa, B.S. "Environmental radioactivity: a case study in Himachal Pradesh, India". J. Environ. Radioact. 45 (1999) 119-127.

Curr. Rep. Sci. & Tech. 1 (2) (2015) 78-84

Dynamics of Odd Mass Lighter Compound System at Different Excitation Energies

BirBikram Singh and Manpreet Kaur
Dept. of Physics, Sri Guru Granth Sahib World University, Fatehgarh Sahib (India)
birbikram.singh@gmail.com

Abstract

The binary symmetric decay (BSD) of 21Ne formed in 10B+11B reactions at excitation energies ECN*= 45.30 and 51.59 MeV has been studied using Dynamical Cluster decay model (DCM) of Gupta and collaborators. It is relevant to mention here that we studied the system at ECN*= 51.59 MeV earlier with the results that fusion-fission (ff) decay has competition from deep inelastic orbiting (DIO). For the present study, we have compared the results with the improved experimental data at the ECN*= 51.59 MeV along with the extension of the study for another excitation energy ECN*= 45.30 MeV. We find that fragmentation potential structure does not change much at these two excitation energies except for the light particles LPs (A≤ 4), seem to be out of favor further at the higher excitation energy, the fact also reflects in the plot of preformation probability profile of the outgoing fragments. Moreover, penetrability at the respective critical angular momentum values ℓc =14 hand 16 hrespectively for ECN*= 45.30 MeV and 51.59 MeV reveals that penetration of the BSD increases at higher energies. The results further show that ff cross-section (σff) contribution for BSD increases from lower to higher excitation energy along with proportionate increase in the DIO cross-section (σDIO) for the same. Interestingly, study also indicates that DIO process, with small neck length parameter ΔR value, gets slower at the higher excitation energy. The calculations are in good comparison with the experimental data.*

Keywords
Fusion-fission, Deep inelastic orbiting

I. Introduction

In light heavy ion induced reactions, the observation of fusion-fission (ff) contrary to predictions of rotating liquid drop model offers the interesting feature to explore the reaction dynamics of light and extremely light mass compound systems formed at low energies [1]. The observed

fully energy damped binary yields have been proposed to resulting either from breakup of orbiting dinuclear system or/and fission of compound nucleus. The decay of light (ACN~30) and extremely light mass composite systems (ACN~20) have been explored within framework of dynamical cluster decay model (DCM) [2,3]. In DCM, the decay of an excited CN is studied as a collective clusterization process for emissions of the light particles LPs ($A \leq 4$), as well asthe intermediate mass fragments (IMFs) and ff, in contrast to the statistical models in which each type of emission is treated on different footing. In recent work [4], we studied the role of deformation and orientation of nuclei in the binary symmetric decay of 21Ne* formed in 10B+11B reactions at ECN*=51.59 MeV in comparison with spherical consideration of nuclei as per availability of data in [5].

In the present work, we extend the study of BSD of extremely light mass compound system 21Ne* at excitation energies E*CN= 45.30 and 51.59 MeV, to see the role of different excitation energies in the decay of lighter mass compound system, as the data for the improved experimental study is also available [6]. The present study shows the occurrence of ff having competition fromdeep inelastic orbiting (DIO), as also observed in previous work [4]. We find that there is not much change in fragmentation structure at these two different excitation energies except that the LPs are further out of favor at higher excitation energy. In preformation profile also, the same observation is reflected. With increase in excitation energy, the penetration probability increases from ECN* = 45.30 to 51.59 MeV for the BSD of 21Ne*. Moreover, it is observed that the value of ΔR for ff is same at both the excitation energies while the (σff) contribution for BSD increases from lower to higher excitation energy along with proportionate increase in the DIO cross-section (σDIO) for the same. The methodology adopted for the study is given in section II. The calculations, results and their comparison with the experimental data [6] are presented in section III and thework is concluded in section IV.

II. Methodology: Dynamical Cluster Decay Model

In the present study, the decay of hot and rotating compound system formed in heavy ion reaction is studied within the framework of dynamical cluster decay model (DCM) of Gupta and collaborators [2,3]. DCM, based on quantum mechanical fragmentation theory (QMFT), is worked out in theterms of collective coordinates of mass asymmetry $\eta = (A_1 - A_2)/(A_1 + A_2)$, relative separation R, quadrupole deformations β_{2i}(i=1,2) and orientations $\theta_i$of two fragments. In terms of thesecoordinates, the DCM defines the decay cross-section, in termsof ℓ partial waves, as

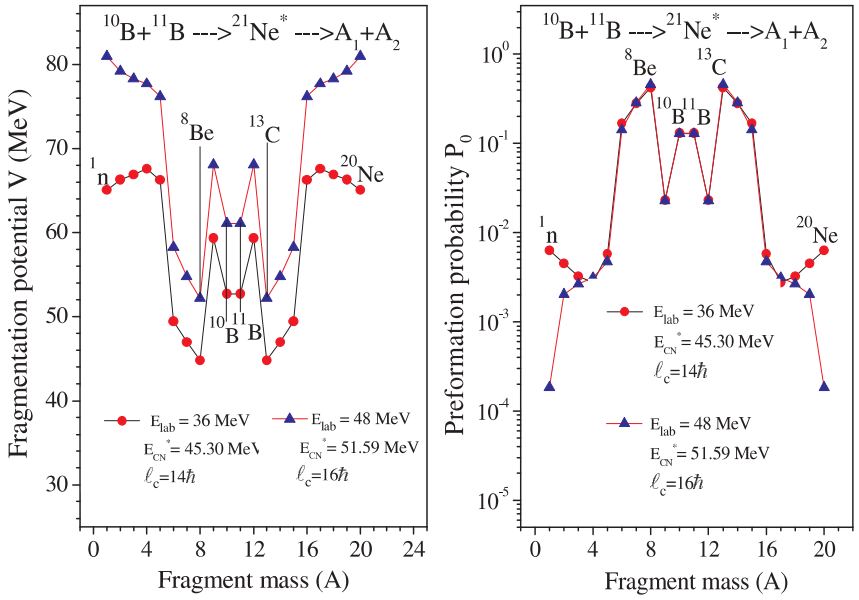

Fig. 1. *Fragmentation potential as a function of fragment mass A for the decay of $^{21}Ne^{*}$ at ℓ_c values for E_{lab} = 36 and 48 MeV, with quadrupole deformations and compact orientations included.*

Fig. 2. *Preformation probability P_0 as a function of fragment mass A for the decay of $^{21}Ne^{*}$ at ℓ_c values for E_{lab} = 36 and 48 MeV, with quadrupole deformations and compact orientations included.*

$$\sigma = \frac{\pi}{k^2}\sum_{l=0}^{l_{max}}(2l+1)P_0P; k = \sqrt{\frac{2\mu E_{c.m.}}{\hbar^2}} \quad (1)$$

where ℓ_c is the critical angular momentum value, in terms of the bombarding energy $E_{c.m.}$, the reduced mass $\mu=[A_1A_2/(A_1+A_2)]_m$ and the first turning point R_a of the entrance channel η_{in}, given by

$$\ell_c = R_a\sqrt{2\mu[E_{c.m.} - V(R_a, \eta_{in}, \ell = 0)]}/\hbar$$

The preformation probability (P_0) in eq. (1) given as

$$P_0 = |\psi_R(\eta(A_i))|^2 \sqrt{B_{\eta\eta}}\frac{2}{A_{CN}} \quad (2)$$

refers to motion and is obtained by the solution of Schrödinger equation in, at a fixed R=R_a

$$\left\{-\frac{\hbar^2}{2\sqrt{B_{\eta\eta}}}\frac{\partial}{\partial\eta}\frac{1}{\sqrt{B_{\eta\eta}}}\frac{\partial}{\partial\eta}+V_R(\eta,T)\right\}\psi^v(\eta)=E^v\psi^v(\eta) \quad (3)$$

with $v = 0, 1, 2, 3...$ referring to ground-state ($v = 0$) and excited states solutions. The mass parameter $B_{\eta\eta}$ are the smooth classical hydrodynamical masses [7].

The tunneling probability P in eq. (1), for each η, is calculated as the WKB integral

$$P = \exp\left[-\frac{2}{\hbar} \int_{R_a}^{R_b} \{ 2\mu [V(R) - Q_{eff}] \}^{1/2} dR \right] \quad (4)$$

with R_a and R_b as the first and second turning points. Q_{eff} is the Q-value of the decay process and the first turning point $R_a(T) = R_1(\alpha_1, T) + R_2(\alpha_2, T) + \Delta R(T)$, where $R_i(\alpha_i,) = R_{0i}(T)\,[1 + \sum \beta_{\lambda i} Y_\lambda^{(0)}(\alpha_i)] R_i(\alpha_i)]$ and $R_{0i}(T) = [1.28A^{1/3}_i - 0.76 + 0.8A^{1/3}_i][1 + 0.0007T^2]$.

The fragmentation potential $V(R, \eta, \beta_{\lambda i}, \theta_i, T)$ is the sum of liquid drop energy V_{LDM}, shell corrections δU, Coulomb potential V_c, nuclear proximity V_p and angular momentum dependent potentials $V_{\ell,}$ given as:

$$V_R(\eta,T) = \sum_{i=1}^{2}[V_{LDM}(A_i,Z_i,T)] + \sum_{i=1}^{2}[\delta U_i]\exp(-T^2/T_0^2) + V_c(R,Z_i,\beta_{\lambda i},\theta_i,T) + V_p(R,A_i,\beta_{\lambda i},\theta_i,T) + V_\ell(R,A_i,\beta_{\lambda i},\theta_i,T) \quad (5)$$

The contribution of non-CN DIO process in $\sigma_{BSD}(\sigma_{ff}+\sigma_{DIO})$ is calculated by considering preformation probability $P_0=1$ for the entrance channel, i.e. the target and projectile considered not to lose their identity, and penetrability P calculated for the incoming channel. The contributions σ_{ff} and σ_{DIO} (using equation. (1)) in total σ_{BSD} are calculated for the best fit of the only parameter, the neck length parameter ΔR.

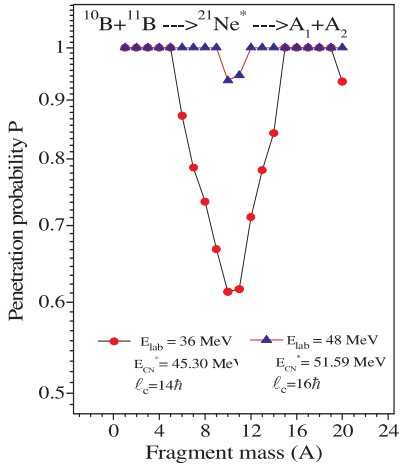

Fig. 3. *Penetration probability P as a function of fragment mass A for the decay of $^{21}Ne^*$ at ℓ_c values for E_{lab} = 36 and 48 MeV.*

III. Calculation and Discussion

The Fig.1 shows the fragmentation potential V (MeV) as a function of fragment mass A for thedecay of $^{21}Ne^{*}$ at E_{lab} = 36 and 48 MeV. Here we observe that at E_{lab}= 48 MeV, the LPs are more out of favor as compared to at E_{lab}=36 MeV. The BSD fragments ^{10}B and ^{11}B are favored having competition from ^{8}Be and ^{13}C at both the excitation energies. Moreover, the potential energy surface for the IMFs does not change at all for both the energies. Fig.2 further reflects the fact which presents the preformation probability P_0 as function of fragment mass (A) for the decay of $^{21}Ne^{*}$. One clearly observes that there is no significant change in the preformation profile with increase in energy specifically for the IMFs whereas for the LPs preformation probability P_0 decreases further athigher excitation energy. It is important to note here that since the nuclear structure effects enters the DCM via P_0, it is evident that with increase in energy there isno significant change in nuclear structure effects takes place with change in excitation energy. Fig. 3 shows variation of penetration probability as a function of A, through the interaction barrier. One observe that with increase in energy the penetration probability P of fragments increases and approaches the maximum value of 1 at the irrespective $\ell_c$values. It is the increase in angular momentum dependent energy due to which penetrability of fragments increases and leads to enhancement in total cross-section for BSD as shown in Table 1. The table presents that with increase in excitation energy, the value of ΔR is same while the σ_{ff} contribution for BSD increases along with proportionate increase in σ_{DIO}. The value of ΔR decreases.

IV. Conclusion

The BSD of odd mass lighter compound system $^{21}Ne^{*}$ has been studied at excitation energies E_{CN}^{*}= 45.30 and 51.59 MeV within the collective clusterization framework of DCM. The study shows that ff and DIO are in competition for the decay of $^{21}Ne^{*}$. With increase in excitation energy, there is no significant change in fragmentation and preformation structure while the penetrability of BSD fragments increases with increase in excitation energy. The calculated BSD cross sections shows that with increase in excitation energy, the σ_{ff}contribution for BSD increases along with proportionate increase in the DIO cross-section (σ_{DIO}) for the same. It seems that DIO process getss lower at higher excitation energy evidently with

small value of ΔR. The calculated total BSD cross-sections are in good agreement with experimental data [6]. It is relevant to mention here that the data for other two neighboring lighter compound systems $^{20,22}Ne^{*}$ is available at different excitation energies [6] and the results from the present study motivate us to further explore the dynamics of these nuclei formed in light heavy ion reactions.

V. Acknowledgment

B.B.S. acknowledges the support from Department of Science and Technology (DST), New Delhi, in theform of a Young Scientist Award under the SERC Fast Track Scheme, vide letter No. SR/FTP/PS-013/2011.

VI. References

[1] S.J. Sanders, "Fusion-fission in nuclear systems with $40 \leq A_{CN} \leq 80$"*Phys. Rev. C*44 (1991) 2676; R.M. Anjos, N. Added, N. Carlin, L. Fant Jr., M.C.S. Figueira,"Fission decay of very light nuclear systems" *Phys. Rev. C* 48(1993) *R2154, ibid* "Competing reaction mechanisms for the $^{16,17,18}O+^{10,11}B$ and $^{19}F+^{9}B$esystems" *Phys. Rev. C* 49(1994) 2018;C. Beck and A. Szanto de Toledo, "Macroscopic features of light heavy-ion fission reactions" *Phys. Rev. C* 53(1996) 1989.

[2] R. K. Gupta, R. Kumar, N. K. Dhiman, M. Balasubramaniam, W. Scheid, "Cluster decay of hot $^{56}Ni^{*}$ formed in the $^{32}S+^{24}Mg$ reaction" *Phys. Rev. C* 68(2003) 014610; B. B. Singh, M. K. Sharma, R. K. Gupta, W. Greiner,"Entrance channel effects in the dynamical cluster decay model for the decay of hot and rotating compound nucleus $^{48}Cr^{*}$ at $E_{CN}^{*} = 60$ MeV" *Int. Jour. Mod. Phys. E* 15 (2006) 699; B. B. Singh, M.K. Sharma, R. K. Gupta, "Decay of $^{246}Bk^{*}$ formed in similar entrance channel reactions of $^{11}B+^{235}U$ and $^{14}N+^{232}Th$ at low energies using the dynamical cluster-decay model" *Phys. Rev. C* 77 (2008) 054613.

[3] B. B. Singh, G. Kaur, M. K. Sharma, R. K. Gupta, "Fusion-fission of very light mass compound nucleus $^{28}Al^{*}$ using the dynamical cluster decay model"*Proc. DAE Symp. on Nuc. Phys.* 56 (2011) 474; 57

(2012) 550; B. B.Singh, M. Kaur, V. Kaur, R. K. Gupta, "Nuclear structure effects in fusion-fission of compound systems $^{20,21,22}Ne^{*}$ formed in $^{10,11}B+^{10,11}B$ reactions" *Proc. Conf. on 75 years of Nuclear Fission* (2014) 51.

[4] B. B. Singh, M. Kaur, R.K. Gupta, "Deformation and orientation effects in the binary symmetric decay of $^{20,21,22}Ne^{*}$"*Proc. DAE Symp. on Nuc. Phys* .59(2014) 516; ibid "Heavy ion collision dynamics of $^{10,11}B+^{10,11}B$ reactions" *Eur.Phys. J. Web of Conferences* 86 (2015) 00048; ibid "Fusion fission of extremely light mass compound systems $^{20,21,22}Ne^{*}$"*J. of Phys. Conf. Series* 6 (2015)030001.

[5] A. Szanto de Toledo, M. M. Coimbra, N. Added, R. M. Anjos, N. Carlin Filho,"Fissionlike Decay of ^{20}Ne: Eccentric behavior in the B+B fusion processes"*Phys. Rev. Lett.* 62(1989) 1255.

[6] M.M. Coimbra, R. M. Anjos, N. Added, N. Carlin Filho, L. Fant Jr. et al., "Study of $^{10,11}B+^{10,11}B$ reactions upto E/A =5 MeV"*Nucl. Phys. A* 535(1991) 161.

[7] H. Kroger and W. Scheid, "Classical models for the mass transfer in heavy ion collisions"*Jour. of Phys. G* 6(1980) L85.

Curr. Rep. Sci. & Tech. 1 (2) (2015) 85-92

Effect of orientations in the decay of very light mass compound nucleus $^{28}Al^{*}$ formed in $^{18}O+^{10}B$ and $^{19}F+^{9}Be$ reactions

BirBikram Singh[a], MandeepKaur[a], and Manoj K. Sharma[b]
[a]Dept. of Physics, Sri Guru Granth Sahib World University, Fatehgarh Sahib (India)
[b]School of Physics & Material Sciences, Thapar University, Patiala (India)
birbikram.singh@gmail.com

Abstract

The yields of evaporation residues (ERs)/light particles (LPs) and fusion-fission (ff) fragments in $^{18}O+^{10}B$ and $^{19}F+^{9}Be$ reactions, forming compound system $^{28}Al^{*}$ at E_{lab}=56 MeV, are analysed within the framework of well known Dynamical Cluster Decay Model (DCM) in reference to the available experimental data. The experimental data is available for ERs and ff fragments with charge distributions (Z) from the equilibrated compound nucleus $^{28}Al^{*}$. The quadruple deformations (β_2) and compact orientations are included for the analysis, within the DCM approach of collective clusterization process. The light particles (LPs) are shown to have different characteristics than that of intermediate mass fragments (IMFs) as observed also in earlier studies but with spherical considerations. Interestingly we find that the results remain invariant with the inclusion of orientation effects, with the only difference of large values of ΔR.The entrance channel independence is also observed in the decay of $^{28}Al^{*}$ formed due to different target projectile combinations, as the excitation energy E^{*}_{CN} for both the cases is approximately chosen to be 45 MeV for the present study.

Keywords

Evaporation residues, Fusion-fission, Intermediate mass fragments

I. Introduction

In recent times, many exotic experiments and advanced theoretical

developments have enabled us to study the nuclear behavior in different ways including the understanding off ormation and decay of nuclear systems. The decay of hot and rotating nuclei formed in heavy ion reactions provide a interesting platform to study the nuclear properties. The target or projectile deformations are explained to play a significantrole in the determination of fusion cross-section. These studies help us to carry out comprehensive analysis of reaction dynamics along with relevant information about the nuclearstructure and associated properties [1-2]. Low energyheavy ion collisions (E/A≤15MeV) present opportunity to study the nuclear structure as well as the collective behaviour of nucleons with binding energies, temperature, Coulomb potential, nuclear potential and angular momentum potential playing significant role in the reaction dynamics during formation and decay of compound system with the deformation and orientation effects included. Compound systems formed in these reactions are highly excited and carry large angular momentum depending upon the energy in the incident channel. Depending upon the mass of the compound nuclei, various emissions like light particles LPs, intermediate mass fragments IMFs, heavy mass fragments HMFs, and fusion-fission ff possibilities may arise.

Recently, a very light mass system $^{28}Al^{*}$ formed in reaction $^{18}O + ^{10}B$ at centre of mass energy $E_{c.m}$.= 17.422 MeV [3], has been studied using Dynamical cluster model (DCM) of Gupta and collaborators [4] with the spherical consideration of outgoing nuclei. We observed that although the structure of the potential energy surface (PES) does not change ingoing from angular momentum values ℓ= 0ħ to 24ħ, but interestingly the characteristic behaviour of the LPs and IMFs is opposite to each other, as is the case with earlier studied light mass compound nuclei $^{48}Cr^{*}$[4] and $^{56}Ni^{*}$[5]. More significantly the PES does not change for the differentchoices of ΔR (neck length parameter, the only parameter of DCM) to fit the data for fragments having Z=3, 4, 5, and 6.The calculated fusion fission cross-section σ_{ff} correspondingto Z=3, 4, 5, 6 fragments for $^{18}O + ^{10}B \rightarrow ^{28}Al^{*}$ reaction compared with the experimental data [6]. The DCM based σ_{ff} find better comparison with the experimental data as compared to TSM calculations. This work was further extended for the simultaneous fitting of the data for all the fragments

and atdifferent $E_{c.m}$. Moreover, another reaction $^{17}O + ^{11}B$ forming^{28} Al^*at different $E_{c.m}$.was also studied. It was observed thatthe choice of the individual or the simultaneous fitting of the ΔR for different fragments does not affect the result too much [7].

In the present work, within the DCM approach of collective clusterization, the study of a very light mass compound system^{28} Al^*formed in $^{18}O+^{10}B$ and $^{19}F+^{9}Be$ reactions, at same excitation energy $E^*_{CN} = 45$ MeV, is further extended with deformations and orientations effects included. It is relevant tomention here that this system has been studied extensively with lot of experimental data available for entrance channels with different target projectile combinations, at different excitation energies. However, we are interested here to study the effects of deformed (quadrupole) and oriented (compact) nuclei in the reaction dynamics of $^{28}Al^*$. The entrance channel independence is also analysed in order to establish the compound nucleus formation of the system at the given energies. Moreover, angular momentum effects have also been studied extensively and the results are very well compared with the experimental data [6]. The calculations are done with the simultaneous fitting of the ΔR for different fragments.

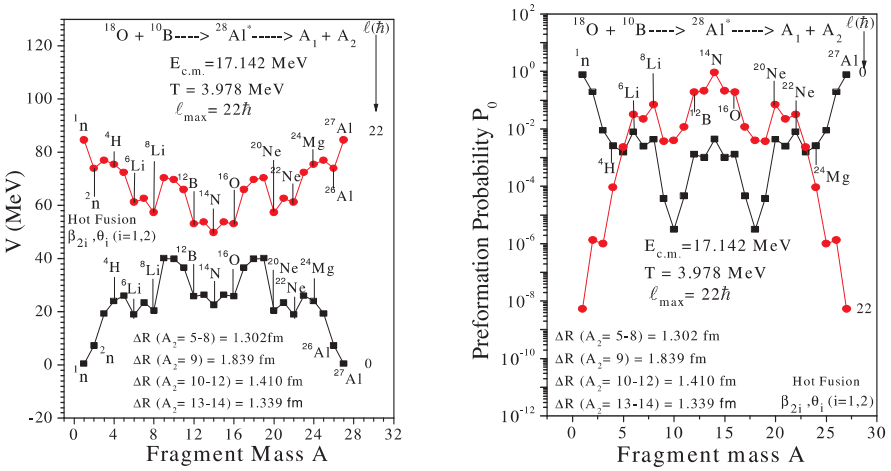

Fig. 1 (a).The fragmentation potentials V (MeV) (b). The fragment preformation factor P_0 for the decay of $^{28}Al^*$, formed in the reaction $^{18}O+^{10}B$ at centre of mass energy $E_{c.m.}$ = 17.142 MeV, to various complex fragments (both LPs and IMFs) based on DCM calculations.

We intend to investigate the effects of oriented nuclei inthe reaction dynamics of a very light mass compound nucleus $^{28}Al^{*}$ using the methodology of DCM, for which details are given in section II. The calculations and results are discussed in section III. The study is concluded in section IV.

II. Methodology: Dynamical Cluster Decay Model

Dynamical cluster decay model (DCM) is different from another statistical model as it treats the evaporation residues (ERs), intermediate mass fragments (IMFs) and fusion fission (ff) on equal footings [3].The missing nuclear structure information of compound nucleus in statistical model enters in DCM via preformation probability P0 of the fragments and is calculated by solving Schrodinger equation in η co-ordinate. For ℓ-partial waves, the compound nucleus decay cross-section is given by

$$\sigma = \frac{\pi}{k^2} \sum_{l=0}^{l_c orl_{\max}} (2l+1) P_0 P \qquad k = \sqrt{\frac{2\mu E_{c.m}}{\hbar^2}} \qquad (1)$$

where, $\mu = [A_1A_2/(A_1 + A_2)]m$, is the reduced mass, with m as the nucleon mass and ℓ_{maxis} the maximum angular momentum. The angular momentum ℓ_{max} is fixed for vanishing the fusion barrier of incoming channel η ior light particles cross-section σ_{LP}. The total fusion cross-section within this model is given by

$$\sigma_{fus} = \sigma_{ER} + \sigma_{ff} + \sigma_{nCN} \qquad (2)$$

where σ_{ER}, σ_{ff} and σ_{nCN} are respectively evaporation residue/ LPs, ff and non-compound nucleus cross sections which sum up to give fusion cross section σfus. Apparently, in the DCM, both LPs and complex IMFs up to symmetric division are treated as the dynamical collective mass motions of preformed clusters or fragments through the barrier. In Eq. (1), the preformation probability P_0 is obtained by solving the stationary Schrodinger equation in η, at a fixed $R = R_a$, and is given by

$$P_0 = \sqrt{B_{\eta\eta}} \left|\psi[\eta(A_i)]\right|^2 (2/A) \qquad (3)$$

The structure information of the compound nucleus enters the preformation probability P0 through the fragmentation potential V (R, η, βλi, θi, T), defined as

$$V(\eta, R, \ell, T) = \sum_{i=1}^{2}[V_{LDM}(A_i,Z_i,T) + \sum_{i=1}^{2}[\delta U_i]e^{\left(\frac{-T^2}{T^2}\right)} + V_c(R,Z_i,\beta_{\lambda i},\theta_i,T) + V_p(R,A_i,\beta_{\lambda i},\theta_i,T) + V_\ell(R,A_i,\beta_{\lambda i},\theta_i,T)] \quad (4)$$

Here V_{LDM} and δU are, respectively, the T-dependent liquid drop and shell correctionenergies [4], V_c is the coloumb potential, V_p indicates the proximity potential and V_ℓ denotes the angular momentum dependent potential.

The penetrability calculated as the WKB tunneling probability

$$P = \exp[-\frac{2}{\hbar}\int_{R_a}^{R_b}\{2\mu[V(R) - Q_{eff}]\}^{1/2}dR] \quad (5)$$

R_a, defined above, is the first turning point of the penetration path used for calculating the WKB penetrability P.

III. Calculations And Discussions

We have presented the systematic study of the decay of $^{28}Al^*$ formed in $^{18}O + ^{10}B$ and $^{19}F + ^{9}Be$ reactions at excitation energy E^*_{CN} =45 MeV only. For this system, the relative cross-section of ERs/ LPs ($A \leq 4$ and $Z \leq 2$) and for IMFs ($5 \leq A \leq 20$ and $3 \leq Z \leq 10$) are observed. The calculations are done to predict the behavior of relative crosssections for Z=3, 4, 5 and 6 and have compared them with the experimental data [6]. Entrance channel independence is also looked into for the system.

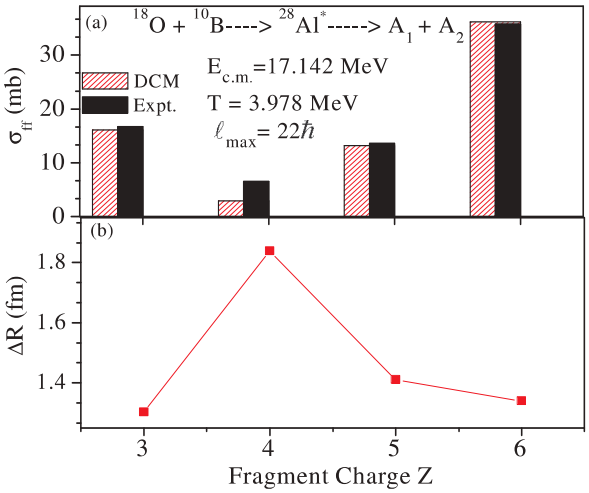

Fig. 2. The DCM calculated (a) fusion-fission cross-sections σ_{ff} for Z=3,4,5 and 6, compared with the experimental data [7] and (b) the simultaneously fitted ΔR values, in the decay of $^{28}Al^*$ formed in $^{18}O+^{10}B$ reaction at excitation energy E^*_{CN}=45MeV

The calculations for the decay of $^{28}Al^{*}$ at E^{*}_{CN} =45 MeV using DCM with deformations and orientations (hot/compact) included are discussed. We calculate the contribution of σ_{ff} in the decay within the dynamical collective clusterisation process. In DCM there isonly one parameter, neck length parameter ΔR, which isrelated to reaction time. More is the value of ΔR means relative separation is more between two nuclei, more fast is the process of fission or emission, so the reaction time is small.The calculated fragmentation potential for the decay of $^{28}Al^{*}$ into various mass fragments (LPs and IMFs) at two extreme ℓ-values, shown in Fig. 1(a).Although the structure of the potential energy surface (PES) does not change ingoing from ℓ= 0ħ to the ℓ_{max}. But the characteristic behaviour of the LPs and IMFs is opposite to each other. In other words at lower ℓ-values, the LPs are energetically more favourable (lower in energy), whereas the same is trueof IMFs at higher ℓ-value. If we compare the *result with that of previous studies [3-7] in which we have done the calculation by spherical consideration, there is no differencein the characteristic behaviour of LPs and IMFs, the only difference is of Δ*R values, which are more for the oriented nuclei. Fig. 1(b) shows the collective preformation profile for the all possible fragments, the fragments having lowest fragmentation potential are highly preformed. LPs are highly preformed at lower ℓ-values, but IMFs start contributing at higher ℓ-values. We see that ^{14}N has higher preformation probability as compared to its neighbors ^{12}C and ^{16}O. So the Possibility of decay of ^{28}Al into ^{14}N and its complementary fragment ^{14}C is more. Fig. 2 (a) presents the DCM calculated σ_{ff} for Z=3, 4, 5 and 6 fragments, compared nicely the same with the experimental data. Moreover, the simultaneously fitted values of ΔR are also plotted as a function of fragment charge Z. We see that the ΔR value for Be is large in comparison tothe neighboring fragments, indicating its fastest decay.

Table. 1 shows the comparison of results for both the reaction channels $^{18}O+^{10}B$ and $^{19}F+^{9}Be$ at E^{*}_{CN}=45 MeV. The calculated σ_{ff}, *within DCM, have good comparison with experimental data at the same values of Δ*R for both the entrance channels. This means that both the reactions occur at similar time scale. Moreover, it establishes that very light mass compound system $^{28}Al^{*}$ formation is not depending on the incoming

channels, in line with the Bohr's hypothesis of entrance channel independence of the compound nucleus. It is relevant to mention here that earlier we have carried out this type of investigation for the light mass compound systems $^{47}V^{*}$[8] and $^{48}Cr^{*}$[5], but with spherical considerations of the nuclei. Here, we have studied the entrance channel independence in the decay of further lighter mass compound nucleus $^{28}Al^{*}$, with deformation and orientation effects included. Also, we have predicted here the LPs/ EVRs cross section σ_{evrs}, not availablefor the decay of $^{28}Al^{*}$formed inanother reaction $^{19}F+^{9}Be$.

Table I: The DCM calculated ff cross-sections $_{ff}$for Z=3,4,5 and 6 and EVRs (LPs) cross section σ_{evr} in the decay of $^{28}Al^{*}$formed in $O+^{10}B$ and $^{19}F+^{9}Be$ reactions at same excitation energy E^{*}_{CN} = 45 MeV, compared with the experimental data [7].

Reaction	$E_{c.m.}$ (MeV)	E^{*}_{CN} (MeV)	T(MeV)	$\ell_{max}(\hbar)$	Z	ΔR	σ_{ff} (mb)	
							DCM	Expt
$^{18}O+^{10}B$	17.142	45.261	3.978	22	3	1.302	16.52	16.77
					4	1.839	2.998	5.95
					5	1.410	13.54	13.60
					6	1.339	36.14	35.75
					LPs	1.878	855	854.92
$^{19}F+^{9}Be$	18.000	44.731	3.956	22	3	1.302	16.15	16.77
					4	1.839	2.94	6.59
					5	1.410	13.215	13.69
					6	1.339	35.62	37.71
					LPs	1.878	852.7	-

IV. Conclusion

The DCM calculated ff cross-section σ_{ff}corresponding to Z=3, 4, 5, 6 fragments and LPs/ ERs cross section σ_{evr}, in the decay of $^{28}Al^{*}$ formed in $^{18}O+^{10}B$ and $^{19}F+^{9}Be$ reactions at $E^{*}_{CN}\leq$ 45 MeV, with deformation and orientation effects included, are compared with the experimental data [6]. However, we have predicted σ_{evr} value for the $^{19}F+^{9}Be$ reaction channel, as experimental data is not available for the same. The inculcation of deformations (upto $\square_2$) and compact orientations for the available data of ff fragments for Z=3, 5, 6 and ERs/ LPs fitted nicely. The study reveals that orientation effects do not alter the results in comparison to the spherical considerations except that the ΔR values are more for the later case.

Moreover, the results for both the reaction channels $^{18}O+^{10}B$, $^{19}F+^{9}Be$ forming $^{28}Al^{*}$at same E^{*}_{CN} = 45 MeV shows that the decay of the same is independent of the entrance channel conforming Bohar's hypothesis.

V. References

[1] R. Beringer., "Coloumb distortions in heavy ion reactions" Phys. Rev. Lett. 18 (1967) 1006.

[2] C. Y. Wong., "Interaction barrier in charge particle nuclear reactions" *Phys. Rev. Lett.* 31(1973) 766.

[3] BirBikram Singh, Gurvinder Kaur Manoj K. Sharma and Raj K. Gupta., "Fusion fission of very light mass compound nucleus $^{28}Al^{*}$ using dynamical cluster decay model" Proc. DAE Symp.on *Nuc. Phys.* 56(2011) 474.

[4] Raj K. Gupta, M. Balasubarmaniam, Rajesh Kumar, Dalip Singh, C. Beck and Walter Griener., Cluster decay of hot $^{56}Ni^{*}$ formed in ^{32}S + ^{24}Mg reaction *Phys. Rev.* C 68 (2003)014610; "Collective Clusterization in Hot and Rotating Nuclei: Preformed-cluster based Dynamical Cluster-decay Model" *IREPHY* 2(2008) 369.

[5] BirBikram Singh, Manoj K Sharma, Raj K. Gupta and Walter Griener.,"Entrance channel effects in the dynamical cluster decay model for the decay of hot and rotating compound nucleus $^{48}Cr^{*}$ at E_{CN}^{*}=60 MeV" Int. J. of Mod. Phy. E 15(2006) 699.

[6] R. M. Anjos, et al., "Competing reaction mechanisms for the1 $^{16,18,17}O$ + $^{10,11}B$ and 19F+9Be reactions" *Phys. Rev.* C 48 (1993) R2154.

[7] BirBikram Singh, Gurvinder Kaur, Manoj K. Sharma and Raj K. Gupta., "Fusion of compound nucleus $^{28}Al^{*}$ formed in $^{18,17}O+$ $^{10,11}B$ reactions using dynamical cluster decay model" Proc. DAE Symp. on Nuc. Phys. 57 (2012) 550.

[8] BirBikram Singh, Pawan Kumar, Shefali Kanwar and Raj K. Gupta., "Entrance channel independence the the decay of $^{47}V^{*}$formed in nearly symmetric and asymmetric reactions" Proc. DAE Symp. on Nuc. Phys. 58(2013)382.

Curr. Rep. Sci. & Tech. 1 (2) (2015) 93-111

Synthesis and Biological Activities of 1,3,5-Trisubstituted Pyrazolines

M. S. Batra,[a] Amandeep Singh,[b] Sujita Thakur[a] and Hardeep Kaur[a]
[a]Post Graduate Department of Chemistry, Khalsa College Amritsar (India)
[b]Pharmacognosy and Phytochemistry Laboratory, Khalsa College of Pharmacy, Amritsar (India)
msbatra_99@yahoo.com

Abstract

Pyrazoline derivatives have broad range of biological activities. The chalcone motif serve as the important intermediate for the synthesis of the biologically active 1,3,5-trisubstituted pyrazolines. The variation of the substitutents around the pyrazoline core results in the novel class of pyrazolines having improved biological profile. In this review, we have compiled the synthesis and biological profiles of variety of trisubstituted pyrazolines synthesized from chalcones.

Keywords

Chalcones, trisubstituted pyrazoline, biological activity, heterocyclic compounds.

I. Introduction

Pyrazolines are the important and well known nitrogen containing five membered heterocyclic compounds. Pyrazolines are weakly basic and chemically, these are considered as partially reduced form of the pyrazole. Pyrazoline exist in three isomeric forms *i.e.* 1-pyrazoline (**1**), 2-pyrazoline (**2**) and 3-pyrazoline (**3**). These three forms exist in equilibrium with one another other which differ in position of double bond (Figure 1). The 2-

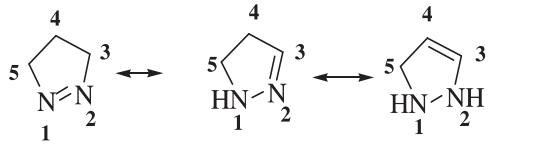

1 **2** **3**

Fig 1. *Structure of pyrazoline.*

pyrazoline exhibits the monoimino character and hence it is more stable than the 1- and 3-pyrazoline. Pyrazoline derivatives (**1-3**) differ considerably in their properties from those of pyrazole due to their much lower stability. Pyrazolines are hydrolyzed by mineral acids and hence they resemble hydrazones.

The 2-pyrazoline ring is characterized by ^{1}H NMR spectrum [1]. The three protons in the pyrazoline ring **(2a)** show AMX splitting pattern, H_A proton appearing at δ 2.98 (dd), J_{AM}= 7.6 Hz and J_{AX} = 12 Hz, H_M proton resonating at δ 3.64 (dd), J_{AM}= 12 Hz and J_{MX}=12 Hz and H_X proton appearing at δ 5.2 (dd), J_{AX}= 7.6 Hz and J_{MX}=12 Hz.

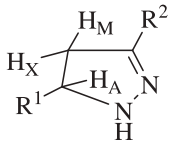

2a

The general methods for the synthesis of 2-pyrazolines (Scheme 1, route **1-6**) include the reaction of α,β-unsaturated carboxylic acid ester (**4**)/benzylideneacetone (**5**)/chalcones (**6**) with diazomethane or the reaction of α,β-unsaturated aldehydes (**7**)/mannich bases (**8**) with phenyl hydrazine or the reaction of chalcones (**9**) with hydrazine. The reaction with diazomethane results in 3,4-disubstituted pyrazolines (route 1-3). The reaction of chalcones with hydrazine (R^1 = H) results in 3,5-disubstitutedpyrazolines whereas similar reaction of chalcones with substituted hydrazines led to the 1,3,5- trisubstituted pyrazolines (route 6). Among the routes 1-6, route 6 is the most common and highly preferred method for the synthesis of 2-pyrazolines in high yield [2].

Numerous pyrazoline derivatives have been found to possess broad-spectrum of biological activities such as antibacterial [3], antifungal [4], antiinflamatory [5], analgesic [6], antioxidant [7], insecticidal [8], molluscicidal [9], antidepressant [10], antitubercular [11], anti HIV [12], antimalarial [13] and anticancer [14] activities. The most promising and notable applications of pyrazoline is the use of pyrazoline derivatives as a fluorescent brightening agent [15]. The prevalence of the pyrazoline scaffold in bioactive molecules has stimulated the research activity in this

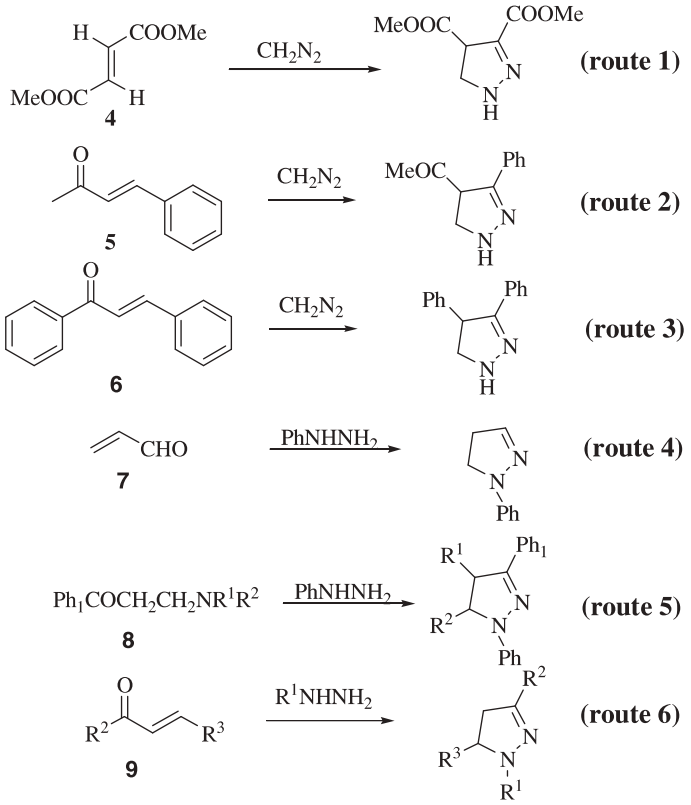

Scheme 1. *General methods of synthesis of 2-pyrazoline.*

field. Thus, we report here, the synthesis and biological evaluation of some new 1,3,5-trisubstituted pyrazoline derivatives derived from the chalcone precursor. The review is divided in two sections. First section discusses the synthesis and biological activity of 1,3,5-trisubstituted pyrazolines obtained from the aromatic chalcones whereas the second section outlines the synthetic aspects and biological activity of pyrazolines obtained from the heteroaromatic chalcones.

II. Pyrazolines Derived From Aromatic Chalcones

Sivakumar *et al* [16] prepared pyrazolines (13) from the condensation of appropriate chalcone (12) with phenylhydrazine in acetic acid (Scheme 2). The chalcones (12) were prepared from the condensation of substituted benzaldehyde and substituted acetophenone (Scheme 2) in ethanol in the

presence of sodium hydroxide. Further, the synthesized compounds were tested for antibacterial activity against six bacterial strains including Gram positive and Gram-negative, namely *S. aureus* NCIM 5021, *B. subtilis* NCIM 2718, *P. vulgaris* NCIM 2813, *E. Coli* NCIM 2931, *S. Typhi* NCIM 2501, and *P. aeruginosa* NCIM 5029 by two fold dilution assay using reaszurin as an indicator. The pyrazolines bearing chloro substitution in the A-ring (R =2/4-Cl) are most active and hence favors activity.

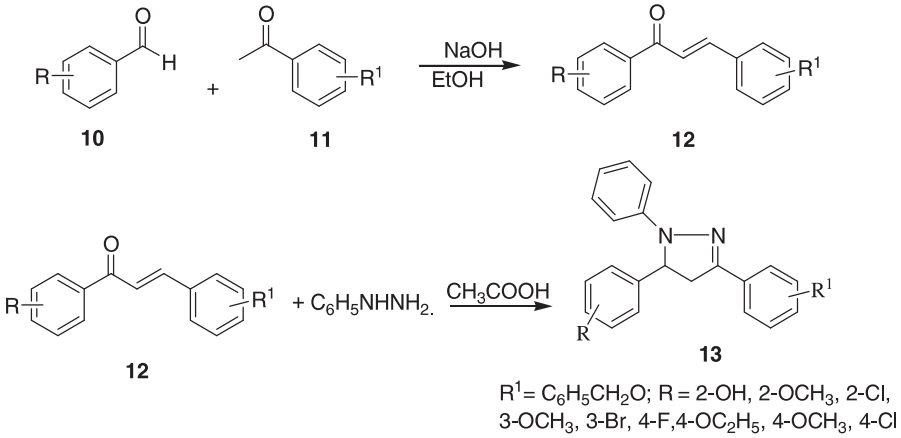

Scheme 2

Novel 2-pyrazoline derivatives **15** [17], have been synthesized by the treatment of 1- (napthyl amino)-3-aryl-2-propene-1-ones **14** with hydrazine hydrate (Scheme 3). Further these compounds were evaluated for their antibacterial activity. The acetylation of **15** in ethanol in the presence of acetic acid led to the 1-acetyl-3,5-disubstituted-pyrazolines (**16**). The compounds **15** showed good activity against gram positive and gram negative bacterial strains whereas pyrazoline **16** depicted mild antifungal activity [18].

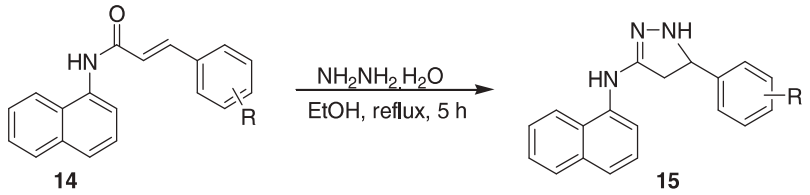

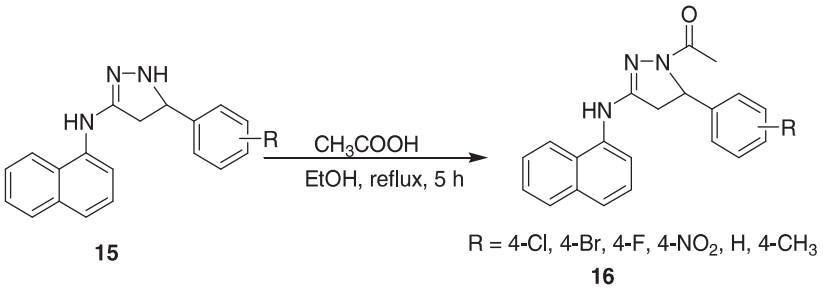

Scheme 3

Voskiene *et al* [19] synthesized a series of the pyrolidinone based pyrazoline derivatives **21-22** and pyrazole **23** from the condensation of the chalcone **20** with hydrazine or phenylhydrazine (Scheme 4). The condensation of phenylhydrazine with chalcone **20** in 1,4-dioxane yielded pyrazoline **22** whereas the same condensation in acetic acid led to the pyrazole derivative **23**. The starting product 1-(4-acetylphenyl)-4-carboxy-2-pyrrolidinone **18** was obtained by the reaction of 4-aminoacetophenone **17** with itaconic acid in water. Further, the chalcones **20** were obtained in good yields by base (NaOH) catalyzed aldol condensation of the substituted acetophenone derivative **18** and the substituted benzaldehydes (**19)** in ethanol (Scheme 4).

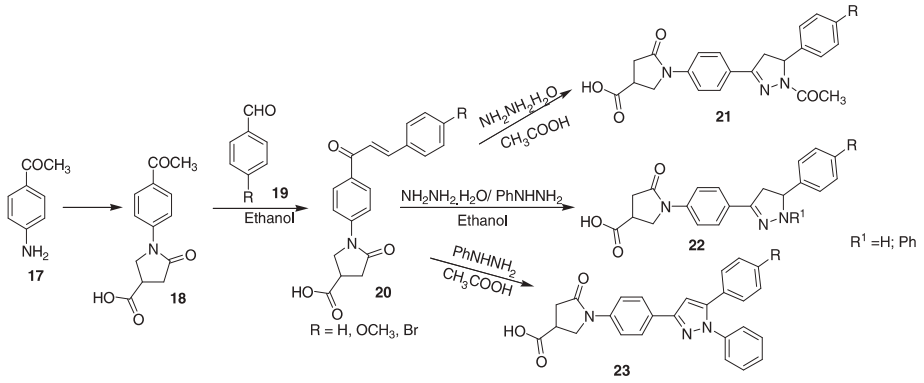

Scheme 4

The reaction of piperazine substituted chalcone (**24**) with phenyl hydrazine in ethanol in the presence of sodium hydroxide afforded piperazine substituted pyrazoline (**25**) in good to excellent yields (Scheme 5) [20]. The antimicrobial screening data of the synthesized hybrids **25** showed that the compounds depict good to excellent activity.

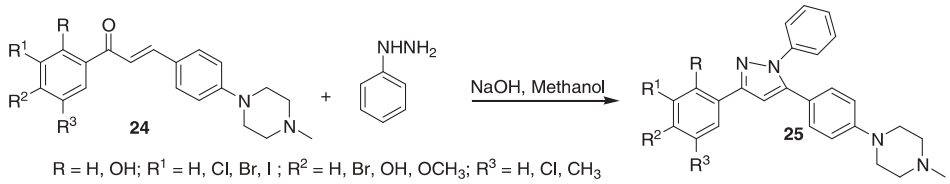

Scheme 5

The microwave irradiation of substituted aromatic aldehydes and substituted acetophenones in alc. KOH gave respective chalcones (**28**) in high yields (Scheme 6). The chalcone derivative **28** were treated with bromine in CCl_4 at room temperature to afford the corresponding dibromochalcones**29** in good yields. The consequent cyclization of bromochalcones**29** with hydrazine derivatives under MW conditions afforded the targeted pyrazolines **31** in excellent yields [21].

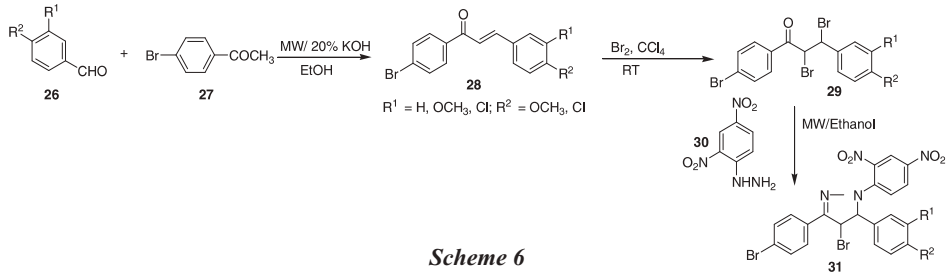

Scheme 6

The series of 1,3,5-trisubstituted pyrazolines derivatives (36) were prepared from the reactions of chalcone derivative 34 with aryloxy acetyl hydrazines 35 in the presence of glacial acetic acid in 70-80% yield (Scheme 7). Further, the synthesized compounds were screened for antibacterial, antifungal, and antitubercular activity studies. The data revealed that the compound 36 shows significant activity against ampicillin, moderate to significant antifungal activity against griseofulvin, and good antitubercular activities against isoniazid [22].

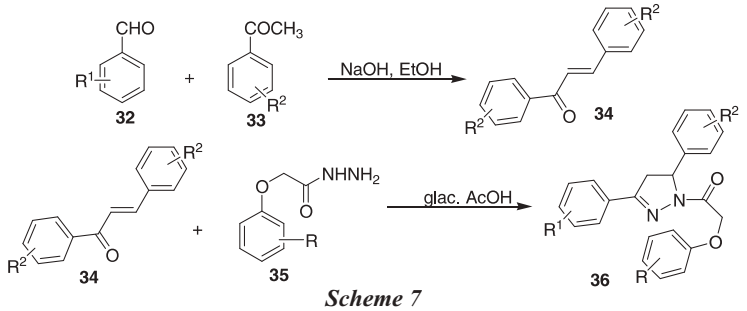

Scheme 7

Some pyrazoles and their novel derivatives **40** [23] were synthesized by cyclization of substituted chalcone **38** in presence of isonicotynyl hydrazide **39** (Scheme 8). The antibacterial and antifungal screening of the synthesized compounds **40** showed that pyrazolines with chloro phenyl, methoxy phenyl and hydroxyl phenyl substitution depicted more anti-bacterial activity where as hydroxy and methoxy phenyl substituted pyrazolines showed good antifungal activity.

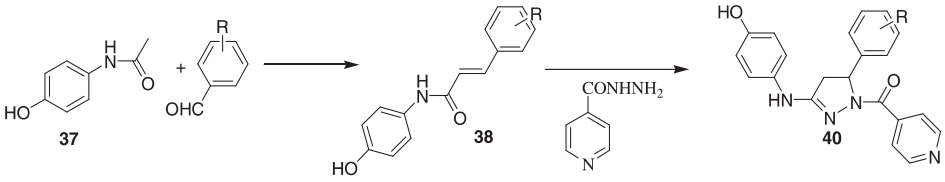

Scheme 8

Using the same methodology, Revanasiddappa *et al* [24] prepared 1,3,5-trisubstituted pyrazolines (**41**) from the cyclization of chalcones (**12**) with isoniazid (**39**) in presence of glacial acetic acid (Scheme 9). The chalcones **(12)** were synthesized by condensation of simple aldehydes with substituted acetophenones in presence of alkali. The *in vitro* antimicrobial activity data of compounds **41** against different strains of bacteria such as *P. aeruginosa, E. coli* (gram negative), *B. subtilis, S.aureus* (gram-positive) and fungi like *A. niger, C.albicans* revealed that most of the compounds are moderately active against both bacteria and fungi organisms.

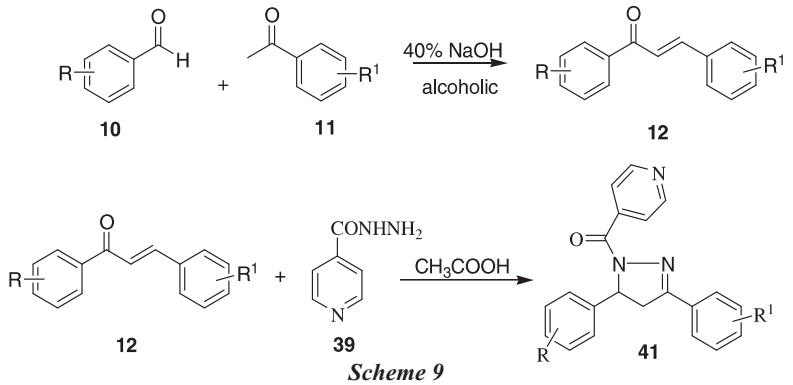

Scheme 9

Novel fatty acid chain substituted pyrazolines **44**/**45** [25] were synthesized from fatty acid hydrazides and 1-phenyl-3-furyl-2-propen-1-one (**42)**/1-phenyl-3 -chlorophenyl-2-propen-1-one (**43**) in refluxing dichloromethane and piperidine (Scheme 10).

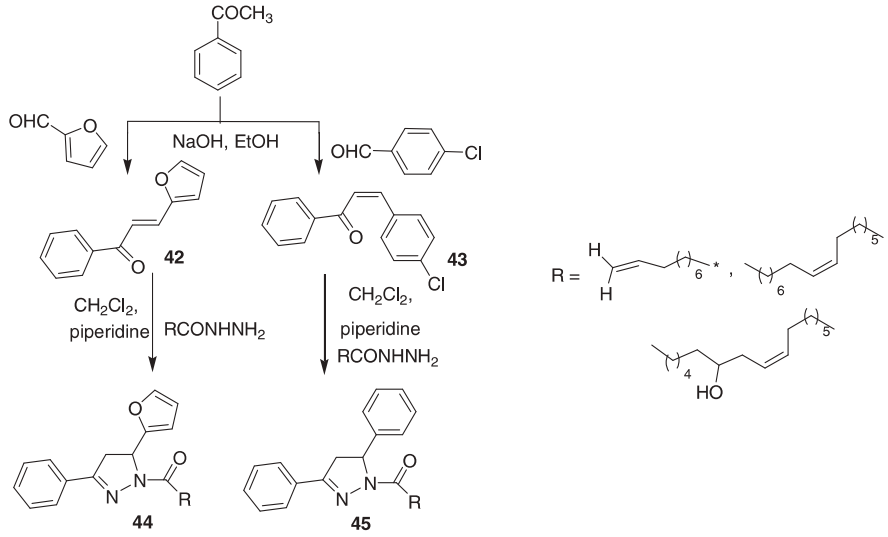

Scheme 10

The reaction of chalcone **46** with thiosemicarbazide **(47)** in dioxane containing a few drops of acetic acid gave pyrazolin-1-carbothioamides **48** (Scheme 11) in good yields [26]. Further, oxidation of pyrazolin-1-carbothioamide (**48**) with sodium hypochloride in dioxane led to the pyrazole-1-carbothioamides (**49**). The antimicrobial screening of compounds **48-49** against gram-positive, gram- negative bacteria and fungi showed that these compounds have moderate antimicrobial activity. Moreover, compound **49** bearing nitro substituent is the most active against all the screened microorganism.

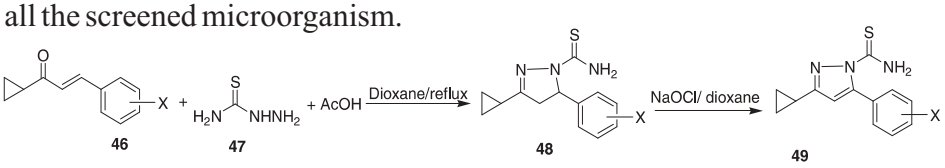

X = H, OCH_3, CH_3, NO_2

Scheme 11

Chawla *et al*. synthesized some novel 3-substituted phenyl-5-substituted phenyl-4,5-dihydro-pyrazole-1-carbothioamides (**50**) employing microwave technique and the synthesized compounds were evaluated for antimicrobial activity [27]. Antibacterial activities of **50** were determined against *S.aureus*, *B.subtilis*, *E.coli*and *Pseudomonas aeruginosa* and antifungal activity were screened against *C.albicans* and *A. niger*. The compounds exhibited moderate antibacterial and good

antifungal activity. Compounds having chloro and methoxy groups as substituents showed significant antifungal activity against *A.nige r*and *C.albicans* respectively.

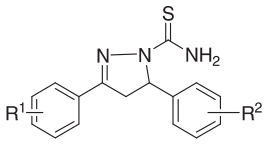

R^1 = 4-Cl, 4-OCH_3, 3-NO_2
R^2 = H, 4-Cl
50

III. Pyrazolines Derived From Hetroaromatic Chalcones

A. Pyrazolines Derived from Thiophene Substituted Chalcones

Ozdemir *et al* [28] prepared 1-[(N,N-disubstitutedthiocarb-amoylthio) acetyl]-3-(2-thienyl)-5-aryl-2-pyrazoline derivatives **57** by reacting 1-(chloroacetyl)-3-(2-thienyl)-5-aryl-2-pyrazolines (**55**) and appropriate sodium salts of N,N-disubstituted dithiocarbamoic acids (**56**) in acetone (Scheme 12). 5-Aryl-2-thienyl-2-pyrazolines (**54**) were obtained from the condensation of appropriate thienylchalcone (**53**) with hydrazine hydrate in refluxing ethanol. On further reaction with chloroacetyl chloride **54** afforded 1-(chloroacetyl)-3-(2-thienyl)-5-aryl-2-pyrazolines (**55**). The preliminary results of evaluation of *in vitro* antimycobacterial activity of 2-pyrazoline derivatives **57** against *Mycobacterium tuberculosis* H_{37}Rv using the BACTEC 460 radiometric system and BACTEC 12B medium showed that all of the tested compounds were inactive.

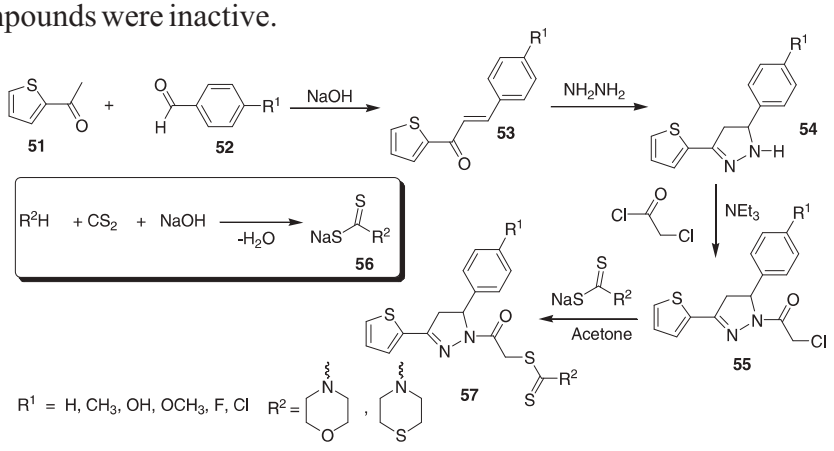

Scheme 12

Microwave irradiations are applied for solid phase cyclization of 5-bromo-2-thienyl chalcones (58) and phenyl hydrazine hydrate in the presence of fly ash, H_2SO_4 to prepare 1-phenyl-3 (5-bromothiophen-2-yl)-5 (substituted phenyl)-2-pyrazolines **59** (Scheme 13) [29]. All the synthesized pyrazoline derivatives (**59**) showed moderate antimicrobial activities against the strains used.

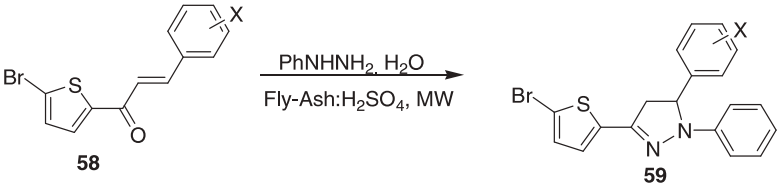

X = H, 4-Br, 2-Cl, 4-Cl, 4-CH_3, 3,4-$(OCH_3)_2$, 4-I, 4-OCH_3

Scheme 13

Thirunarayanan *et al* [30] reported microwave assisted solid acidic green catalyst SiO_2-H_3PO_4 catalyzed cyclization of 5-bromo-2-thienyl chalcones (**60**) and phenyl hydrazine hydrochloride under solvent free conditions (Scheme 14). Under these conditions, eight 1-phenyl-3(5-bromothiophen-2-yl)-5-(substituted phenyl)-2-pyrazoline derivatives (**61**) have been synthesized.

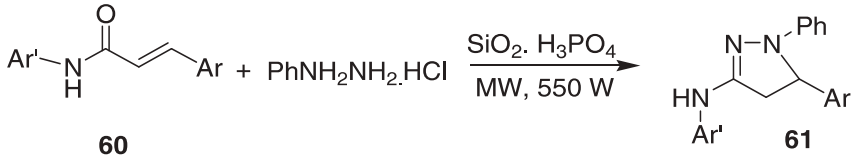

Ar = C_6H_5, 4-ClC_6H_4, 4-OHC_6H_4 Ar' = 4-$NO_2C_6H_4$, 4-ClC_6H_4, 4-OHC_6H_4

Scheme 14

B. Pyrazolines Derived from Furan Substituted Chalcones

Jothikrishnan *et al* [31] prepared pyrazoline derivative containing furan moiety **64** using microwave irradiation (Scheme 15). The reaction of **62** which was prepared by the reaction between 6-bromopiperonal and 2-furylacetone with **63** in absolute ethanol in the presence of microwave irradiation afforded furan substituted pyrazoline **64** in 80% yield.

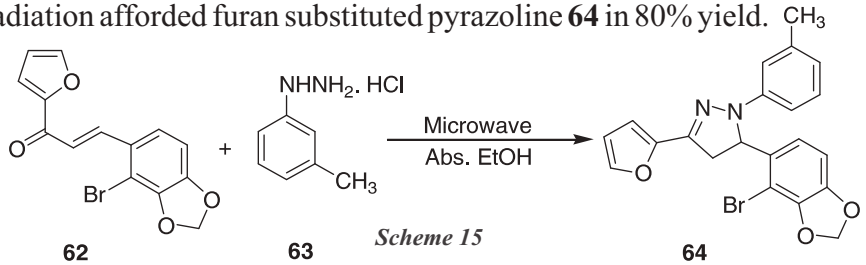

Scheme 15

Vidhiya *et al* obtained pyrazoline **66** upon refluxing chalcone (**65**) and isoniazid in glacial acid [32]. The pyrazolines **68** and **69** were obtained from the reaction of intermediate (**67**) with benzoyl chloride and benzene sulfonyl chloride respectively (Scheme 16). Further, the intermediate **67** is prepared from the reaction of chalcone (**65**) with hydrazine hydrate in ethanol. All the synthesized pyrazolines bearing piperonal were evaluated for their antibacterial activity against *Escherichia coli*, *Staphylococcus* aureus, *Pseudomonas* aeruginosa and *Klebsiella* pneumonia bacterial strains by the disc diffusion method and for antifungal activity against *Aspergillus* niger, *Candida albicans*. Most of them showed the moderate to low antibacterial activity. The compound **66** showed good inhibition towards all the four bacteria as well as against the two fungi tested.

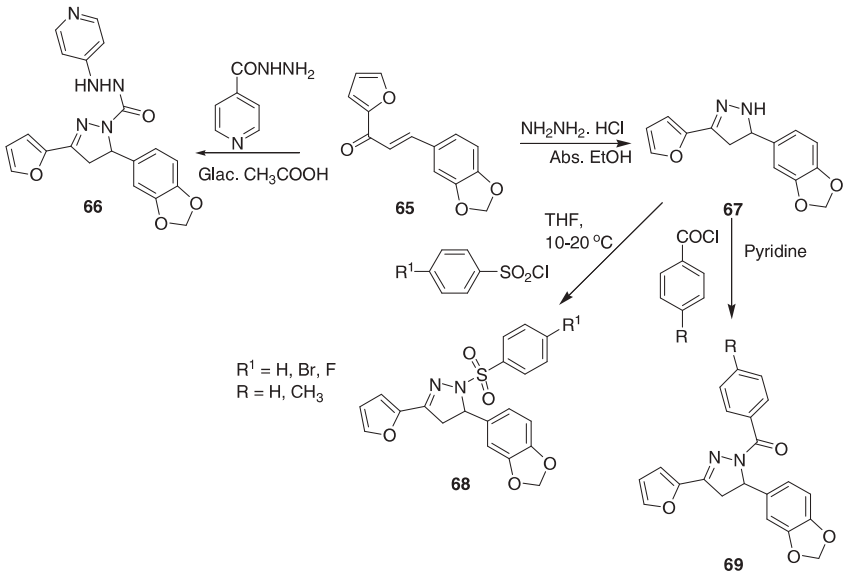

Scheme 16

Phirke *et al* [33] condensed furylchalcone (**72**) with phenyl hydrazine to obtain furylpyrazoline **73** (Scheme 17). The reaction of 2-furyl acetone (**70**) and appropriately substituted benzaldehyde (**71**) in ethanolic sodium hydroxide afforded furylchalcone (**72**). The compounds obtained were evaluated for antibacterial activity. All the synthesized compounds (**73**) depicted appreciable activity.

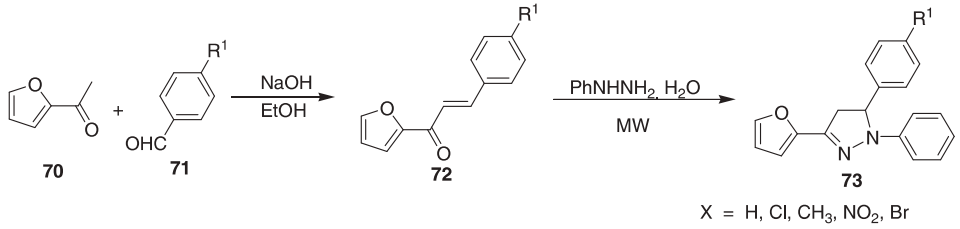

70 71 72 73

Scheme 17

Rahmen *et al* [34] synthesized 3, 5- diphenyl (**77**) and furylpyrazoline derivatives (**81**) by the reaction of appropriate chalcone **76** or **80** with 2,4-dinitrophenylhydrazine,semicarbazide, phenylhydrazine or hydrazine in ethanol (Scheme 18). The corresponding chalcones [1, 3-diphenyl prop-2-ene-1-ones **(76)** and 3-furyl-1-phenylprop-2-ene-1-ones **(80)**] were prepared by condensing appropriate acetophenone (**74**)/furylacetone derivatives (**78**) and benzaldehyde derivatives (**75/79**) respectively in ethanolic sodium hydroxide. Further**,** the antidepressant and anticonvluscent activities of all the synthesized compounds (**77**/**81**) were evaluated. The data revealed that compounds having a furyl substituent (**81**) at 5th position of pyrazoline ring have notable anticonvulsant activity. The compounds (R^1 =$CSNH_2$, 2,4-dinitrophenyl; R^2= H; R^3= H, OH ; R^3= OCH_3, Cl, H) depict good antidepressant whereas the compounds (R^1 =$CSNH_2$, 2,4-dinitrophenyl; R^2= H; R^3= H, OH ; R^3= OCH_3, Cl, H) have good anticonvulsant activity.

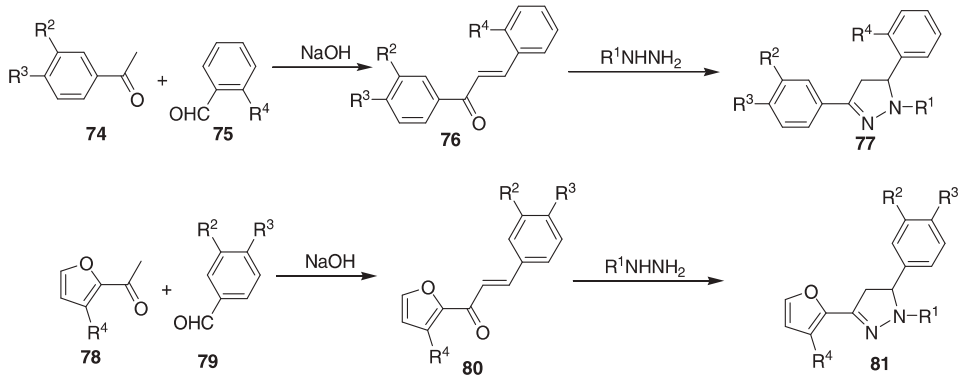

74 75 76 77

78 79 80 81

Scheme 18

C. Pyrazolines Derived From Triazole Substituted Chalcones

The library of 1,2,3-triazolyl-N-acetyl/N-propionylpyrazole hybrids (**85**) were prepared by heating mixture of 1,2,3-triazolyl chalcone (**84**) and hydrazine hydrate in acetic acid (Scheme 19) [35]. The 1,2,3-triazolyl chalcone (**84**) was obtained by grinding the mixture of **82** and **83** in the presence of NaOH.

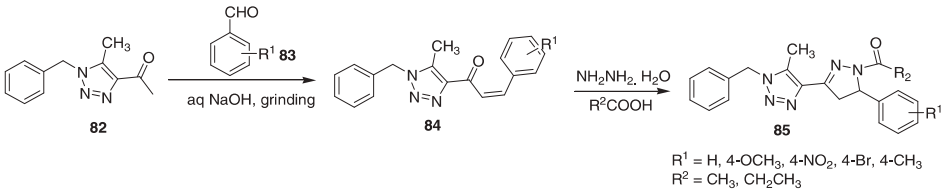

Scheme 19

D. Pyrazolines Derived from Triazine Substituted Chalcones

The reaction of **[2,4-bis-(2',4'-difluorophenylamino)-6-[4′-{5″-(4‴-methoxyphenyl)2''-propenon-1''-yl}phenyl amino]-*s*-triazine]** derivatives (**88**) with phenylhydrazine hydrochloride in ethanol in the presence of 40% KOH yielded triazine based pyrazoline (**89**) in good yields (Scheme 20). The triazine based chalcone (**88**) was prepared by the condensation of triazine **87** dissolved in DMF with appropriate aldehyde in the presence of KOH [36].

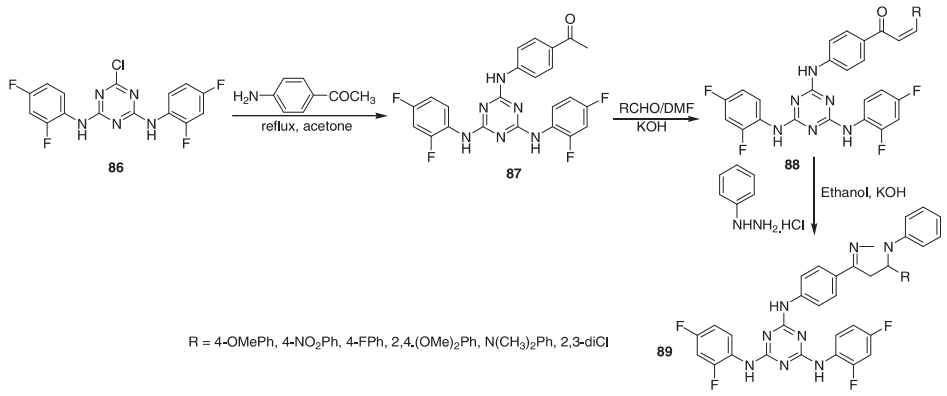

Scheme 20

E. Pyrazolines Derived From Quinoline Substituted Chalcones

Pyrazolines bearing quinolinyl motif (**93**) were prepared by the condensation of chalcone **92** with 2-[(quinolin-8-yl)oxy]acetohydrazide

(**91**) in glacial acetic acid (Scheme 21). The quinoline hydrazide precursor (**91**) was obtained from the reaction of 8-hydroxyquinoline with ethylchloroacetate in dry acetone in the presense of potassium carbonate followed by the condensation with hydrazine hydrate [37]. The antimicrobial, antifungal and anti-inflammatory screening of synthesized compounds (**93**) showed that all the compounds depict significant activity.

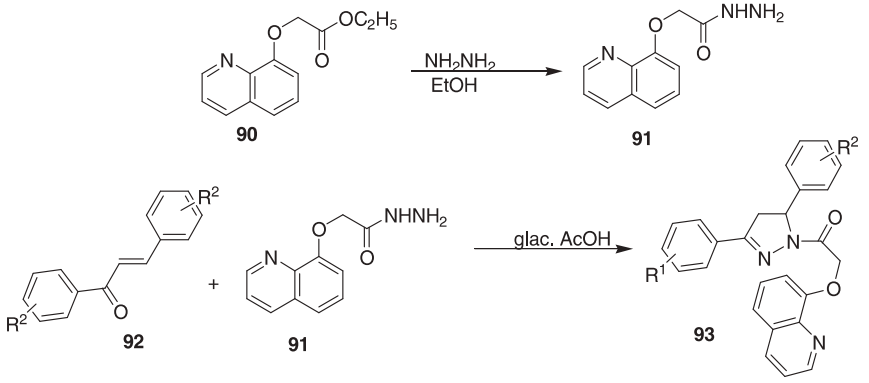

Scheme 21

Using the quinoline (**94**) and acetyl sydnone (**95**) derivatives as the starting materials, Lamani et al [38] obtained chalcone (**96**) which upon reaction with phenyl hydrazine afforded pyrazolines **97** (Scheme 22). Further, reaction of pyrazoline with bromine in acetic anhydride led to pyrazoline derivative **98**. All the newly synthesized compounds (**97**/**98**) were screened for their antimicrobial activity at 100 µg/mL concentration against the bacterial strains viz., E. coli, B. subtilis using Norfloxacin as standard and also against fungal strains viz., A. *niger* and A. *sereus* using Griseofulvin as the reference drug. The data revealed that all these compounds were less active against the bacterial strains, but some of them showed selective fungal inhibitory activity.

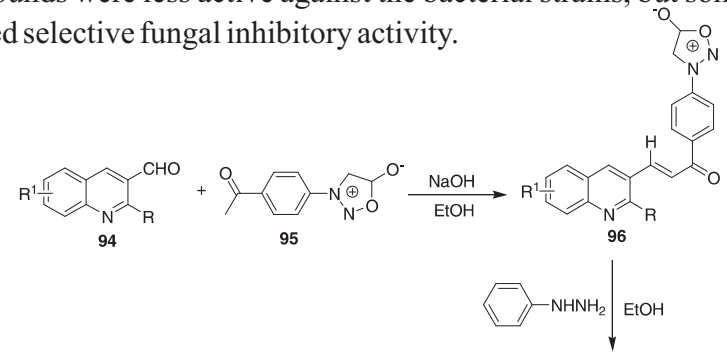

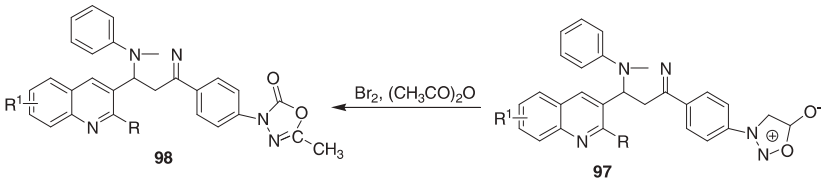

Scheme 22

F. Pyrazolines Derived From Indole Substituted Chalcones

Faritha *et al* [39] reported 5-(1H-indol-3-yl)-3-phenyl-4,5-dihydropyrazole-1-carbothioamide derivatives (**102**). The synthesis involve reaction of (*E*)-3-(1H-indol-3-yl)-1-substituted phenylprop-2-en-1-one **100** with thio-semicarbazide **101** in the presence of sodium hydroxide in ethanol (Scheme 23). The *in-vitro* antibacterial and antifungal screening against various strains of microbial organisms showed that out of the six compounds, the compound **102** (R = OH) showed good antibacterial and antifungal activities against all the tested organisms.

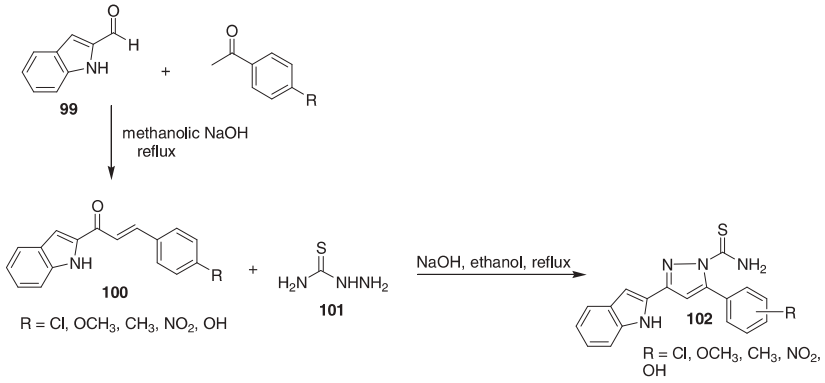

Scheme 23

IV. Conclusions

The chalcones serve as useful precursors for the synthesis of variously substituted pyrazolines. A variety of substituents can be easily appended on pyrazoline motif by using appropriately substituted chalcone precursors. The pyrazoline derivatives obtained from aromatic and hetroaromatic chalcones exhibit excellent biological activity. The pyrazolines bearing chloro phenyl, methoxy phenyl and hydroxyl phenyl substitution depict excellent anti-bacterial activity. Further, the biological activities of the pyrazoline derivatives compiled in this review indicated that there is ample

scope for further study in developing these as good lead compounds for the treatment of bacterial strain as well as fungal strain.

V. References

[1] W. C. Howell, M. Ktenas and J. M. MacDonald, "Reaction of duroquinone with diazomethane: formation of tricycle [5.1.0.0] octane derivatives" Tetrahedron Lett. 26 (1964) 1719-1724.

[2] L. C. Raiford and J. B. Entrikin, "Rearrangement of phenyl hydrazones of some unsymmetrically substituted dibenzalacetones" J. Am. Chem. Soc. 55 (1933) 1125-1128.

[3] D. Nauduri and G. B. Reddy, "Antibacterials and antimycotics: part 1: synthesis and activity of 2-pyrazoline derivatives" Chem. Pharm. Bull (Tokyo) 46 (1998) 1254-1260.

[4] S. S. Korgaokar, P. H. Patil, M. T. Shah and H. H. Parekh, "Studies on pyrazolines : preparation and antimicrobial activity of 3-(p-chlorophenylsulphonamidophenyl)-5 aryl- 1h/acetyl pyrazolines" Indian J. Pharm. Sci., 58 (1996) 222-225.

[5] F. F. Barsoum, H. M. Hosni and A. S. Girgis, "Novel bis(1-acyl-2-pyrazolines) of potential anti-inflammatory and molluscicidal properties" Bioorg. Med. Chem., 14 (2006) 3929-3937.

[6] S. Sridhar and Y. Rajendraprasad, "Synthesis and analgesic studies of some new 2-pyrazolines" E-J. Chem. 9 (2012) 1810-1815.

[7] T. S. Jeong, K. S. Kim, J. R. Kim, K. Y. Cho, S. Lee and W. S. Lee, "Novel 3,5-diaryl pyrazolines and pyrazole as low-density lipoprotein (ldl) oxidation inhibitor" Bioorg. Med. Chem. Lett., 14 (2004) 2719-2723.

[8] P. L. Zhao, F. Wang, M. Z. Zhang, Z. M. Liu, W. Huang and G. F. Yang, "Synthesis, fungicidal, and insecticidal activities of beta-methoxyacrylate-containing n-acetyl pyrazoline derivatives" J. Agric. Food Chem., 56 (2008) 10767-10773.

[9] N. Mishriky N, F. M. Asaad, Y.A. Ibrahim and A. S. Girgis, "New 2-pyrazolines of anticipated molluscicidal activity" Pharmazie. 51 (1996) 544-548.

[10] E. Palaska, M. Aytemir, I. T. Uzbay and D. Erol, "Synthesis and antidepressant activities of some 3,5-diphenyl-2-pyrazolines" Eur. J. Med. Chem. 36 (2001) 539-543.

[11] A. J. Kasabe and P. J. Kasabe, "Synthesis, anti tubercular and analgesic activity evaluation of new pyrazoline derivatives" Int. J. Pharmacy Pharm. Sci., 2 (2010) 132-134.

[12] M. A. Ali, M. S. Yar, A. A. Siddiqui, D. Sriram, P. Yogeeswari and E. D. Clercq, "Synthesis and anticancer and antiviral activities of new 2-pyrazoline substituted 4̃thiazolidinones" Acta Pol. Pharm. Drug Res., 63 (2007) 423-428

[13] B. N. Acharya, D. Saraswat, M. Tiwari, A. K. Shrivastava, R. Ghorpade, S. Bapna and M. P. Kaushik, "Synthesis and antimalarial evaluation of 1, 3, 5-trisubstituted pyrazolines" Eur. J. Med. Chem., 45 (2010) 430-438.

[14] D. Havrylyuk, B. Zimenkovsky, O. Vasylenko, A. Gzella and R. Lesyk, "Synthesis of new 4-thiazolidinone, pyrazoline, and isatin-based conjugates with promising antitumor activity" J. Med. Chem., 55 (2012) 8630-8641.

[15] X. Q. Cao, X. H. Lin, Y. Zhu, Y. Q. Ge and J. W. Wang, "The optical properties, synthesis and characterization of novel 5-aryl-3-benzimidazolyl-1-phenyl-pyrazoline derivatives. Spectrochim Acta A Mol Biomol Spectrosc. 98 (2012) 76-80.

[16] P. M. Sivakumar, S. Ganesan, P. Veluchamy and M. Doble, "Novel chalcones and 1,3,5-triphenyl-2-pyrazoline derivatives as antibacterial agents" Chem Biol Drug Des 76 (2010) 407-411.

[17] S. G. Konda, A. H. Valekar, S. T. Lomate, P. D.Lokhande and B. S. Dawane. "Synthesis and antibacterial studies of some new pyrazoline and isoxazoline derivatives" J. Chem. Pharm. Res., 2 (2010) 187-191.

[18] V. Arora, P. Arora and H. S. Lamba, "Synthesis and biological activities of some 3, 5-disubstitutedpyrazoline derivatives of 2-acetyl naphthalene" Int J Pharm Pharm. Sci, *4 (2012) 303-306.*

[19] A. Voskiene, V. Mickevicius and G. Mikulskiene, "Synthesis and structural characterization of products condensation 4-carboxy-1-(4-styrylcarbonylphenyl)-2-pyrrolidinones with hydrazines" ARKIVOC xv (2007) 303-314.

[20] S. S. N. Na, H. M. Ziauddin, M. Zameer, S. S. Hingole and M. A. Baseer, "An introduction of some novel pyrazolines to synthetic chemistry and antimicrobial studies" J. Chem. Pharm. Res., 2 (2010) 441-445.

[21] M. Russella, I. M. Hosseina, N. E. -Alomb, M. M. Hossaina and M. K. Islamc, "An expedite synthesis of bioactive pyrazolines under microwave irradiation" Int. J. Org. Bioorg. Chem. 4 (2014) 14-16.

[22] I. K. Bhat and P. J. Jainey, "Antimicrobial studies of some substituted pyrazoline derivatives derived from acetyl hydrazines" Asian J Pharm Clin Res, 7 (2014) 237-239.

[23] N. Ramalakshmi, S. Deepa , K. S. Srinivas, A. Puratchikody and S. A. kumar, "Synthesis, characterization and biological screening of some novel 1,3,5-trisubstituted 2-pyrazolines" Rasayan J Chem. 2 (2009) 393-396.

[24] B. C. Revanasiddappa, R. Nagendra Rao, E. V. S. Subrahmanyam and D. Satyanarayana, "Synthesis and biological evaluation of some novel 1, 3, 5-trisubstituted pyrazolines" E-Journal of Chemistry, 7 (2010) 295-298.

[25] K. Laskar, A. Ahmad and A. Rauf, "Synthesis and spectral characterization of novel fatty acid chain substituted pyrazoline derivatives" Rasayan. J. Chem.7 (2014) 276-280.

[26] E. M. Sharshira and N. M. M. Hamada, "Synthesis, Antibacterial and Antifungal Activities of Some Pyrazole-1-Carbothioamides and Pyrimidine-2(1H)-Thiones" Am. J. Org. Chem. 2 (2012) 26-31.

[27] R. Chawla, U. Sahoo, A. Arora, P.C. Sharma and V. Radhadrishnan, "Microwave assisted synthesis of some novel 2-pyrazoline derivatives as possible antimicrobial agents" Acta Pol. Pharm. 67 (2010) 55-61.

[28] A. Ozdemir, G. Zitouni and Z. A. Kaplancikli, "Novel analogues of 2-pyrazoline: synthesis, characterization, and antimycobacterial evaluation" Turk J Chem 32 (2008) 529-538.

[29] R. Sasikala, K.Thirumurthy, P. Mayavel and G. Thirunarayanan, "Eco-friendly synthesis and antimicrobial activities of some 1-phenyl-3(5-bromothiophen-2-yl)-5-(substituted phenyl)-2-pyrazolines" Org. Med. Chem.Lett. 2 (2012) 1-13.

[30] G. Thirunarayanan, P. Mayavel, K. Thirumurthy, S. D.kumar, R. Sasikala, P. Nishaand and A. Nithyaranjani, "Eco-friendly synthesis and spectral correlations. In some 1-phenyl-3-(5-bromothiophen-2-yl)-5-(substituted phenyl)-2-pyrazolines" Eur. Chem. Bull., 2(2013) 598-605.

[31] B. T. Jothikrishnan, and S. S. Shafi, "Synthesis of a 2-Furylpyrazoline Derivative Using Microwave Irradiation" Mol bank (2009) M613.

[32] K. R. Vidhya, and S. Shafi, "Synthesis, characterization and antimicrobial studies of novel 2-pyrazoline derivatives" Der Pharma Chemica, 6 (2014) 283-287.

[33] J. V. Phirke and Y. K. Meshram, "Microwave assisted synthesis and antibacterial activity of substituted 2-furyl pyrazoline derivatives" Ind. J. App. Res. 4 (2014) 537-538.

[34] T. Rahaman, M. A. Khan and B. Ahmed, "Synthesis of some 3, 5-diphenyl -Δ1pyrazoline and 5-(2′′-furyl)-Δ1- pyrazoline derivatives and their screening for antidepressant and anticonvulsant activity" IJPSR, 5 (2014) 3226-3234.

[35] P. Shanmugavelan, M. Sathishkumar, S. Nagarajan and A. Ponnuswamy, "An efficient and facile synthesis of novel 1,2,3-triazolyl-N-acylpyrazoline hybrids" Chinese Chem. Lett. 25 (2014) 146-148.

[36] A. N. Solankee, K. P. Patel and R. B. Patel, "A convenient synthesis of chalcones, aminopyrimidines and phenylpyrazolines" Der Chemica Sinica, 2 (2011) 1-7.

[37] S. K. Chaitanya, I. Bhat, R. Sidhappa, Satyanarayana and B. Kalluraya, "Synthesis and biological activity studies of some pyrazoline derivatives containing quinoline moiety" J. Ind. Council Chem. 26 (2009) 37-40.

[38] K. S. S. Lamani, and O. Kotresh, "Quinoline based 2-pyrazoline derivatives synthetic and pharmacological approach" Chem Sci Trans., 2 (2013) 1528-1536.

[39] Faritha, N. Aja, Ahamed and Thajuddin, "Synthesis, characterization and antimicrobial evaluation of certain pyrazolines" Int. J. Pharm Res Bio-Sci. 3 (2014) 516-527.

Curr. Rep. Sci. & Tech. 1 (2) (2015) 112-118

Nonlinear Electron Acoustic Waves in Multispecies Plasma With Non-Maxwellian Electrons

Harvinder Kaur[a] and Tarsem Singh[b]
[a]Department of Physics, Khalsa College Amritsar (India)
[b]Department of Physics, Guru Nanak Dev University, Amritsar (India)
hkaur21@yahoo.com

Abstract

Nonlinear propagation of electron-acoustic waves were investigated in an unmagnetized plasma consisting non-Maxwellian hot, cold and beam electrons and ions. The Sagdeev potential technique is used to carry out the analysis. The rarefactive solitons exist for the different parameters regime. Thesolitons formation is markedly influenced by the distribution of the electrons and beam electron parameters. The presence of electron beam modifies the parameter regime where the electron acoustic solitons exist. The dependence of amplitude on the different parameters is also investigated.

I. Introduction

For the first time the idea of electron-acoustic (EA) waves have originated for the explanation of numerical solutions of the linear electrostatic Vlasov dispersion equation in an unmagnetized, homogeneous plasma in the mind of Fried and Gould [1]. EA waves were observed in the laboratory when the unmagnetized plasma is composed of two electron populations, described by two Maxwellian distribution functions with different temperature and density. These two populations will be referred to as cold and hot electrons [2-4]. The wave is analogous to ion-acoustic wave. The cold electron in EA mode plays the role of cold ions in the ion-acoustic mode. The ions dynamics plays no role in EA solitary wave. They are simply required for charge neutralization [5]. The propagation characteristics of the EA waves have been studied by a number of authors.

Gary and Tokar [6] performed a parameter survey and found

conditions for the existence of the EA waves. The most important condition is $T_c << T_h$, where T_c (T_h) is the temperature of cold(hot) electrons. Another condition for the existence of this wave is that the hot electron population should represent a significant fraction of the total electron density (probably more than 20%).

As plasmas with two electrons population, are known to occur frequently both in laboratory experiments and space, EA wave plays an important role in these environments [5]. In the earth's bow shock, particularly in the upstream region, the electron-acoustic waves have been suggested as a possible source of broadband electrostatic noise (BEN). They are also of potential importance in interpreting BEN observed in cusp of terrestrial magnetosphere in auroral region and in geomagnetic tail [7-9].The EA mode has also been used to explain various wave emissions in different regions of the Earth's magnetosphere. Furthermore, the EA mode has been applied to interpret the hiss observed in the polar cusp region.

Dubouloz etal. [10,11] rigorously studied the BEN observed in the day side of auroral zone and explained short duration burst of BEN in terms of EA solitary waves. They considered a one dimensional unmagnetized collisionless plasma consisting of cold electrons, Maxwellian hot electrons and stationary ions. A study of nonlinear properties of larger amplitude necessarily useful for understanding BEN was pointed by Mace et al [12]. In the presence of large electron beam energy, the nonlinear effects combine with the dispersive properties of the EA wave which leads to formation of EA solitons[5]. This leads to the existence of new electron-acoustic solitons with velocity related to beam velocity. Berthomieretal. [5] pointed out that the positive potential structure is very important from the point of view of the interpretation of various electrostatic structures observed in the auroral region at intermediate altitude by FAST, at higher altitudes by POLAR and in geomagnetic tail by GEOTAIL. Mace and Helberg [13] studied the effect of a magnetic field on electron-acoustic solitons. They derived KdV-ZK equation for weakly nonlinear EA waves and discussed its solitonic solutions.

Carins et al [14] explained the structure of solitary waves using nonthermal distribution for electrons. Singh and Lakhina [15] have studied

EA solitons using nonthermal electron distribution with ion dynamics. In present investigation, we studied the role of nonthermal hot electron distribution with cold electron and beam electrons in characterizing the behaviour of EA solitons.

II. Basic Equations

Let us consider a collisionles sunmagnetized homogeneous plasma consisting of a cold electron fluid, beam electrons and hot electrons obeying a non-Maxwellian distribution with stationary ions. The dynamics of EA waves is governed by

$$\frac{\partial n_c}{\partial t} + \frac{\partial (n_c\, u_c)}{\partial x} = 0 \tag{1}$$

$$\frac{\partial u_c}{\partial t} + u_c \frac{\partial u_c}{\partial x} = \alpha \frac{\partial \phi}{\partial x} - 3\sigma\alpha(1+\alpha+\gamma)^2 n_c \frac{\partial n_c}{\partial x} \tag{2}$$

$$\frac{\partial n_b}{\partial t} + \frac{\partial (n_b\, u_b)}{\partial x} = 0 \tag{3}$$

$$\frac{\partial u_b}{\partial t} + u_b \frac{\partial u_b}{\partial x} = \alpha \frac{\partial \phi}{\partial x} - 3\sigma_b\, \alpha \left(\frac{1+\alpha+\gamma}{\gamma}\right)^2 n_b \frac{\partial n_b}{\partial x} \tag{4}$$

$$\frac{\alpha}{1+\alpha+\gamma} \frac{\partial^2 \phi}{\partial x^2} = n_c + n_h + n_b - 1 \tag{5}$$

where n_c,$n_{h,}$ and denote cold , hot and beam electron density respectively normalized by n_{co}. The time is normalized by the plasma period

$$\omega_{pc}^{-1} = \left(\frac{m}{4\pi n_{co} e^2}\right)^{1/2} \tag{6}$$

and space variable by the hot electron Debye length

$$\lambda_{Db} = \left(\frac{k_B T_h}{4\pi n_{co} e^2}\right)^{1/2} \tag{7}$$

the hot electrons are assumed to be non-Maxwellian distributed. The electron number density associated with hot electrons is given by

$$\frac{1+\alpha+\gamma}{\alpha} n_h = (1 - \beta\, \phi + \beta\, \phi^2) e^{\phi} \tag{8}$$

where $\sigma = T_c/T_h$,$\alpha = n_{h0}/n_{co}$, $\sigma_b = T_b/T_h$ and $\gamma = n_{b0}/n_{co}$

we seek solution to basic equations that are stationary in a frame

moving with velocity M. Using the transformation χ=x-M t and applying the appropriate boundary conditions, Poisson's equation can be integrated to yield energy integral

$$\frac{1}{2}\left(\frac{\partial\phi}{\partial x}\right)^2 + V(\phi) = 0 \tag{9}$$

where V(ø) is the Sagdeev Potential given by

$$\begin{aligned} V(\phi) = {} & 1 + 3\,\beta - (1 + 3\beta - 3\beta\phi + \beta\phi^2) + \frac{1+\alpha+\gamma}{\alpha}\phi \\ & - \frac{1}{3\alpha^2\sqrt{12\sigma\alpha}}\left(\left(M + \sqrt{3\sigma\alpha}\right)^2 + 2\alpha\phi\right)^{3/2} - \left(\left(M - \sqrt{3\sigma\alpha}\right)^2 + 2\alpha\phi\right)^{3/2}\Big) \\ & - \frac{\gamma}{3\alpha^2\sqrt{12\sigma_b\alpha}}\left(\left(M + \sqrt{3\sigma_b\alpha}\right)^2 + 2\alpha\phi\right)^{3/2} - \left(\left(M - \sqrt{3\sigma_b\alpha}\right)^2 + 2\alpha\phi\right)^{3/2}\Big) \\ & + \frac{1}{3\alpha^2\sqrt{12\sigma\alpha}}\left(\left(M + \sqrt{3\sigma\alpha}\right)^3 + \left(M - \sqrt{3\sigma\alpha}\right)^3\right) \\ & + \frac{\gamma}{3\alpha^2\sqrt{12\sigma_b\alpha}}\left(\left(M + \sqrt{3\sigma_b\alpha}\right)^3 + \left(M - \sqrt{3\sigma_b\alpha}\right)^3\right) \end{aligned} \tag{10}$$

III. Numerical Results

The soliton solution of equation (10) exist when the usual conditions, namely, $V(\phi) = dV(\phi)/d\phi = 0$ at and $V(\phi) < 0$ for $0 < |\phi| < |\phi_0|$ for , where ϕ_0 is the maximum amplitude of the solitons, are satisified. The equation s (9) and (10) are solved numerically for the soliton amplitude and Sagdeev potential, respectively. The parameters for the numerical evaluation are cold electron density, n_{0c}=0.35 cm^{-3}, hot electron density, n_{0h}=0.65 cm^{-3} and n_{bo}=1.0cm^{-3}

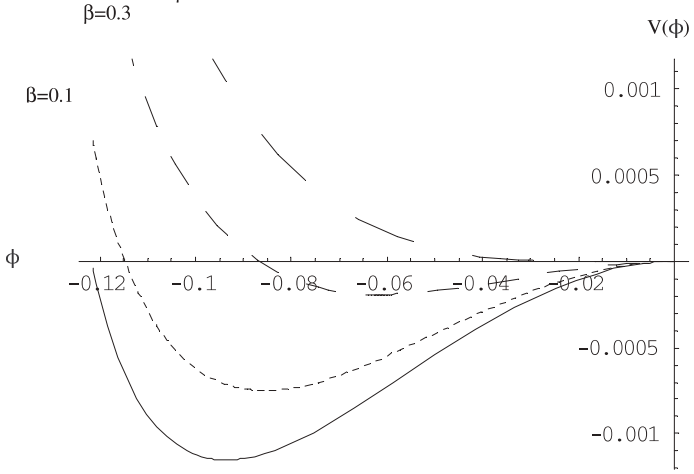

Fig 1*.The variation of Sagdeev potential with potential ϕ for different values of β. Other parameters are α=7.5, γ=0, M=1.5, σ=0.001*

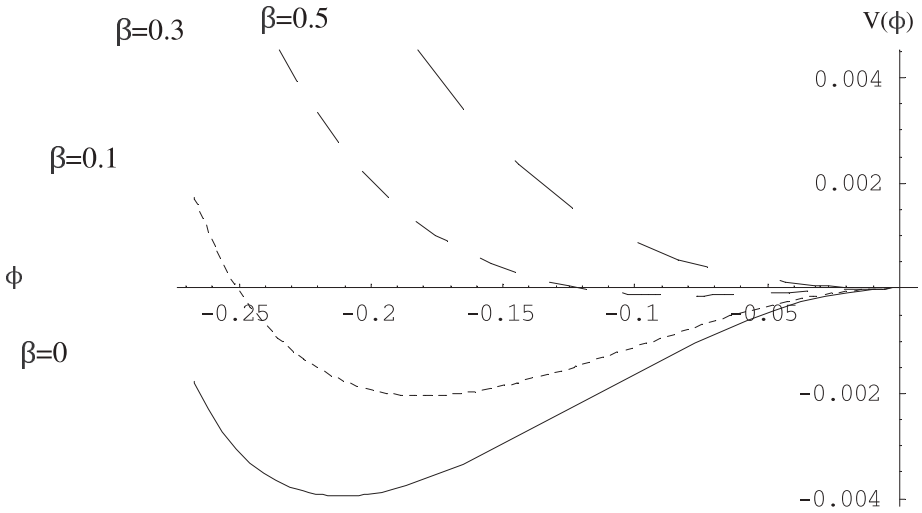

Fig 2*.The variation of Sagdeev potential for different values of β. Other parameters are α=7.5, γ=5, M=3.5, σ=0.001, σ_b=0.1*

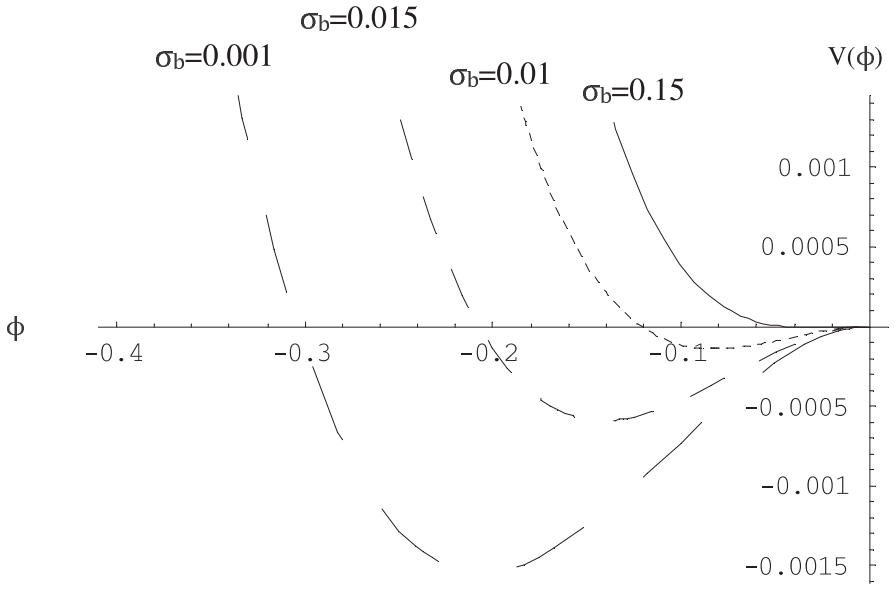

Fig 3. *The variation of Sagdeev potential with potential for different values of σ_b . Other parameters are α=7.5, γ=5, M=3.5, σ=0.001, β =0.3*

Fig 1.shows the variation of Sagdeev potential v (ϕ) with potential ϕ for the above mentioned parameters for the various values of β withmach number M=1.5 and σ=0.001. It is interesting to point out that no soliton exist for β=0 (Maxwellian distribution). However, for nonthermal distribution, solitons exits for <0 β <0.5 . This implies the nonthermal distribution is favourable for the formation of solitons. The effect of beam electrons is shown in Fig 2. At σ_b=0.1, solitonexist formach number M=3.5 in the regime of o< β <0.5. It is further observed that the increase of β leads to decrease of amplitude. It implies that the solitons formation take placeat mach number M=3.5 i.e. for high soliton speed as compared to those without beam. Fig. 3 exhibits the variation of soliton profile for the different values of σ_b, the other parameters are same as those in Fig 2. for β=0.3. It is noticed that increase of beam temperature leads to the decrease of amplitude. The solitons exist for σ_b<0.15. In general, it is clear that with introduction of nonthermal distribution and beam electrons modifies the parameters region where the electron acousticsolitons can exist. It may be noticed that in given situations, only rarefactive electron acoustic solitons are permissible.

IV. References

[1] B. D. Fried and R. W. Gould, Longitudinal ion oscillations in a hot plasma Phys. Fluids, 4 (1961) 139-147.

[2] H. Derflerand T.C.Simonen, Higher-order Landau Modes, Phys. Fluids,12(1969)269-278.

[3] D. Henry and J. P. Treguier, Propagation of electronic longitudinal modes in a non-Maxwellian plasma, Plasma Phys., 8(1972)311-319.

[4] S. Ikezawa and Y. Nakamura, Observation of Electron Plasma Waves in Plasma of Two-Temperature Electron, J. Phys. Soc. Jpn., 50 (1981) 962-967.

[5] M.Berthomier, R.Pottelette, M. Malingreand Y. Khotyainpsev, Electron acoustic solitons in an electron-beam plasma system,Phys. Plasmas, 7(2000) 2987-2994.

[6] S. P.Gary and R.L. Tokar., Electron-acoustic mode, Phys. Fluids, 28(1985)2439-2441.

[7] R.L.Tokar and S.P. Gary, Electrostatic hiss and the beam driven electron-acoustic instability in the dayside polar cusp,Geophys. Res. Lett., 11(1984)1180-1183.

[8] S.V. Singh and G.S. Lakhina,Generation of Electron-Acoustic waves in the Magnetosphere, Planetary Space Sci.49(2001)107-114.

[9] D. Schriver and M. Ashour-Abdalla, Broadband electrostatic noise due to field aligned currents, *Geophys. Res. Lett.,* 16(1989)899-902.

[10] N.Dubouloz, R.Pottelette, M.Malingre, G. Holmgren and P.A.Lindqvist, Detailed analysis of broadband electrostatic noise in the dayside auroral zone, J. Geophys. Res. 96(1991a)3565-3579.

[11] N. Dubouloz, R.A.Treumann, R. Potteletteand M. J.Malingre, Turbulence generated by a gas of electron-acoustic solitons, Geophys. Res. , 98(1993)17415-17422.

[12] R.L.Mace, S.Baboolal, R. Bharuthram and M.A. Hellberg, Arbitrary-amplitude electron-acoustic solitons in a two electron component plasma, J. Plasma Phys., 45 (1991) 323-338.

[13] R.L. Mace and M.A. Hellberg, The Korteweg-de Vries Zakharov-Kuznetsov equation for electro-acoustic waves, Phys. Plasmas, 8 (2001) 2649-2656.

[14] R.A. Cairns, A.A.Mamun, R.Bingam, R.Bostrom, R.O.Dendy, C.Nairn and P.K.Shukla, Electrostatic solitary structures in nonthermal plasma, Geophys. Res. Lett., 22(1995)2709-2712.

[15] S.V. Singh. and G.S. Lakhina, Electron-acoustic solitary waves with nonthermal distribution of electrons, Nonlinear Processes in Geophysics, 11(2004)275-279.

Curr. Rep. Sci. & Tech. 1 (2) (2015) 119-123

Effect of Heavy Ion Irradiation on Conductivity of Polyethylene Naphthalate (PEN)

Kusum Devgan[a] and Navjeet Kaur[b]
[a]Department of Physics S.R. Government College for Women, Amritsar (India)
[b]PG Department of Physics,Mata Gujri College, Fatehgarh Sahib (India)
kusamdevgan93@yahoo.com

Abstract

The effects of heavy ion irradiations such as 50 MeV Lithium and 120 MeV Nickel ions of different fluences have been investigated on the conductivity of Polyethylene Naphthalate, PEN. These studies indicate that electronic conduction via hopping process is taking place.

Keywords

Polymers, dielectric properties, thin films, lithium-ion, Hopping transport

I. Introduction

Polymeric materials are inimitable because of the range of structural forms that can synthesized and the way in which alterations can be made in the structure in local or general way. Polyethylene Naphthalate (PEN) (Poly (ethylene 2,6 naphthalate) is a new generation polyester polymer of naphthalene-2,6-dicarboxylate and ethylene glycol, demonstrating outstanding heat resistance and better dimensional stability. The irradiation of polymeric materials with ionizing radiation (gamma rays, X rays, accelerated electrons, ion beams) contributes to the formation of very reactive intermediates products (excited states, ions and free radicals), which result in rearrangements and/or formation of new bonds. The consequences of these reactions are formation of oxidized products, grafts, scission of main chain (degradation) or cross-linking. Often the two processes (degradation-cross-linking) occur simultaneously, and the result of the process is determined by a competition between the reactions [1-2].

Oxidation and degradation happen gradually with increasing irradiation dose. Different polymers have different reactions to radiation, which are as such related to the chemical structures of the polymers. Polymers with more hydrogen atoms on side (e.g., polyethylene) incline to cross-link with radiation. Polymers with a methyl group (e.g., polypropylene), disubstitutions (e.g., polymethacrylate) and per-halogen substitutions (e.g., polytetrafluoroethlene) would more likely undergo degradation with radiation. Aromatic polymers with benzene rings either in the main chain or on the side (e.g., polycarbonate) are normally radiation resistant [3]. Polycarbonate (PC) is a well known engineering thermoplastic with fantabulous balance of optical, physical, mechanical, and processing features [4]. Moreover, radiation effects on dielectric properties are of particular interest to science and technology and the result of ion irradiation on the dielectric properties of polymers has been also studied earlier [5-7]. It has been known for a long time that the electrical properties of insulating material are adversely affected by exposure to nuclear radiations. Some beneficial effects may deduce from the fact that radiation-induced currents can be used as a measure of radiation dose rate. Investigation of changes of dielectric properties is of importance in view of the extensive use of dielectrics in a nuclear environment and the continuous increase of the amount of radiation which electrical equipment is supposed to withstand. The influence of radiation on the properties and performance of a polymer differs according to whether the material degrades or cross-links and this is in turn depends on specific sensitivities or susceptibilities underlying in the polymer backbone. All materials have been found to break down at very high radiation doses, however, the range of doses under which a given polymer will maintain its desirable properties depends greatly on the chemical structure of the polymers. Indeed, below the destructive level of exposure, radiation treatment can contribute many benefits and enhance properties of commercial value [8-9]. The study of properties of PEN has been described in number of research papers [10-12]. The energy deposition and modifications in MeV light ion and UV laser induced luminescence of PET and PEN films brings out that luminescence centers are repressed by irradiation [13]. Since very less work on swift heavy ion irradiation on PEN is depicted, so the present work deals with the

experimental studies conductivity of PEN polymer irradiated with lithium ions (50 MeV) and nickel ions (120 MeV). The study provides information about the irreversible changes triggered in properties of polyethylene naphthalate, after Swift heavy ion irradiation.

II. Experimental

The specimens of Polyethylene naphthalate (PEN) in the form of flat polished thin films (25m) were procured from Good Fellow Ltd. (England). These films were used as-received form without any further treatment in the size of 1 cm x 1 cm. The samples were mounted on the sliding ladder and irradiated with lithium (50 MeV) and nickel (120 MeV) ion beams using 15 UD pelletron facility for the general purpose scattering chamber (GPSC) under vacuum of $\sim 10^{-6}$ Torr at Inter-University Accelerator Center, New Delhi. The electronic energy loss of characterize lithium (50 MeV) and nickel (120 MeV) ions in PEN polymer is ~6.96 and 563.3 eV/Å respectively [14]. The range of all ions is more than the thickness of polymer films. The ion beam fluence was varied from 1×10^{11} to 3×10^{12} ions $cm^{-2.}$ In order to expose the whole target area, the beam was scanned in the x-y plane. The beam current was kept low to suppress thermal decomposition and was monitored intermittently with a Faraday cup. The Precision impedance analyzer 6500B is used to measure coductivity of pristine and irradiated samples of polyethylene naphthalate at room temperature in the frequency range 20Hz-1MHz.

III. Result and Discussion

The frequency dependence of the ac conductivity is determined by plotting logσac versus log frequency for pristine and ion irradiated samples (irradiated with 50 MeV Lithium and 120 MeV Nickel ions) and is shown in Fig. 1 and 2. The significant change is observed in the ac conductivity due to ion irradiation which may be attributed to the formation of ion induced defects along the passage of incoming ions. When swift heavy ions penetrate into the material, a large amount of energy is deposited along its trajectory. The major fraction of its energy is lost due to the ionization and excitation of atoms known as electronic energy loss Se and rest of its energy is used for elastic and inelastic nuclear collisions known as nuclear energy

losses Sn. As electronic energy loss Se is generally higher than nuclear energy loss Sn, a large number of disordered regions are formed. As the ion fluence increases, these disordered regions overlap and result in the formation of ion induced defects and there is a change in the ac conductivity. The plot of logσac versus log frequency shows almost linear relation indicates that ac conductivity follows the relation σacα fn where n is the frequency exponent and can be calculated from the slope of straight lines of Fig. 1 and 2. The linear dependence of ac conductivity with frequency and the value of n<1 account for the electronic conduction via hopping process.

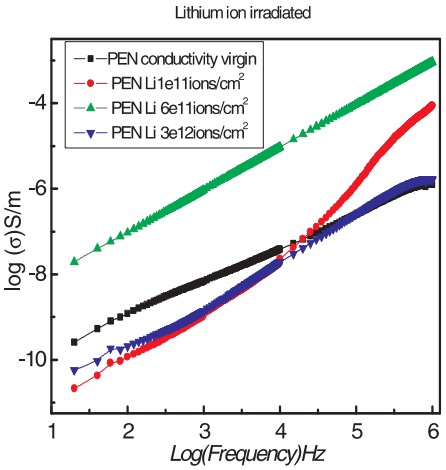

Fig 1.

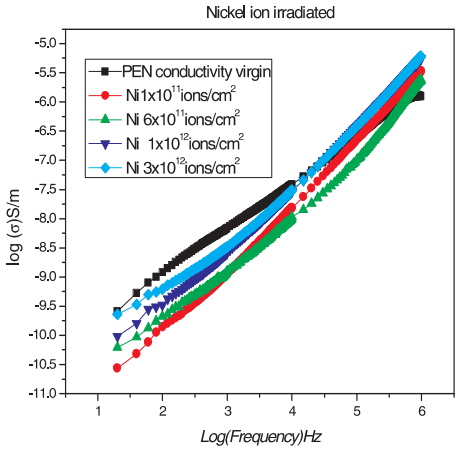

Fig. 2

IV. Conclusions

Samples of PEN have been irradiated with 50 MeV Lithium ions and 120 MeV Nickel ions at different fluencies. Irradiated PEN show a significant change in the *ac* conductivity which may be due to the formation of ion induced defects. The plot of *ac* conductivity is proportional to f^n in pristine and irradiated PEN with a slope $n<1$ which indicates that electronic conduction takes place through hopping process.

V. Acknowledgments

IUAC, New Delhi, is highly acknowledged for providing swift heavy ion facility to the authors for the experimental work.

VI. References

[1] R. Kumar, H.S. Virk, K.C.Verma, A. Saha, and U.De.R. Prasad, "Physico-chemical modifications induced in Makrofol N-polycarbonate by swift heavy ions," Nucl. Instr. and meth. in Phys Res B, 251 (2006) 163-166.

[2] D. Sinha, K.L. Sahoo, U.B. Sinha, A. Chemseddine, T. Swu, and D.Fink, "Gamma induced modifications of polycarbonate polymer," Radiat. Eff. & Def. in Sol, 9 (2004) 587-595.

[3] S. Cheng, and D.R. Kerluke, "Radiation processing for modification of polymers," Annual Technical Conference of the Society of Plastic Engineering (ANTEC) IBA, Advanced Materials Division, 7695 Formula Place, San Diego, (2003).

[4] J.Y.J. Chung, "Stabilization of Gamma-Irradiated Polycarbonate," Med. Plast. and Biomat. Tech. Paper Series, (1997). 49.

[5] S. Darwish, A. S. Riad and M. El-Shabasy, "8th arab international conference on polymer science & technology," Cairo-Sharm El-Shiekh, Egypt, (2005).

[6] D. S. Kim, K.W. Lee, and D. H. Park, "Transactions on electrical and electronic materials," Korea Sci, 4 (2000) 25-29.

[7] L. Boudou, J. Guastavino, N. Zouzou and J. M. Vega, "Influence of annealing treatment on the electrical conductivity of low density polyethylene," Polymer international, 50 (2001) 1046-1049.

[8] R. Kumar, S. Asad Ali, U. De, D. K. Avasthi, and R. Prasad, "Dielectric response of makrofol-KG polycarbonate irradiated with 145 MeV Ne6+ and 100 MeV Si8+ ions," Ind. J. of Phys, 83 (2009) 963-968.

[9] R.Ch. Abul-Hail, "Optical absorption of polycarbonate (Makrofol E) as means of Gamma-ray Dosimetry," J. of Basrah Res. (Sci.), 36 (2010) 26-30.

[10] S.Z.D. Cheng, and B.Wunderlich, "Thermal analysis of thermoplastic polymers," *Thermochem. Acta,* 134 (1988) 161-166.

[11] S. Buchner, D. Wiswe, and H.G. Zachmann, "Kinetics of crystallization and melting behavior of poly (ethylene-2,6 naphthalate) " *Polymer*, 30 (1989) 480-488.

[12] S. Murakami, M. Yamakawa, M. Tsuji, and S. Kohjiya, "Structural development in the uniaxial drawing process of poly (ethylene naphthalate)," *Polymer,* 37 (1996) 3945-3951.

[13] S. Nagata, H. Katsui, K. Takahiro, B. Tsuchiya, and T. Shikama, "Radiation-induced luminescence of PET and PEN films under MeV ion and pulsed UV laser irradiation," *Nucl. Instr. Methods phys. Res., Sect. B,* 268 (2010) 3099-3102.

[14] J. F. Ziegler, "Stopping and range of ions in matter," *Srim.org*, (2008).

Curr. Rep. Sci. & Tech. 1 (2) (2015) 124-130

Ion Track Membrane As Template For Copper Nanowires

S. Amrita Kaur and G.S. Randhawa
Department of Physics, Khalsa College Amritsar (India)
sanjitamrita@gmail.com

Abstract

Metallic as well as semiconducting nanowires are the most attractive materials having tremendous applications in electronics, magnetic devices, optics, whereas nanotubules have more potent applications in physical and biosciences. In the present paper, polymer (Makrofol-KG) were irradiated with heavy ions and chemically etched to produce cylindrical pores of various diameters. These membranes have been used as templates for the creation of metallic nanowires using potentiostatic electrodeposition within the confined nanochannels of porous track etched membranes. The morphology of copper nanowires has been studied using scanning electron microscopy.

Keywords

Ion track membranes, templates, copper, nanostructures

I. Introduction

There has been a tremendous growth of interest in investigation of metallic as well as non-metallic nano/micro structures and materials. They have potential applications in different fields viz. nano-electronics[1,2,3] magnetic devices[4-6] optics[7,8] chemical and biosensors[9,10] and chemical science[11]. Nanotechnology has attracted considerable attention in bringing a revolution in the development and advancement in techniques involving synthesis and fabrication of sensors and devices. The progress in this field has been accelerated by advances in by conventional techniques for fabrication of very low dimensional wires which includes - wet chemistry, electron beam lithography, focussed ion beam techniques and atomic beam lithography[12]. Tremendous influence on nanotechnologies is expected due

to new physical properties arising from small dimensions. Nanowires, fibres, tubules etc. having high aspect ratio would provide unusual and uncommon properties. In particular, nanowires have been produced and investigated by many different techniques. In this paper, we report the production of copper nanowires using the template synthesis[11,13] method. This method allow us to create very thin wires of few tens of nanometers with high aspect ratios (length over diameter). In the recent past extensive curiosity has been exhibited in the production of nanomaterial fabrication involving metals, semiconductors, magnetic multilayered nanowires, conducting polymers, glasses etc. reported by various authors[14,17] elemental understanding of nanomaterials properties and their potential use for technological applications in various fields.

In the present work, copper nanowires were electrochemically synthesized using etched ion track pores in polycarbonate membranes. Morphology of electrodeposited copper nanowires has been studied using scanning electron microscopy (SEM). These nanowires have uniform diameter of about 250nm, which corresponds to the pore size of the template used. As templates, most commonly porous alumina, mica and polymeric ion track filters are used. For the formation of suitable ion track membranes, the etch rate along the track (V_t) should be much larger than the etch rate of the undamaged bulk material (V_b). The ratio V_t/V_b determines the resulting geometry of the pores[18]. The ratio determines many characteristics like energy, mass and charge resolution of detector and depends upon the damage density in the track, which is related to the stopping power of the projectiles in the polymer (dE/dx)[19].

II. Materials And Methods

A. Production of Ion Track Pores in Polymer

In particular, polycarbonate membranes (Makrofol-KG) of thickness 10μm, irradiated with heavy ion U^{238} having fluence 10^8 ions/cm^2 at normal incidence from UNILAC accelerator, GSI, Darmstadt, Germany have been used. These samples were chemically etched at room temperature 27 ± 1^0C, for 10 minutes in etchant 6N NaOH solution. The resulting pores are cylindrical having pore diameter of size ~250nm, their diameters increasing linearly with the time of etching.

B. Production of Copper Template.

A thick copper layer was sputtered on to one side of the ion track membrane (ITM) which acts like a cathode in two electrode electrochemical cell whereas pure copper rod act as an anode. The electrolyte consisted of an aqueous solution of 200 g/l $CuSO_4.5H_2O$ and 25 g/l H_2SO_4. High concentration of $CuSO_4$ is important to provide a sufficiently large number of copper ions inside the pores during the galvanic deposition process. Electrodeposition was performed potentiostatically at room temperature i.e 38±1°C. During the deposition process, we recorded the electrical current as a function of time. Fig. 1 shows the current versus time graph during electrodeposition process.

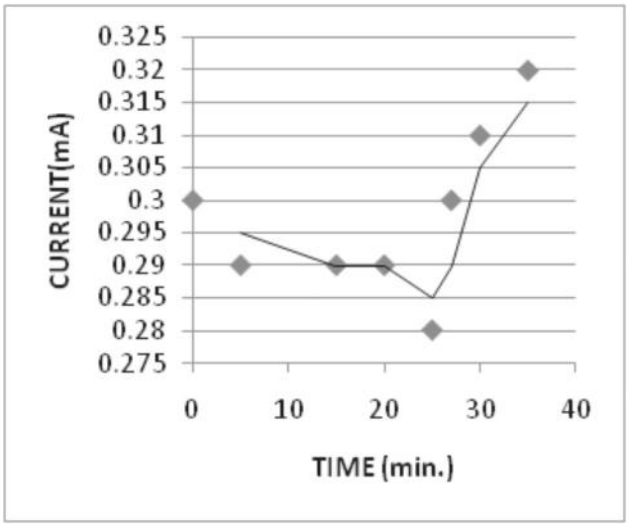

Fig 1. Variation of current versus time during electrodeposition.

After the deposition the polycarbonate templates with Cu nanowires were immediately removed from the electrolyte, first rinse with double-distilled water and ethanol, finally dried in dry air at room temperature. The porous polycarbonate membrane was removed by dissolving it in dichloromethane for 10 minutes and subjected to further analysis. The cleaned and dried samples were mounted on specially designed aluminium stubs with the help of double adhesive tape, coated with a layer of gold palladium alloy in Zeiss, Fine Sputter, coater and viewed under "Carl Zeiss Supra 55 Scanning Electron Microscope" at an accelerating voltage of 10

KV. The nanostructures of copper (Cu) grown through the multipore ITFs of Makrofol-KG are shown in Figures 2 & 3 respectively. Voltage-Current characteristics of copper grown structures is shown in Fig.4.

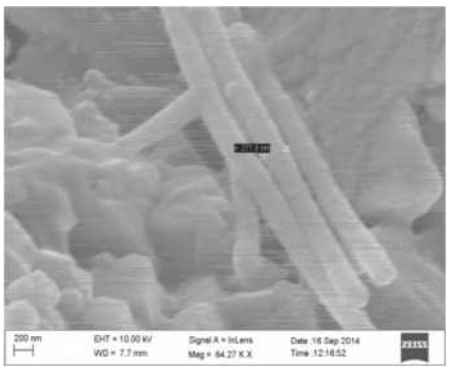

Fig 2. Nanostructure ensembles of Cu grown electro-chemically

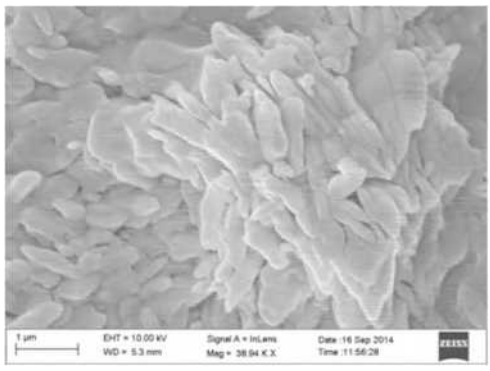

Fig 3. Cluster of microstructure ensembles of Cu grown electrochemically

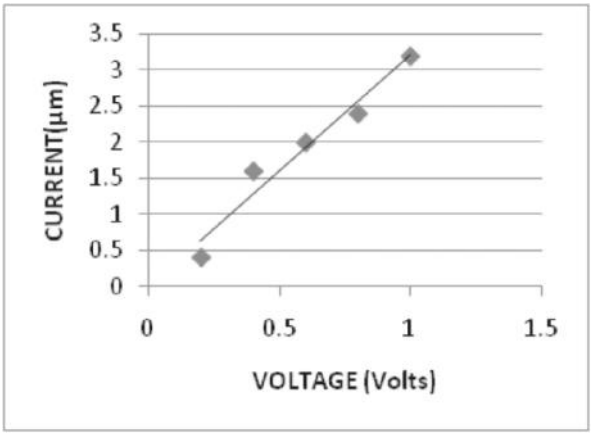

Fig 4. Plot of V-I characteristics of Cu grown structures.

III. Results And Discussion

As the shape of the wires directly reflects the geometry of the pores in the polymer (Makrofol-KG). It clearly indicates that under the employed irradiation and etching conditions, the pores are well aligned and have cylindrical geometry. The surface smoothness of wires depends on several factors viz., quality of polymer, etching process, electrode position, presence of air bubbles in the pores, hydrogen evolution during deposition

at high voltages and quality of deposited metal at high current densities results in roughness of wire surface. Single wire generated having smooth and good alignment of pores perpendicular to the membrane surface is of great importance if homogenous needle growth is required. The ITMs offer distinct advantages for their use as templates for the generation of nano/microstructures over other host membranes like alumina membranes, nanochannel array glass membranes, xeolites etc. This is because in ITMs, pore density, pore shape and aspect ratio can be controlled19-20 as per the specific requirements by suitably choosing incident ion beam from the accelerator and the etching conditions. The morphological study of such structures produced through electrochemical methods and of replicas of etched tracks in ITMs used as templates, has two-fold purpose. One, it provides the finest and critical details of the geometry and dimensions of micro structural constituent elements and the second, as a by product it enables to study the various aspects of interaction of a nuclear particle with given material leading to formation of tracks in ITM. It is well known that parameters, which control the shapes of tracks in ITMs, include the nature of the material; the ion beam and energy deposition rate; pre, post-irradiation storage and environment and the etching conditions20-22.

IV. Conclusion

It should be emphasized that heavy ion etched tracks in polymers are most suitable for the production of templates with cylindrical pores. In such membranes, the grown copper wires of nanometer range reveals basic research and applications where a high degree of parallelism plays important role. It provide us the simplest route to nanotechnology and generation of nanodevices. The nano wires have huge potential for their use as biosensors, field emission studies[23] etc.

V. Acknowledgements

The author is thankful to Dr. Reimer Spohr of GSI, Darmstadt, Germany for providing irradiation facilities and also thankful to Prof. H.S. Virk and Prof. S.K. Chakarvarti for their guidance and Dr. Jaskiran Kaur,

Department of Physics G.N.D.U. Amritsar for providing the SEM facilities.

VI. References

[1] D. Fink , P.S. Alegaonkar, A.V. Petrov, M. Withelm, P. Szimkowiak, M. Behar, D. Sinha, W.R. Fahrner, K. Hoppe and L.T. Chadderton, "High energy ion beam irradiation of polymers for electronic applications" Nucl. Intr. Methods in Physics Research B, 236 (2005) pp.11-20.

[2] S. Tsukuda, S. Seki, S.Tagawa, M.Sugimoto, A. Idesaki and S.Tanaka, Fabrication of nanowires using high-energy ion beams J. Phys. Chem. B, . 108 (2004) 3407.

[3] S.Amrita Kaur and Jyot Amrita, " Track etched membranes for electronic applications" International J. of Science and Research, 4(1) (2015) 1414-1417.

[4] S. Mechotte, L. Piraux, S. Dubois, F. Piailloux, J. Stenuit and J.Govaerts, "Superconducting properties of lead nanowires arrays" Physics C, 377 (2002) 267.

[5] K. Liu, K. Nagodawithana, P.C. Searson, C.L. Chien, "Perpendicular giant magnetoresistance of multilayered Co/Cu nanowires" Phys. Rev. B, (1995) 7381.

[6] V. Scarani, B. Doudin and J.P. Anermet, The microstructure of electro-deposited Cobalt-based nanowires and its effect on their magnetic and transport properties Magn. Mater.J., 205 (1999) 248.

[7] M. Saito, T. Kano, T.Seki and M. Miyagi Microwire arrays for infrared polarizers Infrared Phys. Technol., 35 (1994) 709.

[8] Jr C.A.Foss, C.A.Tierney and C.R.Martin, Template synthesis of infrared transparent metal microcylinders comparison of optical properties with the predictions of effective medium theory J.Phys. Chem., 96 (1992) 9001.

[9] S.P.Singh, S.K. Arya, P. Pandey, B.D. Malhotra, S. Saha, K. Sreenivas and V.Gupta, "Cholesterol biosensor based on rf sputtered zinc oxide nanoporous thin film" App. Phys. Lett. 91 (2007) 063901.

[10] H. Bayley, and B.S. Cremer, Stochastic sensors inspired by biology: Article. Nature, 413 (2001) 226230.

[11] C.R. Martin, "Nanomaterials: a membrane based synthetic approach" Science, 266 (1994)1961.

[12] He Huixin and J Nongjian Tao, Encyclopedia of Nanoscience and Nanotechnology, H.S. Nalwa, Vol.1 ,USA, Academic press, (2000).

[13] M. Sima, I. Enculesca, C.Trautmann, R. Neumann, "Electrodeposition of CdTe nanorods in ion track membranes" J. of Optoelec. and Adv. Mater., 6 (2004) pp.121-125.

[14] J. Vetter, " Free standing metal whiskers" GSI Darmstadt, (2010) pp. 04-27.

[15] S.K. Chakarvarti "Track-etch membranes as templates enabled nano/micro technology: a review" Ind. J. Phys. 83 6 (2009) pp.737-749.

[16] C.J. Brumlik, V.P. Menon and C.R. Martin, "Template synthesis of microtubule ensembles utilizing chemical, electrochemical and vacuum deposition techniques" J. Mater. Res. 9, (1994) 1174.

[17] T.M. Whitney, J.S. Jiang, P.C. Searson and C.L. Chien, "Fabrication and magnetic properties of arrays of metallic nano wires" Science 261 (1993)1316.

[18] J.H. Schön, A. Dodabalapur, Ch Kloc, B Batlogg, "A light emitting field effect transistor" Science 290 (2000) 963.

[19] R.L. Fleischer, P.B. Price & R.M. Walker, Nuclear tracks in solids: Principles and Applications, University of California press, Berkely, (1975).

[20] S. Amrita, G.S. Randhawa, S.K. Chakarvarti and H.S.Virk," Fabrication of metallic and polymeric microstructures using ion track filters" Ind. Jourl. of Pure and Appl. Phys., 37(1999) 924-928.

[21] E. Ferain, R. Legras, "Characteristics of nanoporous particle track etched membrane" Nucl. Instr. and Meth., B (1997) 97.

[22] C. Schoenberger, B.M.I. Vander Zande, L.G.F. Fokkink, M. Henny, C. Schmid, M. Kruger, A. Bachtold, R. Huber, H. Birk, and U. Staufer, "Template synthesis of nanowires in porous polycarbonate membranes" J. Phys. Chem. B. 13 (1997) 5407.

[23] R. Spohr, 23rd International Conference on Nuclear Tracks in Solids, Beijing, China, (2006).